McGill University

Master's Thesis

Calculating the role of composition in the anisotropy of the solid-liquid interface via phase field crystal theory

Author:
Bernadine A. Jugdutt

Supervisor:
Dr. Nikolas Provatas

A thesis submitted in partial fulfilment of the requirements
for the degree of Master of Science

in the

Department of Physics

Submitted March 2015

MCGILL UNIVERSITY

Abstract

Faculty of Science

Department of Physics

Master of Science

Calculating the role of composition in the anisotropy of the solid-liquid interface via phase field crystal theory

by Bernadine A. Jugdutt

Microstructure formation in alloys is a field of great interest to the materials science community, as the microstructural features of a material determine many of its physical properties. As such there is a strong desire to understand the mechanisms behind the formation of microstructure, so that material properties might be better engineered. Dendritic solidification in particular has been extensively studied, and choice of dendrite orientation related back to the interfacial anisotropy of the material. Experimental work in recent years has found that the anisotropy selection mechanisms influencing dendrite orientation are more complex than previously realized, and in fact may be strongly tied to the respective compositions of alloy species. A large body of work done with *phase field* (PF) and *phase field crystal* (PFC) type models has proven both very successful in determining the underlying causes of microstructural formation. In this work we utilize PFC and effective phase field methods derived from them to make a determination of the concentration dependence of interfacial anisotropy in two-component metallic alloys.

Résumé

La connaissance des phénomènes microscopiques dans les alliages est un sujet important à la communauté de la science des matériaux, parce que la morphologie microscopique détermine la plupart des propriétés physiques des matériaux. Par conséquent, il existe un désir de comprendre les mécanismes de formation de ces structures afin de mieux contrôler les propriétés des matériaux. En particulier, la solidification de dendrites a été très étudié. Orientation préférentielle de la dendrite est lié à l'anisotropie de l'interface du matériau. Travaux expérimentaux récents ont constaté que l'anisotropie de l'interface est plus compliqué qu'on ne le pensait, et qu'il peut être fonction de la composition des espèces d'alliage. Techniques *phase field* (PF) et *phase field crystal* (PFC) sont avérées très efficaces dans la compréhension des mécanismes de formation de la morphologie microscopique. Dans cette thèse, nous utilisons des méthodes PFC et PF connexes pour déterminer la dépendance de la composition de l'anisotropie interfaciale dans les alliages métalliques à deux composants.

Acknowledgements

This work would not have been possible without the support of several individuals.

First and foremost, my sincerest gratitude goes to my supervisor, Prof. Nikolas Provatas. His enthusiasm for his work is infectious and genuinely inspiring. He has always made himself readily available to his students, and the group dynamic and regular discussions that he has encouraged have been instrumental in my own learning. Nik is both a great scientist and a great mentor, and I consider it a privilege to have been his student.

I would also like to thank Dr. Nana Ofori-Opoku. I first met Nana as a doctoral candidate in Nik's group, and have been exceedingly fortunate to have had his mentorship over the last few years. His insight, intelligence and dedication are truly remarkable, and he has acted as a sounding board, an advisor, and a friend on more occasions than I can count.

Thanks also goes out to the other members of my research group, both current and former, for discussion, for suggestions, and for partners in crime when it came time to blow off steam. It's been a fun ride and I'm happy to have met you all.

Finally, thanks to my friends and family for their support, particularly to Jack for always being there to talk me through the tough times, and to the wonderful employees and regulars of Second Cup du Parc, my home-away-from-home and unofficial office, for conversation and caffeine.

This work could not have been completed without the resources from Compute Canada and Calcul Québec, in particular the use of the Clumeq and Sharcnet facilities.

Contents

List of Figures

List of Tables

Chapter 1

Introduction

It is well known in the materials science and engineering community that many of the characteristic physical properties of a material can be traced back to aspects of the material's microstructure, that is, the underlying, microscopic-scale features of the material[2]. It is often the case that gaining an understanding of the mechanisms behind the formation of such microstructures gives us a tool with which to control particular properties of the final material.

One particular such microstructural feature that has been of interest to both theoretical and experimental studies for some time is the dendrite, a branched, directional structure that forms in solidifying materials. Dendrites are understood to emerge as a result of thermal or diffusive instabilities and subsequently grow in the orientation that provides the lowest stiffness. Ascertaining this orientation had for some time been thought to be a simple matter of determining the interfacial anisotropy associated with the crystal symmetry of the material; in the case of an alloy with competing symmetries arising due to the preferred crystal structures of its constituent species, the dendrite was thought to select the orientation of the dominant species and to switch discontinuously from one choice of direction to another[3][1] for different compositions.

A wealth of experimental studies[4][3][5] in the past ten to fifteen years have suggested that this is not always the case, and in fact that there exist a class of materials for which a continuous variation in dendrite orientation seems to be possible. This surprisingly complex behaviour suggests, then, that the interfacial anisotropy of such materials is not as simplistic as was previously thought. In particular, there has been some suggestion from experiments[3][1] that this anisotropy has a significant dependence on the respective composition of the alloy in question.

Modern numerical modelling techniques have proven very adept at discerning the behaviour and properties of materials at a microscopic scale, especially in terms of the behaviour of the interface. In particular, *phase field* (PF) and *phase field crystal* (PFC) methods have yielded impressive results in a multitude of diverse phase transformations, including solidification and solid state processes.

In solidification, PF modelling has been succesful in quantitatively predicting the relationship between growth rate and morphology of individual dendrite crystals[6][7], the branch-spacing selection in directional solidification under steady state conditions[8], and transient conditions relevant to industrial processes[9]. In the solid state, the PFC methodology, comprised of an atomic scale density functional theory, has been used alongside TEM work to quantitatively predict the elusive mechanisms behind precipitation in age-hardened alloys[10].

In this work we aim to make use of both PFC methods and effective phase field techniques derived from these to further elucidate both the behaviour of and the mechanisms behind the changing anisotropy of the solid-liquid interface in alloy materials. In particular we restrict ourselves to the investigation of a binary (two-component) alloy formation, and the effect of altering the fractional composition of such an alloy on the resulting interfacial anisotropy.

To date there has been, to our knowledge, no fundamental study of the possible mechanism behind this phenomenon in alloy materials. Most molecular dynamics models have examined pure substances, with a focus on fluctuations. Meanwhile, traditional phase field models are not appropriate to examine anisotropy, as they require the input of information about the interfacial stiffness and other atomic scale properties. It is the aim of this thesis to make use of a relatively new *microscopic* continuum theory, the structural PFC alloy model, to derive an effective phase field theory from which investigations of the interface anisotropy can be made. Since the salient features of PFC theory are fundamentally linked to classical density functional theory of the liquid state, the resulting PF model will be endowed with parameters that contain fundamental - rather than phenomenological - information about anisotropy.

Chapter 2

Background Information

2.1 Microstructure

The term *microstructure* broadly refers to any structural feature of a material resolved on the microscopic scale, and includes the material's underlying crystal lattice, any grain boundaries or defects, and the dendrite structure, to name a few. Microstructural features are determining factors for many of the properties of engineering materials, from band structure and conductivity to hardness and tensile strength. For instance, the presence of a large number of grain boundaries (and correspondingly small grain size) has been shown to contribute to increased ductility in metallic alloys. High numbers of dislocations, on the other hand, decrease ductility but increase the hardness of the material via a well-known process called *work hardening*. Being able to predict the microstructure that may arise in a material has allowed us to make progress in controlling and understanding its physical properties.

One particular feature of interest is the *dendrite*. Dendrites are branching tree-like structures that form as a material solidifies. Their directionality and three-dimensional shape are specified by the anisotropies of the material, and in particular are heavily dependent on the thermodynamics of the solid-liquid interface. A variety of 3-dimensional dendritic structures are possible [3]. As stated in the introduction, there is a long list of investigations performed on dendritic microstructures, too extensive to discuss here. The reader is referred to the following reviews by Granasy [11], Emmerich [12], and Provatas [13].

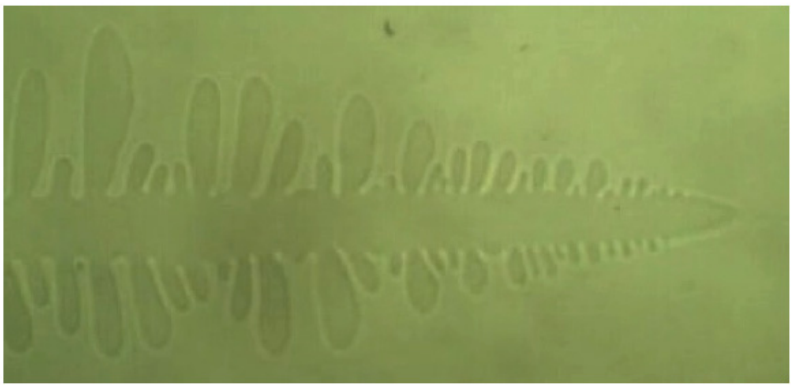

FIGURE 2.1: An example of a characteristic dendritic shape, grown in succinonitrile (SCN). This image reprinted with permission from [14].

Many complexities of dendrite growth, such as tip radius, growth velocity, and side branching behaviour, have merited study. The characteristic that we are interested in, however, is growth direction. Previously it was believed that dendritic growth could only occur along the primary crystallographic axes of a material; however, both experimental [1, 4, 5, 15] and computational [3] results now exist showing that this is not always the case, and, indeed, that a continuous range of dendrite growth directions may be possible in certain solids. Studying the role of alloy impurities on dendritic growth direction will be the focus of this thesis.

2.1.1 Dendrite Orientation and the Solid-Liquid Interface

Dendrites form due to instabilities in the solid-liquid interface of a solidifying material. When the rate of solidification is low enough that the effect of attachment kinetics is negligible, it is expected that the direction of dendrite growth will follow one of the primary crystallographic directions. This is the case for most conventional metal-casting technologies that manufacture aluminum or steel based products, for example. For crystals with underlying cubic symmetry, the expected growth directions are $< 100 >$ for FCC and BCC structures, and $< 1010 >$ for HCP [1], the assumption being that these directions correspond to minima of the interfacial stiffness.

However, there is a growing body of evidence suggesting that this picture is oversimplified, particularly in cases where the material in question exhibits weak anisotropy. Experimental studies in FCC aluminum alloys have found a wealth of unexpected morphologies, including feathered structures along the $< 110 >$ direction [5], dendrite growth

along the $< 320 >$ direction [15], and even curved dendrite paths changing orientation from $< 112 >$ to $< 110 >$ [5].

In light of these observations it was clear that the relationship between interfacial anisotropy and dendrite orientation merited further study. Following the presentation of an improved expression for calculating anisotropy developed using molecular dynamics simulations [16], a thorough phase field simulation study of pure material dendrite orientation was performed by Haxhimali et al [3] for a variety of experimentally motivated values of the anisotropy parameters. A continuous change in dendrite orientation from $< 100 >$ to $< 110 >$was found as these parameters were varied. This range of growth orientations was consistent with those observed experimentally within a single sample.

It was clear that anisotropy could change dramatically, and the dendritic morphology along with it; the question became what was causing it to vary. An experimental study also done by Haxhimali et al [3] showed for an Al-Zn alloy that the same continuous change in orientation could be obtained by varying the weight percentage of Zn. Additional work on the same material by Gonzalez and Rappaz [1] provided theoretical fits for the interfacial stiffness by assuming that observed growth angles corresponded to stiffness minima. These fits demonstrate significant changes in angular dependence of stiffness for various concentrations of zinc, to the point of maxima shifting to minima for sufficiently large compositional changes.

There is thus significant experimental evidence for a relationship between alloy concentration and stiffness anisotropy; our goal in this study is to provide a computational framework to both quantify and gain a theoretical understanding of this relationship.

2.1.2 Quantifying Interfacial Anisotropy

We intend to measure anisotropy via the interfacial energy. As mentioned in the previous section, materials with relatively weak anisotropy may be more likely to exhibit a variety of dendritic orientations and therefore, presumably, will be more strongly affected by composition changes. Weak anisotropy is the case in metallic alloys, the most common practical material in which dendritic growth is relevant. We thus need a method of observing the changes in anisotropy even when it is quite weak.

Hoyt et al [16] proposed a method to examine anisotropy using stiffness rather than interfacial energy alone as the representative quantity. In 3 dimensions, the energy of an interface is traditionally fit via an expansion in terms of spherical harmonics, chosen

to reflect the symmetry of the crystal in question [1]. Simplifying this expansion to two dimensions (by setting one of the angular parameters to a constant) gives, for a crystal with square symmetry, the form [16]:

$$\gamma(\theta) = \gamma_0(1 + \epsilon_4 \cos 4\theta + \epsilon_8 \cos 8\theta + \ldots) \tag{2.1}$$

where ϵ_4 is the first order anisotropy parameter, ϵ_8 is the second order anisotropy parameter, and so on. The first order parameter ϵ_4 is typically on the order of 10^{-2}. Higher order fits can be made if necessary.

The interfacial stiffness

$$S(\theta) = \gamma(\theta) + \frac{d^2\gamma(\theta)}{d\theta^2} = \gamma + \gamma'' \tag{2.2}$$

shows anisotropy an order of magnitude stronger than γ alone, and thus makes it easier to observe the maxima and minima of weakly anisotropic materials. This can be illustrated explicitly if we calculate stiffness from the the first order expansion of Eq 2.1:

$$\begin{aligned} S &= \gamma_0(1 + \epsilon_4 \cos 4\theta - 16\epsilon_4 \cos 4\theta) \\ &= \gamma_0(1 - \alpha \cos 4\theta) \end{aligned} \tag{2.3}$$

where the stiffness anisotropy parameter becomes $\alpha = 15\epsilon_4$.

We will use Eq 2.1 to fit simulation results for the interfacial energy, and from the resulting fit determine the stiffness of the system.

2.2 Phase Field Crystal Modelling

The approach that we use in this work to model solid-liquid interfaces has been coined the *phase field crystal* model. It can be seen as a hybrid between traditional phase field theory and classical density functional theory (hereafter just 'density functional theory'). The former allows a self-consistent and efficient approach for modeling interfaces, while the latter introduces atomic-scale density variations.

Density functional theory can be thought of as a continuum extension of molecular dynamics (MD) studies, the latter of which functions by describing the interactions between individual particles in terms of atomic potentials. These simulations provide atomic-scale

resolution and can thus be used to study properties such as individual point defects in the underlying crystalline symmetry of a lattice. The downside is that each atom must be tracked individually, which severely limits both the system sizes and the timescales that can reasonably be studied.

Phase field (PF) simulations, on the other hand, represent a system through a free energy functional, expressed in terms of smooth local order parameter fields, and additional fields representing relevant conserved parameters. The evolution of these fields is derived via dissipative minimization of the free energy, subject to the appropriate conservation laws. Thermal fluctuations are absorbed into the stochastic noise strength, which follows the fluctuation-dissipation theorem. PF simulations are able to access system sizes and time scales large enough to be experimentally relevant, but sacrifice atomic resolution in order to do so: each phase of a system is represented as a constant field, with a largely continuous transition between the two values occuring at the interface. The effects of atomic scale features have only been introduced into these models phenomenologically.

In recent years a new type of phase field approach has been introduced [17][18][19] that defines the free energy of the system to be minimized in terms of periodic order parameter fields: the *phase field crystal* (PFC) technique. In its most fundamental form, this approach essentially reproduces classical density functional theory, and the order parameter is proportional to the local time or ensemble averaged atomic number density. In its more practical, albeit cruder, manifestations, the order parameter loses this rigorous connection to atomic number density, but maintains the ability to represent crystal symmetries, topological defects, and density wave fluctuations that are seen in materials. With PFC, then, we aim to maintain a computational advantage over CDFT and MD models, while reproducing the physics resulting from the presence of atomic scale structures.

2.2.1 Derivation of the Standard PFC model from Density Functional Theory

The first form of the PFC model was presented by Elder et al in 2002 [20]. It was motivated by extending the free energy of the standard PF model for a conserved order parameter to include a term minimized in the solid by a periodic order parameter field, rather than a constant. This model can be seen as a re-interpretation of the classical Swift-Hohenberg equation for modelling periodic patterns in block-copolymers. It has

since been shown [18] that this form can also be derived directly from classical density functional theory (DFT) formalism; the procedure to do so is outlined in this section.

We take as a starting point the free energy functional presented by Ramakrishnan and Yussouff [21] in which free energy $F[\rho]$ is expanded around a reference liquid state at a coexistence point with the solid. The dimensionless form is:

$$\frac{F}{k_B T} = \int d^3\vec{x} \left\{ \rho \ln\left(\frac{\rho}{\bar{\rho}}\right) + (\rho - \bar{\rho}) - \frac{\rho}{2} \int d^3\vec{x}' C(|\vec{x} - \vec{x'}|)\rho(\vec{x'}) \right\} \tag{2.4}$$

in which $\rho(\vec{x})$ is the position-dependent density field, and $\bar{\rho}$ is the liquid reference density. The $C(|\vec{x} - \vec{x'}|)$ term is the two-point correlation function. In the formal expansion (Eq 2.4), this would continue up to n-point correlations. However, past studies [17] have found that retaining only the two-point correlation function is sufficient to obtain many of the desired properties of the solid-liquid interface, the specifics of which will be addressed in this work.

To obtain an expression in terms of the PFC model variables, position is rescaled in terms of the lattice constant a such that $\vec{r} = \frac{\vec{x}}{a}$. We also define a dimensionless density term $n = (\rho - \bar{\rho})/\bar{\rho} = (\rho/\bar{\rho}) - 1$, and can thus rewrite Eq 2.4 as

$$\frac{F}{k_B T} = a^3 \int d^3\vec{r} \left\{ \bar{\rho}\,(n+1)\ln(n+1) + \bar{\rho} n - \frac{\bar{\rho}\,(n+1)}{2} \int d^3\vec{r}' [\bar{\rho} a^3 C(|\vec{r} - \vec{r'}|)](n(\vec{r'})+1) \right\} \tag{2.5}$$

To obtain a more mathematically tractable expression, the nonlinear bulk term is expanded to fourth order in n, giving

$$\frac{F}{k_B T} = a^3 \int d^3\vec{r} \left\{ \left(2\bar{\rho} n + \frac{\bar{\rho}}{2} n^2 - \frac{\bar{\rho}}{6} n^3 + \frac{\bar{\rho}}{12} n^4\right) - \frac{\bar{\rho}(n+1)}{2} \int d^3\vec{r}' [\bar{\rho} a^3 C(|\vec{r} - \vec{r'}|)](n(\vec{r'})+1) \right\} \tag{2.6}$$

The key feature of the original PFC model [17] is the approximation of the correlation function as a sum of gradients. We choose to truncate the sum at the ∇^4 term:

$$C(|\vec{x} - \vec{x'}|) = \left(-\hat{C}_0 - \hat{C}_2 \nabla^2_{x'} - \hat{C}_4 \nabla^4_{x'}\right) \delta(\vec{x} - \vec{x'}) \tag{2.7}$$

which can be written conveniently in k-space as

$$\hat{C}(|\vec{k}|) = -\hat{C}_o + \hat{C}_2 k^2 - \hat{C}_4 k^4 \tag{2.8}$$

For all $\hat{C}_n$ positive, this expression describes a single-peaked correlation function around some finite wavelength $2\pi/|\vec{k}|$. In terms of the dimensionless variable $\vec{r}$, the correlation can be written as

$$\bar{\rho}a^3 C(|\vec{x}-\vec{x'}|) = \left(-\bar{\rho}\hat{C}_o - \frac{\bar{\rho}\hat{C}_2}{a^2}\nabla^2_{r'} - \frac{\bar{\rho}\hat{C}_4}{a^4}\nabla^4_{r'}\right)\delta(\vec{r}-\vec{r'}) \tag{2.9}$$

The shape of Eq 2.9 implies that we can take $d\hat{C}/dk = 0$ to solve for the lattice constant a in terms of gradient coefficients. We find that $a = 2\pi\sqrt{2\hat{C}_4/\hat{C}_2}$. To obtain the form presented by Elder and Grant [17] the following definitions are then made:

$$\begin{aligned} B^x &= \frac{\bar{\rho}\hat{C}_2^2}{4\hat{C}_4} \\ B^l &= \bar{\rho}\hat{C}_0 + 1 \\ \Delta B &= B^l - B^x \end{aligned} \tag{2.10}$$

Rewriting Eq 2.9 with these substitutions and applying the delta function gives the final form of the original PFC model for a pure substance.

$$\frac{F}{k_B T\bar{\rho}a^3} = \int d^3\vec{r}\left\{\left(2n + \frac{n^2}{2} - \frac{n^3}{6} + \frac{n^4}{12}\right) - \frac{(n+1)^2}{2}(1-\Delta B) + \frac{(n+1)}{2}\left[B^x\left(2\nabla^2_{r'} + \nabla^4_{r'}\right)\right]n\right\} \tag{2.11}$$

Finally we consider the functional form of the solid density field, which emerges under minimization of Eq 2.11 for certain parameter ranges. This is the key distinguishing element of the PFC model, in which density is thought of as a continuously varying field with peaks at atomic sites in the lattice and troughs between them. We can thus think of the density as a sum of sinusoidal functions, or equivalently in terms of a sum of exponentials of the reciprocal vectors of the desired crystal lattice

$$n(\vec{r}) = n_0 + \sum_{\vec{G}} \eta_{\vec{G}} e^{i\vec{G}.\vec{r}} + c.c. \tag{2.12}$$

where $\vec{G}$ are reciprocal lattice vectors of the crystal structure in question and $\eta_{\vec{G}}$ are the amplitudes of each reciprocal lattice mode. Here we will take the lowest order *single-mode expansion*, retaining only the smallest reciprocal lattice vectors required to reconstruct the particular crystal symmetry. It can be shown that by using this expansion, constant or linear terms in $n(\vec{r})$ will only contribute vanishing terms to the free energy at long

wavelengths and as such can be disregarded at the microscopic level described by Eq 2.11 [18]. Applying this simplification, and as a final step introducing the variables η and χ as additional degrees of freedom with which to parametrize the bulk terms of the free energy expansion, the dimensionless PFC free energy is presented as[1]

$$\bar{F} \equiv \frac{F}{k_B T \bar{\rho} a^3} = \int d^3\vec{r} \left\{ -\eta \frac{n^3}{6} + \chi \frac{n^4}{12} + \frac{n}{2} \left[\Delta B + B^x \left(2\nabla_r^2 + \nabla_r^4 \right) \right] n \right\} \tag{2.13}$$

Expanding out this notation for a moment to the form

$$\bar{F} = \int d^3\vec{r} \left\{ \frac{n}{2} - \eta \frac{n^3}{6} + \chi \frac{n^4}{12} + \frac{n}{2} \left[\bar{\rho} \hat{C}_0 + \frac{\bar{\rho} \hat{C}_2^2}{4 \hat{C}_4} (2\nabla_r^2 + \nabla_r^4 - 1) \right] n \right\} \tag{2.14}$$

reveals that the first, *ideal* component of Eq 2.14

$$\Delta F_{id} = \int d^3\vec{r} \left(\frac{n}{2} - \eta \frac{n^3}{6} + \chi \frac{n^4}{12} \right) \tag{2.15}$$

is an entropic term that, by itself, drives the system towards a uniform field. The second component is termed the *excess* energy

$$\Delta F_{ex} = \int d^3\vec{r} \frac{n}{2} \left[\bar{\rho} \hat{C}_0 + \frac{\bar{\rho} \hat{C}_2^2}{4 \hat{C}_4} (2\nabla_r^2 + \nabla_r^4 - 1) \right] n \tag{2.16}$$

and is what supports the existence of periodic structures (i.e.crystals). Effects of the underlying crystal lattice, such as anisotropy or defects, arise due to the presence of this term. It is clear then that the form of the correlation function is the critical feature in controlling the behaviour of the system. The following section introduces the newer *structural PFC* (XPFC) model, which differs from this approach primarily in its treatment of the correlation function.

2.2.2 XPFC Functional

The structural PFC model was introduced in 2010 [23][19] and was intended as a formalism that allowed more direct connection to the underlying crystallographic symmetry of the solidifying material in question. In 3 dimensions this model was able to stabilize FCC, BCC, HCP and SC structures without difficulty, as well as coexistence between

[1] These coefficients can also be shown to arise as $\vec{k} = 0$ contributions from higher order correlation functions[22].

combinations of such structures and with the liquid phase. In 2 dimensions, square and triangular symmetries are equally simple to obtain.

The ideal component of the XPFC free energy functional maintains the same form as Eq 2.15.

For the excess free energy of the system we begin with the correlation function term presented in Eq 2.4.

$$\Delta F_{ex} = -\frac{1}{2}\int d^3\vec{r} n(\vec{r}) \int d^3\vec{r}' C(|\vec{r} - \vec{r}'|) n(\vec{r}') \tag{2.17}$$

The form of the correlation function is motivated by the underlying crystal symmetry of the system in question. Thus to model different lattice structures it is necessary to change both the mode approximation and the correlation function. The formulation of the correlation function is as follows:

Consider a crystal in which each atom vibrates around its equilibrium lattice position. The probability of the atom occupying some location in space at a given time can be represented by a Gaussian centered at the equilibrium position. The full crystal can be seen as a sum of Gaussians representing individual lattice sites,

$$P(\vec{r}) = \sum_i P_i(\vec{r}) = \sum_i \frac{1}{\sigma\sqrt{2\pi}} e^{-\frac{1}{2\sigma^2}(\vec{r}-\vec{r}_i)^2} \tag{2.18}$$

where σ is the width of the Gaussian and the $\vec{r}_i$ are the equilibrium lattice positions. In k-space

$$\hat{P}_i(\vec{k}) = \cos(\vec{k}\cdot\vec{r}_i) e^{-\frac{1}{2}\sigma'^2\vec{k}^2} \tag{2.19}$$

The sum over the $\hat{P}_i(\vec{k})$ gives a series of sinusoidal functions that interfere to produce delta function peaks at the $\vec{k}$ vector values corresponding to the locations of lattice planes (assuming an infinite lattice). The exponential factor acts as a Debye-Waller coefficient that modulates the height of the successive k-space delta peaks.

The form of Eq 2.18 served to motivate the introduction of the XPFC correlation kernel. The more modes included, the sharper the real space Gaussian becomes and thus the more stable and precise the description of the periodic structure in question. However, smaller and smaller numerical grid spacings are required to resolve these narrower structures; it has been found [19] that the increase in stability from additional frequency modes is minor compared to the resulting computational cost. As such, we retain only the first peak corresponding to each family of lattice planes.

When constructing the correlation function itself we represent the delta functions as Gaussians with finite widths α_i, of the form $\exp\left[-(\vec{k}-\vec{k}_i)^2/2\alpha_i^2\right]$, where the $\vec{k}_i$ are the reciprocal lattice vectors. The Debye-Waller term presents an entry point for temperature into the XPFC model through the σ parameter, which can be rigorously connected to the temperature scale. Constants β_i and ρ_i are also included, representing the number of planar symmetries and the in-plane atomic density, respectively. The choice of α_i acts as a control on the stiffness of the model, and directly affects the width of the solid-liquid interface. Additionally, the ratio between the different α_i values can be used to introduce an anisotropy between the elastic coefficients of the crystal. It has been shown [19] that to maintain elastic isotropy within a particular crystal structure, the ratio between the α_i must equal the ratio between the values of the corresponding peak positions. The full correlation function term around each dominant frequency mode is

$$\hat{C}_2(\vec{k}) = e^{-\frac{\sigma^2\vec{k}_i^2}{2\rho_i\beta_i}} e^{-\frac{(\vec{k}-\vec{k}_i)^2}{2\alpha_i^2}} \tag{2.20}$$

For any given $\vec{k}$-value in reciprocal space, the full correlation function is taken as the envelope of the superposition of the $\hat{C}_2$ for each contributing $\vec{k}_i$.

The full XPFC model has the form

$$\frac{\Delta F}{\bar{\rho} k_B T} = \Delta F_{id} + \Delta F_{ex} \tag{2.21}$$

where here we have set the lattice constant $a = 1$. The form of the XPFC correlation function is a purely reciprocal space construction, and as such the dynamic equations of the model are solved in reciprocal space and the Fourier transform is taken.

2.2.3 Binary Alloys in XPFC

A binary alloy consists of two component species. While for the pure material it is only necessary to track a single density field, we must now consider the species A and B separately. As previously, we break the free energy down into ΔF_{id} and ΔF_{ex}.

The ideal part can be written in terms of the two components ρ_A and ρ_B as:

$$\frac{\Delta F_{id}}{k_B T} = \int d\vec{r} \left[\rho_A \ln(\rho_A/\rho_A^0) - \delta\rho_A + \rho_B \ln(\rho_B/\rho_B^0) - \delta\rho_B\right] \tag{2.22}$$

where ρ_A^0 and ρ_B^0 are the reference densities of each respective component. Rather than expressing the energy in terms of these two components, it is more instructive to work in terms of a total density ρ and a fractional concentration field c, defined as

$$\begin{aligned} \rho &= \rho_A + \rho_B \\ c &= \frac{\rho_B}{\rho_A + \rho_B} = \frac{\rho_B}{\rho} \end{aligned} \tag{2.23}$$

We additionally define a reference density $\rho^0 = \rho_A^0 + \rho_B^0$ and reference concentration $c_0 = \rho_B^0/\rho^0$. As with the case of a pure material we then write a total dimensionless density $n = \rho/\rho^0 - 1$. Applying all of these transformations allows us to write the ideal energy in the dimensionless form

$$\frac{\Delta F_{id}}{k_B T \rho^0} = \int d\vec{r}(n+1)\left\{(1-c)\ln\left(\frac{1-c}{1-c_0}\right) + c\ln\left(\frac{c}{c_0}\right)\right\} + (n+1)\ln(n+1) - n \tag{2.24}$$

We again expand the nonlinear terms in n to get

$$\begin{aligned} \frac{\Delta F_{id}}{k_B T \rho^0} &= \int d\vec{r}\frac{n^2}{2} - \eta\frac{n^3}{6} + \chi\frac{n^4}{12} + (n+1)\left\{(1-c)\ln\left(\frac{1-c}{1-c_0}\right) + c\ln\left(\frac{c}{c_0}\right)\right\} \\ &= \int d\vec{r}\frac{n^2}{2} - \eta\frac{n^3}{6} + \chi\frac{n^4}{12} + (n+1)\Delta F_{mix}(c) \end{aligned} \tag{2.25}$$

The first set of terms are the same as those seen in the pure material, and express the individual free energies of the two separate fields. The last term, as the notation suggests, represents the entropic mixing of the two fields and their interactions with each other.

We now consider the excess free energy which, as previously, contains a two-point correlation function. However, unlike the pure case, we must now consider three types of interactions: A-A, B-B, and A-B. We can begin with a summation using the same form as in the pure case

$$\Delta F_{ex} = -\int d\vec{r}\frac{1}{2}\sum_{ij}\delta\rho_i(\vec{r})\int d\vec{r'}C_2^{ij}(|\vec{r}-\vec{r'}|)\delta\rho_j(\vec{r'}) \tag{2.26}$$

where i,j sum over the two species.

Rewriting Eq 2.26 in terms of variables c and n, we note that the correlation function acting on a constant (i.e. the $\vec{k} = 0$ mode) has zero contribution. We additionally make the assumption that the concentration field is slowly varying as compared to density,

which allows us to say that $c(\vec{r}) \approx c(\vec{r'})$. We obtain the form [24]

$$\Delta F_{ex} = \int d^3\vec{r} \left\{ \frac{-n}{2} \int d^3\vec{r}' \left(C^n_{eff} n' + C^c_{eff} c' \right) - \frac{(c - c_0)}{2} \int d^3\vec{r}' \left(C^{c_0 n}_{eff} n' + C^{c_0 c}_{eff} c' \right) \right\} \tag{2.27}$$

where

$$\begin{aligned} C^n_{eff} &= c^2 C_2^{BB} + (1-c)^2 C_2^{AA} + c(1-c)(C_2^{BA} + C_2^{AB}) \\ C^c_{eff} &= c(C_2^{BB} - C_2^{BA}) - (1-c)(C_2^{AA} - C_2^{AB}) \\ C^{c_0 n}_{eff} &= c(C_2^{BB} - C_2^{AB}) - (1-c)(C_2^{AA} - C_2^{BA}) \\ C^{c_0 c}_{eff} &= C_2^{BB} + C_2^{AA} - (C_2^{BA} + C_2^{AB}) \end{aligned} \tag{2.28}$$

These expressions are obtained explicitly in Appendix A.

Coarse graining these terms (i.e.looking at their behaviour on length scales much greater than that of the lattice constant) using the same prescription as with the PFC model for a pure material, and taking advantage of the fact that c is a slow-varying field, the remaining expression is

$$\Delta F_{ex} = \int d^3\vec{r} \left(\alpha |\nabla c|^2 - \frac{n}{2} \int d^3\vec{r}' C^n_{eff}(|\vec{r} - \vec{r'}|) n' \right) \tag{2.29}$$

We now consider the form of the correlation term, which is made up of elemental components C^{AA}, C^{AB}, C^{BA}, and C^{BB}. The mixed terms AB and BA represent the cases where A atoms are arranged in the B preferred crystal structure, and vice versa. These terms can be approximated by interpolating between AA and BB correlations, allowing us to re-express C^n_{eff} in Eq 2.28 as

$$\begin{aligned} C^n_{eff} &= X_1(c) C_2^{AA} + X_2(c) C_2^{BB} \\ X_1(c) &= 1 - 3c^2 + 2c^3 \\ X_2(c) &= 1 - 3(1-c)^2 + 2(1-c)^3 \end{aligned} \tag{2.30}$$

where X_1 and X_2 are composition-modulated interpolation functions [24]. C_2^{AA} and C_2^{BB} are constructed from the dominant lattice peaks of the preferred crystal structures of each respective species, as explained above in detail for the pure model. The full binary

XPFC free energy is then:

$$\frac{\Delta F}{kT\rho^0} = \int d\vec{r}(\frac{n^2}{2} - \eta\frac{n^3}{6} + \chi\frac{n^4}{12} + (n+1)\Delta F_{mix}(c) \\ +\alpha|\nabla c|^2 - \frac{1}{2}n\int d\vec{r'}\left[X_1(c)C_2^{AA} + X_2(c)C_2^{BB}\right]n') \tag{2.31}$$

A note: the X_1 and X_2 interpolation functions have been introduced to interpolate between the fundamental interactions contained in the species correlation functions C_2^{AA} and C_2^{BB}. The precise form of these interpolation functions is not known, but can be made quantitative by demanding that the equilibrium properties of the alloy system (e.g. the phase diagram and free energy differences) are reproduced, and appropriate free energy changes between solid phases are achieved.

Chapter 3

Methodology

3.1 XPFC Dynamics of the Pure Material

In this section we outline the derivation of the dynamic equations of motion for the XPFC model, and their numerical integration. There is more than one numerical iteration scheme possible. To begin with we present a scheme used to study dynamics in the majority of XPFC simulations to date. We then introduce a method that makes use of relaxed constraints to obtain a significant reduction of the time scales required to attain equilibrated structures.

3.1.1 Conserved Diffusive Dynamics

The pure XPFC model equilibrates via diffusion of density through the system. We require that the density flow obey flux conservation, and thus we need a continuity equation for a conserved quantity. The general form is

$$\frac{\partial x}{\partial t} + \nabla \cdot \vec{J} = 0 \tag{3.1}$$

where $\vec{J}$ represents flux in the quantity x. We now require an expression for $\vec{J}$.

We are considering local changes in particle number, and as such must establish the local driving force depending on number of particles. We look to the entropy of the system;

changes in entropy are written as

$$dS = \frac{1}{T}dU + \frac{p}{T}dV - \frac{\mu}{T}dN \tag{3.2}$$

where U is the internal energy of the system, μ is chemical potential, p is pressure, V the volume and T temperature. We then get an expression for change in entropy with changing particle number.

$$\frac{dS}{dN} = -\frac{\mu}{T} \tag{3.3}$$

and

$$\frac{dS}{dU} = -\frac{1}{T} \tag{3.4}$$

The basic premise of most non-equilibrium transport theories is that Eq 3.2 can be applied locally to derive the local flux of mass through a volume element according to

$$\vec{J} = M_{10}\nabla\frac{1}{T} + M_{11}\nabla\frac{\mu}{T} \tag{3.5}$$

where M_{10} and M_{11} are called Osanger coefficients. In our case we consider only uniform temperature, which implies that the first term is zero. Setting $M_{11} \equiv M$ for simplicity, we thus write flux in terms of this driving force as

$$\vec{J} = -M\nabla\frac{\mu}{T} = -\frac{M}{T}\nabla\mu \tag{3.6}$$

Here M is a constant coefficient representing solute mobility, and we write $\bar{M} \equiv M/T \approx M/T_c$, which is assumed to be valid to lowest order close to the transition temperature T_c. The form we have recovered is effectively Fick's law of diffusion. Finally, the chemical potential is defined from classical density functional theory as

$$\mu = \frac{\delta F[n(\vec{r})]}{\delta n} \tag{3.7}$$

We substitute the expression for flux into Eq 3.1. The dynamics become

$$\frac{\partial n}{\partial t} = \nabla \cdot \left(\bar{M}\nabla\frac{\delta F}{\delta n}\right) = \bar{M}\nabla^2\left(\frac{\delta F}{\delta n}\right) \tag{3.8}$$

which is the form of the Cahn-Hilliard equation [25].

3.1.2 Nonlocal Dynamics

The diffusional dynamics equation is advantageous in that it allows the system to evolve realistically in terms of local diffusion of solute. As such it gives a good illustration of the behaviour of the system both on the path to and at equilibrium. However, this also restricts the model to operating at diffusive timescales.

It is possible to obtain a significant decrease in required simulation time to reach equilibrium by no longer restricting the solute to move via diffusion, the tradeoff being that transient results may be unphysical and can't be considered meaningful. For the purposes of our investigation, only the equilibrium profiles of conserved and nonconserved fields are relevant and as such this method is ideal. The prescription is outlined in Ref [26] and is based around relaxing the requirement of local flux conservation. Only global conservation of the order parameter is enforced via the chemical potential, which plays the role of a Lagrange multiplier. This permits a decrease in the order parameter at some point A to occur with a corresponding increase at point B, without necessarily having any changes carried through the intervening space. This swapping process allows for faster equilibration of the model.

This *nonlocal* method (as we shall henceforth refer to it) is illustrated as follows for the case of a pure material. The global conservation condition is expressed as

$$\int n(\vec{r})d\vec{r} - Vn_0 = 0 \tag{3.9}$$

where n_0 is the average density of the system and V is the system volume. The free energy is then rewritten as

$$\tilde{F} = F + \mu \left[\int n(\vec{r})d\vec{r} - Vn_0 \right] \tag{3.10}$$

where the chemical potential μ acts as a Lagrange multiplier. Equilibrium is attained via the pseudo-time equation of motion for the density field:

$$\frac{\partial n}{\partial t} = -\frac{\delta F}{\delta n} + \mu \tag{3.11}$$

where μ is calculated at each timestep according to

$$\mu = \frac{1}{V} \int \frac{\delta F[n(\vec{r})]}{\delta n} d\vec{r} \tag{3.12}$$

It should be noted that additional speed increase can be obtained by setting μ to an externally imposed constant value. However, doing so relaxes the final constraint of global density conservation. Due to the degeneracy of n_0 values corresponding to a single chemical potential at phase coexistence, the non-conserved Eq 3.11 frees the system to move anywhere along the common tangent line of slope μ between the coexisting liquid and solid free energies. In minimizing the free energy, the system will move towards whichever curve gives the lowest energy minimum. This will result in the system equilibrating at either the liquidus or solidus line of the system, which means that the sample will either entirely melt or entirely solidify. This constant μ method has its uses. For example, it was effective in studying grain boundaries in fully solidified systems [26]. However as it is incapable of stabilizing solid-liquid coexistence, it will not be discussed further here.

Due to the notable decrease in equilibration time obtained by switching to the nonlocal method, the XPFC results presented in this thesis were obtained using this method.

3.1.3 Numerical Integration of the Non-Local Model in Reciprocal Space

In order to simulate equations describing a continuous system, we assume that it is possible to discretize the system into a series of elements that are all locally at thermodynamic equilibrium. The free energies from these discrete elements are used to calculate local driving forces that evolve the system towards a global equilibrium. In the limit of vanishing element size, such a coarse graining procedure leads to continuum equations such as those described above. When solving such equations numerically, we are essentially discretizing space and time into elements that a computer can process. This subsection describes the iterative scheme that we use to model the XPFC equations numerically.

To solve the dynamic equations numerically on the discrete lattice, we begin with the following approximation:

$$\frac{\partial n(\vec{r})}{\partial t} \approx \frac{n^{t+1}(i,j) - n^{t}(i,j)}{\delta t} \tag{3.13}$$

This is applied to Eq 3.11 (or Eq 3.8) and the functional derivative $\delta F/\delta n$ is explicitly evaluated using the form of the XPFC free energy. For the nonlocal method this gives

$$\frac{n^{t+1} - n^{t}}{\Delta t} = -\left(n - \frac{\eta}{2}n^2 + \frac{\chi}{3}n^3 - \int C_2(|\vec{r} - \vec{r'}|)n(\vec{r'})d\vec{r'}\right) + \mu \tag{3.14}$$

In the XPFC model, the correlation function has an analytical form in reciprocal space only, so rewriting the Fourier transformed expression gives:

$$\frac{\hat{n}_k^{t+1} - \hat{n}_k^t}{\Delta t} = -\hat{n}_k^{t+1} - \hat{C}_2(\vec{k})\hat{n}_k^{t+1} - \left[\frac{\eta}{2}n^2 + \frac{\chi}{3}n^3 + \mu\right]_k^t \tag{3.15}$$

where the final bracketed expression contains all of the nonlinear terms in n. The superscripts t and $t+1$ indicate at which timestep the term is being evaluated. All nonlinear terms are evaluated at time t and all linear terms at $t+1$ in what is called a *semi-implicit* method. The nonlinear terms are evaluated separately in real space and then transformed as a single term. All transforms are performed using a parallel (MPI) fast Fourier transform routine (FFTW). Finally note that the realspace convolution in the correlation function has become a simple product in kspace. Eq 3.15 can then be rearranged to obtain

$$\hat{n}_k^{t+1} = \left[\frac{1}{1 + \Delta t(1 + \hat{C}_2(\vec{k}))}\right]\left(\hat{n}_k^t - \Delta t\left[\frac{\eta}{2}n^2 + \frac{\chi}{3}n^3 + \mu\right]_k^t\right) \tag{3.16}$$

The overall prescription is thus to initialize a density profile (using the mode approximation form in Eq 2.12), then at each timestep to transform the density field (or the nonlinear function of the density field) via FFTW, update the field in k-space according to Eq 3.16, and transform back to real space.

3.2 Dynamics of the Binary Alloy

It is possible to extend the same general methods above to an alloy. We describe the process for a binary alloy model. While the basic prescription is unchanged, there are some special considerations worth mentioning.

In particular, note that we now have two number density fields, ρ_A and ρ_B, representing species A and B. Following the variable transformations described in Eq 2.23, we are able to make contact with the XPFC functional variables, n and c.

3.2.1 Alloy Conserved Diffusive Dynamics

The diffusive dynamics method for the alloy [24] takes as a starting point the two fields n and c. In one of the approximations considered herein, the assumption is made that

two chemical potentials based on the respective fields can be defined as follows:

$$\begin{aligned}\mu_n &= \frac{\delta F}{\delta n} \\ \mu_c &= \frac{\delta F}{\delta c}\end{aligned} \tag{3.17}$$

In analogy with the pure method we then trivially obtain the following expressions:

$$\begin{aligned}\frac{\partial n}{\partial t} &= \nabla \cdot M_n \nabla \frac{\delta F}{\delta n} \\ &= \nabla \cdot M_n \nabla \left\{ n - \eta \frac{n^2}{2} + \chi \frac{n^3}{3} + \Delta F_{mix} - \int \left[X_1(c) C_2^{AA} + X_2(c) C_2^{BB} \right] n' \right\}\end{aligned} \tag{3.18}$$

and

$$\begin{aligned}\frac{\partial c}{\partial t} &= \nabla \cdot M_c \nabla \frac{\delta F}{\delta c} \\ &= \nabla \cdot M_c \nabla \left\{ (n+1) \frac{\delta \Delta F_{mix}}{\delta c} - \alpha \nabla^2 c - \frac{1}{2} n \int \left[\frac{\delta X_1}{\delta c} C_2^{AA} + \frac{\delta X_2}{\delta c} C_2^{BB} \right] n' \right\}\end{aligned} \tag{3.19}$$

where M_n and M_c are the mobilities of the respective fields. Equations 3.18 and 3.19 have previously been used for binary XPFC studies.

3.2.2 Alloy Nonlocal Dynamics

The nonlocal dynamics method is also known as *pseudo* or *fictitious* dynamics. As mentioned previously, its purpose is solely to rapidly converge the fields c and n to the equilibrium state defined by Eq 3.18 and 3.19.

We consider two choices of Lagrange multiplier for the alloy model.

We once again assume Eq 3.17, and integrate both components of these expressions over the system volume. This yields

$$\mu_n = \frac{1}{V} \int \frac{\delta F[n(\vec{r}), c(\vec{r})]}{\delta n} d\vec{r} \tag{3.20}$$

$$\mu_c = \frac{1}{V} \int \frac{\delta F[n(\vec{r}), c(\vec{r})]}{\delta c} d\vec{r} \tag{3.21}$$

Note that Eq 3.20 and 3.21 constrain the two chemical potentials to be constant in a mean, integrated sense, but *not* locally. With these expressions for μ_n and μ_c, nonlocal

dynamics for n and c are given by

$$\begin{aligned}\frac{\partial n}{\partial t} &= -\frac{\delta F}{\delta n} + \mu_n \\ \frac{\partial c}{\partial t} &= -\frac{\delta F}{\delta c} + \mu_c\end{aligned} \tag{3.22}$$

This description is appealing in its simplicity and elegance, however note that it effectively treats the evolution of the density and concentration fields as independent of each other. This is strictly speaking incorrect, since they are by definition connected via ρ_A and ρ_B (Eq 2.23) and thus a second derivation, beginning from the grand potential functional in ρ_A and ρ_B, is considered.

3.2.2.1 Derivation from DFT

We begin with the form of the grand potential, defined in terms of the fundamental fields ρ_A and ρ_B [27]

$$\Omega[\rho_A, \rho_B] = F[\rho_A, \rho_B] - \mu_A \int \rho_A(\vec{r}) d\vec{r} - \mu_B \int \rho_B(\vec{r}) d\vec{r} \tag{3.23}$$

From classical density functional theory, equilibrium is defined to occur when the grand potential functional is minimized, leading to

$$\begin{aligned}\frac{\delta \Omega[\rho_A, \rho_B]}{\delta \rho_A} = 0 \Longrightarrow \frac{\delta F[\rho_A, \rho_B]}{\delta \rho_A} = \mu_A^{eq} \\ \frac{\delta \Omega[\rho_A, \rho_B]}{\delta \rho_B} = 0 \Longrightarrow \frac{\delta F[\rho_A, \rho_B]}{\delta \rho_B} = \mu_B^{eq}\end{aligned} \tag{3.24}$$

We perform the variable transforms laid out in Eq 2.23, noting that we can also write

$$\begin{aligned}\rho_A &= (1-c)(n+1)\rho^0 \\ \rho_B &= c(n+1)\rho^0 \\ \rho &= (n+1)\rho^0\end{aligned} \tag{3.25}$$

The final expressions for free energy are normalized by the reference density ρ^0; as such for convenience's sake we will omit this factor from here on out.

We proceed as follows:

$$\begin{aligned}\frac{\delta\Omega[\rho_A,\rho_B]}{\delta\rho_A} &= \frac{\delta\Omega}{\delta n}\frac{\delta n}{\delta\rho}\frac{\delta\rho}{\delta\rho_A} + \frac{\delta\Omega}{\delta c}\frac{\delta c}{\delta\rho_A} \\ &= \frac{\delta\Omega}{\delta n} - \frac{c}{n+1}\frac{\delta\Omega}{\delta c} \\ &= \left[\frac{\delta F}{\delta n} - \mu_A\frac{\delta}{\delta n}\int\rho_A d\vec{r} - \mu_B\frac{\delta}{\delta n}\int\rho_B d\vec{r}\right] \\ &\quad -\frac{c}{n+1}\left[\frac{\delta F}{\delta c} - \mu_A\frac{\delta}{\delta c}\int\rho_A d\vec{r} - \mu_B\frac{\delta}{\delta c}\int\rho_B d\vec{r}\right] \\ &= 0 \end{aligned} \tag{3.26}$$

Rearranging the last line to solve for μ_A gives

$$\mu_A = \frac{\delta F}{\delta n} - \frac{c}{n+1}\frac{\delta F}{\delta c} \tag{3.27}$$

Doing the same for ρ_B

$$\begin{aligned}\frac{\delta\Omega[\rho_A,\rho_B]}{\delta\rho_B} &= \frac{\delta\Omega}{\delta n}\frac{\delta n}{\delta\rho}\frac{\delta\rho}{\delta\rho_B} + \frac{\delta\Omega}{\delta c}\frac{\delta c}{\delta\rho_B} \\ &= \frac{\delta\Omega}{\delta n} + \frac{(1-c)}{n+1}\frac{\delta\Omega}{\delta c} \\ &= \left[\frac{\delta F}{\delta n} - \mu_A\frac{\delta}{\delta n}\int\rho_A d\vec{r} - \mu_B\frac{\delta}{\delta n}\int\rho_B d\vec{r}\right] \\ &\quad +\frac{(1-c)}{n+1}\left[\frac{\delta F}{\delta c} - \mu_A\frac{\delta}{\delta c}\int\rho_A d\vec{r} - \mu_B\frac{\delta}{\delta c}\int\rho_B d\vec{r}\right] \\ &= 0 \end{aligned} \tag{3.28}$$

and

$$\mu_B = \frac{\delta F}{\delta n} + \frac{(1-c)}{n+1}\frac{\delta F}{\delta c} \tag{3.29}$$

We can use these expressions to simplify Euler-Lagrange equations for n and c. First we subtract Eq 3.27 from Eq 3.29, and in the process define $\mu^{eq} = \mu_B^{eq} - \mu_A^{eq}$. This gives

$$\frac{\delta F}{\delta c} = (n(\vec{r})+1)\mu^{eq} \tag{3.30}$$

and

$$\mu^{eq} = \frac{1}{V}\int\frac{1}{(n+1)}\frac{\delta F}{\delta c}d\vec{r} \tag{3.31}$$

Finally, substituting Eq 3.30 into Eq 3.27, we solve to obtain a second equation for n.

$$\frac{\delta F}{\delta n} = c(\vec{r})\mu^{eq} + \mu_A \tag{3.32}$$

where

$$\mu_A = \frac{1}{V}\int \left[\frac{\delta F}{\delta n} - \frac{c}{n+1}\frac{\delta F}{\delta c}\right] d\vec{r} \tag{3.33}$$

We thus end up with a set of evolution equations that explicitly tie the behaviour of the density and concentration fields to the variable transforms Eq 2.23, making manifest the connection between the fields n and c and the fundamental species densities ρ_A and ρ_B.

Note that the method described by Eq 3.22 makes the same assumption as the conserved diffusive dynamics (Eq 3.18, 3.19), namely, that the fields n and c are independent and as such that the alloy grand potential can be represented by

$$\Omega[n, c] = F[n, c] - \mu_n \int n(\vec{r})d\vec{r} - \mu_c \int c(\vec{r})d\vec{r} \tag{3.34}$$

The nonlocal method Eq 3.22 and the conserved diffusive dynamics are thus expected to return the same equilibrium profiles; trial runs reveal this to be the case for both n and c fields.

The grand potential Eq 3.23, resulting in the evolution equations Eq 3.30, 3.32 derived above, cannot be manipulated to agree with Eq 3.34. As such we expect different results from this method and indeed find that resulting equilibrium profiles are shifted somewhat. In what follows, the latter DFT form of the nonlocal XPFC alloy dynamics will be used, because of its self-consistent connection to the density fields. It is found, however, that the results of this thesis do not change qualitatively whether the simplified (Eq 3.22) or the self-consistent (Eq 3.30, 3.32) formulation of the Euler Lagrange equations are used to solve for the interface energy.

3.3 Binary Alloy Amplitude Model

We find in practice that it is not trivial to numerically stabilize an equilibrium solid-liquid interface in the binary alloy XPFC model with variable average density. This was not a problem in past work done with the binary PFC or XPFC models; however, no previous PFC alloy study has incorporated density changes in the investigation of dynamical or equilibrium interfacial properties and structure. In order to avoid practical issues associated with solving the above equilibrium density and concentration equations, we also looked to the long wavelength limit of the alloy XPFC equations, wherein we work with a coarse grained representation that emerges from the microscopic equations

(Eq 3.30, 3.32). Such coarse grained equations have become known in the literature as *amplitude* equations.

We obtain an alloy amplitude model by coarse-graining the binary XPFC free energy, presented in detail in section 2.2.3, to obtain an equivalent phase field model. This method requires us to evolve not only the concentration and average density fields, but also fields representing the amplitudes of the respective oscillatory terms in the density mode expansion (Eq 2.12). For a square-triangle alloy system, the full mode expansion employed to capture either square or triangular crystal symmetries is

$$n(\vec{r}) = n_0 + \sum_{j}^{2} A_j e^{i\vec{k}_j \cdot \vec{r}} + \sum_{l}^{2} B_l e^{i\vec{q}_l \cdot \vec{r}} + \sum_{m}^{3} C_m e^{i\vec{Q}_m \cdot \vec{r}} \tag{3.35}$$

where $n_0(\vec{r})$ is the average density, the A_j and B_l are the generally complex amplitudes for the square $(1,0)$ and $(1,1)$ directions, respectively, and the C_m are the amplitudes for the triangle. This mode expansion is substituted into the binary XPFC free energy, which is then coarse-grained. Details of the procedure are presented in Appendix B.

The final free energy functional has the form

$$
\begin{aligned}
F_{cg} = \int d\vec{r} \big\{ & \left(1 - \eta n_0 + \chi n_0^2\right) \left(A_1^2 + A_2^2 + B_1^2 + B_2^2 + C_1^2 + C_2^2 + C_3^2\right) \\
& + \frac{1}{2} n_0^2 - \frac{\eta}{6} n_0^3 + \frac{\chi}{12} n_0^4 + \omega(n_0 + 1)\Delta F_{mix}(c) + \alpha |\nabla c|^2 \\
& + \left(4\chi n_0 - 2\eta\right)\left(A_1 A_2 B_1 + A_1 A_2 B_2 + C_1 C_2 C_3\right) \\
& + \frac{\chi}{2}\left(A_1^4 + A_2^4 + B_1^4 + B_2^4 + C_1^4 + C_2^4 + C_3^4\right) \\
& + 2\chi A_1^2 \left(B_1 B_2 + C_2 C_3\right) + 2\chi A_1^2 \left(A_2^2 + B_1^2 + B_2^2 + C_1^2 + C_2^2 + C_3^2\right) \\
& + 2\chi A_1^2 B_1 B_2 + 2\chi A_2^2 \left(B_1^2 + B_2^2 + C_1^2 + C_2^2 + C_3^2\right) \\
& + 2\chi B_1^2 \left(B_2^2 + C_1^2 + C_2^2 + C_3^2\right) + 2\chi B_2^2 \left(C_1^2 + C_2^2 + C_3^2\right) \\
& + 2\chi C_1^2 \left(C_2^2 + C_3^2\right) + 2\chi C_2^2 C_3^2 + 4\chi B_1 B_2 B C_2 C_3 \\
& - 2(A_1^2 + A_2^2)\left(X_1(c)\hat{C}_2^{AA}(|\vec{k}_{10}^A|) + X_2(c)\hat{C}_2^{BB}(|\vec{k}_{10}^A|)\right) \\
& - 2(B_1^2 + B_2^2)\left(X_1(c)\hat{C}_2^{AA}(|\vec{k}_{11}^A|) + X_2(c)\hat{C}_2^{BB}(|\vec{k}_{11}^A|)\right) \\
& - 2(C_1^2 + C_2^2 + C_3^2)\left(X_1(c)\hat{C}_2^{AA}(|\vec{k}_{10}^B|) + X_2(c)\hat{C}_2^{BB}(|\vec{k}_{10}^B|)\right) \\
& - \frac{1}{|\vec{k}_{10}^A|^2}\left(X_1(c)\hat{C''}_2^{AA}(|\vec{k}_{10}^A|) + X_2(c)\hat{C''}_2^{BB}(|\vec{k}_{10}^A|)\right)\left[\left|\left(i\vec{k}_{10}^A \cdot \nabla\right) A_1\right|^2 + \left|\left(i\vec{k}_{10}^A \cdot \nabla\right) A_2\right|^2\right] \\
& - \frac{1}{|\vec{k}_{11}^A|^2}\left(X_1(c)\hat{C''}_2^{AA}(|\vec{k}_{11}^A|) + X_2(c)\hat{C''}_2^{BB}(|\vec{k}_{11}^A|)\right)\left[\left|\left(i\vec{k}_{11}^A \cdot \nabla\right) B_1\right|^2 + \left|\left(i\vec{k}_{11}^A \cdot \nabla\right) B_2\right|^2\right] \\
& - \frac{1}{|\vec{k}_{10}^B|^2}\left(X_1(c)\hat{C''}_2^{AA}(|\vec{k}_{10}^B|) + X_2(c)\hat{C''}_2^{BB}(|\vec{k}_{10}^B|)\right) \\
& \left[\left|\left(i\vec{k}_{10}^B \cdot \nabla\right) C_1\right|^2 + \left|\left(i\vec{k}_{10}^B \cdot \nabla\right) C_2\right|^2 + \left|\left(i\vec{k}_{10}^B \cdot \nabla\right) C_3\right|^2\right] \big\}
\end{aligned}
\tag{3.36}
$$

where $\hat{C''}_2^{IJ}$ is the second derivative of the IJ correlation function, evaluated at the indicated reciprocal lattice vector length.

For many applications it is sufficient to make the simplifying assumption that each set of amplitudes is real and has the same value, that is, $A_1 = A_2 = A$ and so on. However, in order to retain an explicit angular dependence with respect to interface orientation, it is necessary to track all of the amplitudes separately. We do still assume that they are real; the main drawback of this assumption is that we lose the potential for describing topological defects in the bulk, which is not the focus of this study. We show the necessity of separate amplitudes explicitly in what follows.

The angular dependence comes into the dot product terms of Eq 3.36; for example:

$$\sum_j^2 |(i\vec{k}_j \cdot \nabla)\vec{A}_j|^2 = \sum_j^2 (\vec{k}_j \cdot \nabla \vec{A}_j)^2 = \sum_j^2 (\vec{k}_j \cdot \hat{n})^2 (\nabla A_j)^2 \tag{3.37}$$

which, in the case where $A_j = A$, simplifies to

$$(\nabla A)^2 \sum_j (\vec{k}_j \cdot \hat{n})^2 \tag{3.38}$$

We obtain different orientations by performing a rotation on the $\vec{k}_j$ vectors of the reciprocal lattice,

$$k'_x = k_x \cos\theta - k_y \sin\theta \tag{3.39}$$

$$k'_y = k_y \cos\theta + k_x \sin\theta \tag{3.40}$$

where for the 1D simulation only the k'_x component is retained. For any θ we then obtain

$$(\nabla A)^2 \sum_j (k_{jx} \cos\theta - k_{jy} \sin\theta)^2 \tag{3.41}$$

The reciprocal lattice vectors for the respective crystal structures are as follows.

$$\begin{array}{lll} \vec{k}_1^{\text{square}} = 2\pi(1,0) & \vec{k}_2^{\text{square}} = 2\pi(0,1) & \\ \vec{q}_1^{\text{square}} = 2\pi(1,1) & \vec{q}_2^{\text{square}} = 2\pi(1,-1) & \\ \vec{Q}_1^{\text{tri}} = 2\pi\left(0, \frac{2}{\sqrt{3}}\right) & \vec{Q}_2^{\text{tri}} = 2\pi\left(1, \frac{-1}{\sqrt{3}}\right) & \vec{Q}_3^{\text{tri}} = 2\pi\left(-1, \frac{-1}{\sqrt{3}}\right) \end{array} \tag{3.42}$$

Inserting, for example, $\vec{k}_1$ and $\vec{k}_2$ into Eq 3.41, we can see that the angular dependence is lost:

$$\begin{aligned} & (\nabla A)^2 \left[(-2\pi \sin\theta)^2 + (2\pi \cos\theta)^2\right] \\ = & (\nabla A)^2 \left[4\pi 2(\sin^2\theta + \cos^2\theta)\right] \\ = & 4\pi^2 (\nabla A)^2 \end{aligned} \tag{3.43}$$

Similarly for both the $\vec{q}$ and $\vec{Q}$, we obtain a constant of $8\pi^2$ multiplying the gradient term, regardless of the choice of angle θ.

This loss of rotational dependence in the gradient terms of a PFC amplitude theory can be remedied by tracking each amplitude field separately rather than making this

simplification. This gives a total of seven evolving amplitude fields for the square-triangle system. In initializing these fields it is sufficient to seed all of the A_j amplitudes with the same initial profile. It is important to note however that this model is necessarily more sensitive to amplitude values than the XPFC model, and as such when obtaining the phase diagram we must solve separately for both the A and B amplitudes of the square phase, rather than making the assumption that $B = fA$ for some appropriate choice of f, as has been the case for most XPFC work to date [19].

In order to obtain the evolution equations for the fields we take variational derivatives of Eq 3.36. The variational with respect to average density n_0:

$$\begin{aligned}\frac{\delta F}{\delta n_0} &= (2\chi n_0 - \eta)({A_1}^2 + {A_2}^2 + {B_1}^2 + {B_2}^2 + {C_1}^2 + {C_2}^2 + {C_3}^2) \\ &\quad +4\chi(A_1A_2B_1 + A_1A_2B_2 + C_1C_2C_3) + n_0 - \frac{\eta}{2}{n_0}^2 + \frac{\chi}{3}{n_0}^3 + \omega F_{mix}(c)\end{aligned} \tag{3.44}$$

The variational with respect to concentration c:

$$\begin{aligned}\frac{\delta F}{\delta c} &= \omega(n_0+1)\frac{dF_{mix}(c)}{dc} - \alpha\nabla^2 c \\ &\quad -({A_1}^2 + {A_2}^2)\left[\frac{dX_1(c)}{dc}\hat{C}_2^{AA}(|\vec{k}_{10}^A|) + \frac{dX_2(c)}{dc}\hat{C}_2^{BB}(|\vec{k}_{10}^A|)\right] \\ &\quad -({B_1}^2 + {B_2}^2)\left[\frac{dX_1(c)}{dc}\hat{C}_2^{AA}(|\vec{k}_{11}^A|) + \frac{dX_2(c)}{dc}\hat{C}_2^{BB}(|\vec{k}_{11}^A|)\right] \\ &\quad -({C_1}^2 + {C_2}^2 + {C_3}^2)\left[\frac{dX_1(c)}{dc}\hat{C}_2^{AA}(|\vec{k}_{10}^B|) + \frac{dX_2(c)}{dc}\hat{C}_2^{BB}(|\vec{k}_{10}^B|)\right] \\ &\quad -\frac{1}{|\vec{k}_{10}^A|^2}\left[\frac{dX_1(c)}{dc}\hat{C''}_2^{AA}(|\vec{k}_{10}^A|) + \frac{dX_2(c)}{dc}\hat{C''}_2^{BB}(|\vec{k}_{10}^A|)\right](|k'_{1x}\nabla A_1|^2 + |k'_{2x}\nabla A_2|^2) \\ &\quad -\frac{1}{|\vec{k}_{11}^A|^2}\left[\frac{dX_1(c)}{dc}\hat{C''}_2^{AA}(|\vec{k}_{11}^A|) + \frac{dX_2(c)}{dc}\hat{C''}_2^{BB}(|\vec{k}_{11}^A|)\right](|q'_{1x}\nabla B_1|^2 + |q'_{2x}\nabla B_2|^2) \\ &\quad -\frac{1}{|\vec{k}_{10}^B|^2}\left[\frac{dX_1(c)}{dc}\hat{C''}_2^{AA}(|\vec{k}_{10}^B|) + \frac{dX_2(c)}{dc}\hat{C''}_2^{BB}(|\vec{k}_{10}^B|)\right](|Q'_{1x}\nabla C_1|^2 + |Q'_{2x}\nabla C_2|^2 + |Q'_{3x}\nabla C_3|^2)\end{aligned} \tag{3.45}$$

The variationals with respect to each of the amplitudes:

$$\begin{aligned}\frac{\delta F}{\delta A_1} &= 4\chi A_1({A_2}^2 + {B_1}^2 + {B_2}^2 + {C_1}^2 + {C_2}^2 + {C_3}^2) \\ &+2\chi({A_1}^3 + 2A_1B_1B_2) + (4\chi n_0 - 2\eta)(A_2B_1 + A_2B_2) + 2A_1(1 - \eta n_0 + \chi {n_0}^2) \\ &-2A_1\left[X_1(c)\hat{C}_2^{AA}(|\vec{k}_{10}^A|) + X_2(c)\hat{C}_2^{BB}(|\vec{k}_{10}^A|)\right] \\ &+\frac{1}{|\vec{k}_{10}^A|^2}\left[X_1(c)\hat{C''}_2^{AA}(|\vec{k}_{10}^A|) + X_2(c)\hat{C''}_2^{BB}(|\vec{k}_{10}^A|)\right] 2|k'_{1x}|^2\nabla^2 A_1 \end{aligned} \tag{3.46}$$

$$\begin{aligned}\frac{\delta F}{\delta A_2} &= 4\chi A_2({A_1}^2 + {B_1}^2 + {B_2}^2 + {C_1}^2 + {C_2}^2 + {C_3}^2) \\ &+2\chi({A_2}^3 + 2A_2B_1B_2) + (4\chi n_0 - 2\eta)(A_1B_1 + A_1B_2) + 2A_2(1 - \eta n_0 + \chi {n_0}^2) \\ &-2A_2\left[X_1(c)\hat{C}_2^{AA}(|\vec{k}_{10}^A|) + X_2(c)\hat{C}_2^{BB}(|\vec{k}_{10}^A|)\right] \\ &+\frac{1}{|\vec{k}_{10}^A|^2}\left[X_1(c)\hat{C''}_2^{AA}(|\vec{k}_{10}^A|) + X_2(c)\hat{C''}_2^{BB}(|\vec{k}_{10}^A|)\right] 2|k'_{2x}|^2\nabla^2 A_2 \end{aligned} \tag{3.47}$$

$$\begin{aligned}\frac{\delta F}{\delta B_1} &= 4\chi B_1({A_1}^2 + {A_2}^2 + {B_2}^2 + {C_1}^2 + {C_2}^2 + {C_3}^2) \\ &+2\chi({B_1}^3 + B_2{A_1}^2 + B_2{A_2}^2) + (4\chi n_0 - 2\eta)A_1A_2 + 2B_1(1 - \eta n_0 + \chi {n_0}^2) \\ &-2B_1\left[X_1(c)\hat{C}_2^{AA}(|\vec{k}_{11}^A|) + X_2(c)\hat{C}_2^{BB}(|\vec{k}_{11}^A|)\right] \\ &+\frac{1}{|\vec{k}_{11}^A|^2}\left[X_1(c)\hat{C''}_2^{AA}(|\vec{k}_{11}^A|) + X_2(c)\hat{C''}_2^{BB}(|\vec{k}_{11}^A|)\right] 2|q'_{1x}|^2\nabla^2 B_1 \end{aligned} \tag{3.48}$$

$$\begin{aligned}\frac{\delta F}{\delta B_2} &= 4\chi B_2({A_1}^2 + {A_2}^2 + {B_1}^2 + {C_1}^2 + {C_2}^2 + {C_3}^2) \\ &+2\chi({B_2}^3 + B_1{A_1}^2 + B_1{A_2}^2) + (4\chi n_0 - 2\eta)A_1A_2 + 2B_2(1 - \eta n_0 + \chi {n_0}^2) \\ &-2B_2\left[X_1(c)\hat{C}_2^{AA}(|\vec{k}_{11}^A|) + X_2(c)\hat{C}_2^{BB}(|\vec{k}_{11}^A|)\right] \\ &+\frac{1}{|\vec{k}_{11}^A|^2}\left[X_1(c)\hat{C''}_2^{AA}(|\vec{k}_{11}^A|) + X_2(c)\hat{C''}_2^{BB}(|\vec{k}_{11}^A|)\right] 2|q'_{2x}|^2\nabla^2 B_2 \end{aligned} \tag{3.49}$$

$$\begin{aligned}\frac{\delta F}{\delta C_1} &= 4\chi C_1({A_1}^2 + {A_2}^2 + {B_1}^2 + {B_2}^2 + {C_2}^2 + {C_3}^2) \\ &+2\chi {C_1}^3 + (4\chi n_0 - 2\eta)C_2C_3 + 2C_1(1 - \eta n_0 + \chi {n_0}^2) \\ &-2C_1\left[X_1(c)\hat{C}_2^{AA}(|\vec{k}_{10}^B|) + X_2(c)\hat{C}_2^{BB}(|\vec{k}_{10}^B|)\right] \\ &+\frac{1}{|\vec{k}_{10}^B|^2}\left[X_1(c)\hat{C''}_2^{AA}(|\vec{k}_{10}^B|) + X_2(c)\hat{C''}_2^{BB}(|\vec{k}_{10}^B|)\right] 2|Q'_{1x}|^2\nabla^2 C_1 \end{aligned} \tag{3.50}$$

$$\begin{aligned}\frac{\delta F}{\delta C_2} &= 4\chi C_2({A_1}^2 + {A_2}^2 + {B_1}^2 + {B_2}^2 + {C_1}^2 + {C_3}^2) \\ &+2\chi {C_2}^3 + (4\chi n_0 - 2\eta)C_1C_3 + 2C_2(1 - \eta n_0 + \chi {n_0}^2) \\ &-2C_2\left[X_1(c)\hat{C}_2^{AA}(|\vec{k}_{10}^B|) + X_2(c)\hat{C}_2^{BB}(|\vec{k}_{10}^B|)\right] \\ &+\frac{1}{|\vec{k}_{10}^B|^2}\left[X_1(c)\hat{C''}_2^{AA}(|\vec{k}_{10}^B|) + X_2(c)\hat{C''}_2^{BB}(|\vec{k}_{10}^B|)\right] 2|Q'_{2x}|^2\nabla^2 C_2 \end{aligned} \tag{3.51}$$

$$\begin{aligned}\frac{\delta F}{\delta C_3} &= 4\chi C_2({A_1}^2 + {A_2}^2 + {B_1}^2 + {B_2}^2 + {C_1}^2 + {C_2}^2) \\ &+2\chi {C_3}^3 + (4\chi n_0 - 2\eta)C_1C_2 + 2C_3(1 - \eta n_0 + \chi {n_0}^2) \\ &-2C_3\left[X_1(c)\hat{C}_2^{AA}(|\vec{k}_{10}^B|) + X_2(c)\hat{C}_2^{BB}(|\vec{k}_{10}^B|)\right] \\ &+\frac{1}{|\vec{k}_{10}^B|^2}\left[X_1(c)\hat{C''}_2^{AA}(|\vec{k}_{10}^B|) + X_2(c)\hat{C''}_2^{BB}(|\vec{k}_{10}^B|)\right] 2|Q'_{3x}|^2\nabla^2 C_3 \end{aligned} \tag{3.52}$$

where the $\vec{k'}_{jx}$, $\vec{q'}_{lx}$, and $\vec{Q'}_{mx}$ represent the x components of the rotated reciprocal lattice vectors.

The pseudo-time Euler-Lagrange evolution equations for the concentration and average density fields retain the same form as presented in Eq 3.32 and 3.30 of the previous section. In the amplitude formalism, however, in addition to concentration and density we must also minimize all amplitude fields, which thus follow the non-conserved (so-called Model A) dynamics [14] as described in the above amplitude equations. It is also noted that for this model, the values for chemical potentials μ_{eq} and μ_a are not evolved, and instead are constant values calculated offline via the phase diagram. Calculation of the model's phase diagram will be studied in Chapter 5.

The fields c, n_0, A_j, B_l, C_m are all equilibrated to represent a solid-liquid interface by using the above functional derivatives as driving forces to minimize the total free energy of the system as a function of pseudo time. The resulting equations of motion are:

$${n_0}^{t+1} = {n_0}^t + dtM\left(\mu_{eq}c + \mu_a - \frac{\delta F}{\delta n_0}\right) \tag{3.53}$$

$$c^{t+1} = c^t + dtM\left(\mu_{eq}(n_0 + 1) - \frac{\delta F}{\delta c}\right) \tag{3.54}$$

$${A_j}^{t+1} = {A_j}^t - dtM\frac{\delta F}{\delta A_j} \tag{3.55}$$

$${B_l}^{t+1} = {B_l}^t - dtM\frac{\delta F}{\delta B_l} \tag{3.56}$$

$${C_m}^{t+1} = {C_m}^t - dtM\frac{\delta F}{\delta C_m} \tag{3.57}$$

where j, l, and m run over the indices associated with each amplitude in the density expansion sum of Eq 3.35.

3.4 Determining Anisotropy

3.4.1 Solid-Liquid Interfacial Energy

This section derives the expression used to compute the solid-liquid interfacial energy. The methodology is illustrated first for a single component material, and then expanded to include the alloy systems that will be the main topic of this thesis.

For our calculation of the interfacial energy we begin by considering the grand potential of the system, defined as

$$\Omega = G - \mu N \tag{3.58}$$

where $\Omega = \Omega(V, T, \mu)$, G is the Helmholtz free energy of the system and N is the number of particles. In the case of a pure material, we can rewrite the grand potential as

$$\Omega_{total} = \int d\vec{r} g[n(\vec{r})] - \mu \int d\vec{r} n(\vec{r}) = \int d\vec{r} g[n(\vec{r})] - \mu n_0 V \tag{3.59}$$

where g is the free energy density, $n(\vec{r})$ is the number density field, and n_0 is the average density.

We can in addition calculate the grand potential that would arise from a constant bulk phase. We can choose either the solid or the liquid phase at equilibrium to calculate this; then

$$\Omega_{bulk_{s/l}} = g_{s/l}[n_{s/l}]V - \mu n_{s/l} V \tag{3.60}$$

where the subscripts s/l refer to values in the bulk solid or liquid, respectively.

We define [27]

$$\Omega_{total} = \Omega_{bulk_{s/l}} + \Omega_{interface} \tag{3.61}$$

which states that the total grand potential is made up of one contribution from the bulk region, and another due to the presence of an interface. We isolate for the interface term, which gives us the *total* energy contained within the interface. The unit interfacial energy

γ_{sl} [27] is obtained by dividing this by the length of the interface.

$$\begin{aligned}\gamma_{sl} &= \frac{\Omega_{total} - \Omega_{bulk_{s/l}}}{L_{int}} \\ &= \frac{1}{L_{int}}\left(\int d\vec{r} g[n(\vec{r})] - g_{s/l}[n_{s/l}]V + \mu(n_{s/l} - n_0)V\right)\end{aligned} \tag{3.62}$$

This expression is used to determine γ_{sl} from the pure material simulations.

For the alloy, the two-component version of the grand potential is a simple extension of the ideas presented above. Beginning with the grand potential in terms of ρ_A and ρ_B

$$\Omega[\rho_A, \rho_B] = G[\rho_A, \rho_B] - \mu_A \int d\vec{r}\rho_A - \mu_B \int d\vec{r}\rho_B \tag{3.63}$$

Using the expressions for ρ_A and ρ_B from Eq 3.25 we can rewrite in terms of the alloy model fields, c and n.

$$\begin{aligned}\Omega[\rho_A, \rho_B] &= G[n, c] - \mu_A \int d\vec{r}(1-c)(n+1) - \mu_B \int d\vec{r}c(n+1) \\ &= G[n, c] - \mu_A \int d\vec{r}(n+1) - (\mu_B - \mu_A) \int d\vec{r}c(n+1) \\ &= G[n, c] - \mu_A \int d\vec{r}(n+1) - \mu_{eq} \int d\vec{r}c(n+1)\end{aligned} \tag{3.64}$$

Which, for the alloy, gives us finally

$$\gamma_{sl} = \frac{1}{L_{int}} \int d\vec{r}\left[(g - g_{s/l}) + \mu_A(n_{s/l} - n) + \mu_{eq}(c_{s/l}(n_{s/l}+1) - c(n+1))\right] \tag{3.65}$$

This is the expression used for calculations from the solutions of Eq 3.32 and 3.30, which respect the variable transformations in Eq 2.23.

For the simpler method where n and c are assumed to be decoupled, the assumption is made that

$$\Omega[n, c] = G[n_c] - \mu_n \int d\vec{r}n - \mu_c \int d\vec{r}c \tag{3.66}$$

and the interfacial energy thus becomes

$$\gamma_{sl} = \frac{1}{L_{int}} \int d\vec{r}\left[(g - g_{s/l}) + \mu_n(n_{s/l} - n) + \mu_c(c_{s/l} - c)\right] \tag{3.67}$$

As mentioned previously, the simpler method is formally inconsistent because n and c are in reality coupled. However, we consider both approaches where possible given the convention to sometimes treat n and c as independent for simplicity.

Upon coarse graining, the surface energy calculation for the so-called amplitude model is essentially unchanged; the only differences being that the density field becomes an *average* density field without atomic-scale fluctuations (that is, $n(\vec{r})$ becomes $n_0(\vec{r})$), and that the free energy becomes a function of the amplitudes A_j, B_l, C_m as well as of the density and concentration fields.

3.5 Numerical Considerations

The angular dependence of the interfacial energy is a small quantity and as such care must be taken to avoid or reduce as many sources of numerical error and fluctuation as possible. This is challenging in that our concern is not just with fluctuations within a given simulation; we also want to ensure that between runs for different angular offsets θ, the other parameters of the model remain constant or fluctuate on a much smaller scale than the changes in interfacial energy.

3.5.1 2D XPFC Simulations

In our investigation we do not want to deal with any interfaces or boundaries aside from the solid-liquid interfaces that we are controlling; that is, away from the interface both in the bulk liquid and in the bulk solid, we want to come as near as possible to simulating an infinite system. The standard procedure in the two-dimensional XPFC case is to implement periodic boundary conditions; that is, one side of the simulation box 'wraps around' to the opposite side, in both the x and y directions (or in x, y, and z for the 3D case). In order to ensure that the wraparound occurs in such a way that there is no partial overlap between or cutoff of lattice points, we choose the number of lattice sites of size a we want to simulate (n_x) and the number of pieces we want each site to be divided into ($1/dx$) and from this calculate the numerical array size

$$N_x = \frac{n_x a}{dx} \tag{3.68}$$

This ensures that an integer number of lattice sites fit into the box, and thus an atom on the far left edge of the box will see the same environment both to its right and to its left.

This procedure is standard, and is fine for the case where there is no rotation of the solid with respect to the interface; that is, when $\theta = 0°$ or $\theta = 90°$. However, for other choices of angle this is no longer sufficient. Consider the following:

Say we measure the size of a lattice site from peak maximum to peak maximum (recall that in the XPFC model our 'atoms' are diffuse structures) and call this the lattice constant a. The method above ensures an integer number of lattice constants will fit in the unrotated simulation box. However, when we rotate the periodic solid with respect to the interface –and therefore also with respect to the x-axis, as our interface is always parallel to this axis – this condition becomes irrelevant. What we are now concerned with is fitting an integer number of "effective lattice constants", which we will call the peak-to-peak distance along the particular angular cut of the lattice. This effective constant may pass through two or more unit cells of the crystal before encountering another peak. However without taking this into consideration, when the simulation box is wrapped around we may encounter a mismatch that can act something like a grain boundary in terms of its impact on the energy of the system. This is especially important to our study in that our calculation of interfacial energy makes the assumption that the *only* contribution to the free energy not from the bulk phases comes from the interface. However, these grain-boundary-like structures introduce new sources of energy to the system, and impact the measured interfacial energy in a variety of ways that are not easily accounted for. The degree to which the energy is changed, and the angles for which there is a major impact, will vary with system size as different sizes will accomodate different effective constants.

It thus becomes necessary to slightly vary the size of our simulation box in order to fit an integer number of effective constants. However, not all angles can be fit in such a way. Mellenthin [26] presents a method to determine permissable angles for the triangular lattice; here we extend the method to the square.

We begin by applying the following rotation to the square basis vectors $\vec{a_1} = a(1,0)$ and $\vec{a_2} = a(0,1)$

$$\begin{aligned} x' &= x\cos\theta - y\sin\theta \\ y' &= y\cos\theta + x\sin\theta \end{aligned} \tag{3.69}$$

which gives the rotated basis vectors

$$\vec{a_1'} = \begin{pmatrix} \cos\theta \\ \sin\theta \end{pmatrix} \tag{3.70}$$

and

$$\vec{a_2'} = \begin{pmatrix} -\sin\theta \\ \cos\theta \end{pmatrix} \tag{3.71}$$

The minimum box size in each direction is given by the conditions [26]:

$$n\vec{a_1'} - m\vec{a_2'} = \begin{pmatrix} L_x \\ 0 \end{pmatrix} \tag{3.72}$$

$$-i\vec{a_1'} + j\vec{a_2'} = \begin{pmatrix} 0 \\ L_y \end{pmatrix} \tag{3.73}$$

where m,n,i, and j are integers. Since we are simulating a strip of solid lying in the x plane, sandwiched between two liquid regions in the y direction, it is only necessary for us to impose condition Eq 3.72. We solve the bottom equation for n and m to get

$$\tan\theta = \frac{m}{n} \tag{3.74}$$

for some integer choices of m, n. Having determined θ, this gives us an effective lattice constant (i.e. the size of the repeated chunk of lattice in the x-direction) of

$$L_x = n\cos\theta + m\sin\theta \tag{3.75}$$

With these values determined we must now choose the size of our simulation array. Some approximations must necessarily be made in the following steps. For the unrotated matrix we chose the number of lattice sites and the number of subdivisions; for each rotated lattice we'd like to stay as close to these values as possible; that is, we aim to keep the actual area of the simulation box roughly the same. To get an estimate of the number of 'effective' unit cells n_x' we should include, we use the following:

$$n_x' = \sqrt{\frac{n_x^2 a^2}{L_x^2}} \tag{3.76}$$

and round to the nearest integer. Thus we ensure that there is not a large change in the simulation area.

There is one final consideration that must be made; namely that we cannot blindly follow Eq 3.68 any more, as with the new n_x' and L_x values replacing n_x and a we typically do not arrive at an integer value. We thus select values of N_x that agree as closely as possible with an integer n_x', while also keeping N_x on a scale that is tenable to simulate in a reasonable period of time. Some examples of the set of values chosen are illustrated in Table 3.1.

Angle	m	n	Nx
0	0	1	1280
4.76364	1	12	1204
9.46232	1	6	1217
15.2551	3	11	1254
18.4349	1	3	1265
21.8014	2	5	1292
26.5651	1	2	1275

TABLE 3.1: A selection of angles and the corresponding array widths used for XPFC simulations.

3.5.2 1D Amplitude Model Simulations

For the 1D effective phase field model we have significantly fewer constraints to worry about than with direct simulation of the microscopic XPFC model. Since we are no longer representing periodic atomic structures, the problem of edge-matching is no longer an issue. Rather than solid sandwiched between regions of liquid and periodic boundary conditions, we now implement a single solid-liquid interface in 1D, where the rotation is handled through the angular dependence of the gradient energy coefficients in Eq 3.45 - 3.52, and zero flux boundary conditions at each edge of the box. That is, for a simulation box with boundaries at *start* and *end*, we create 'ghost' sites on either side of the box intended simply to create the desired environment at the box edges. At each timestep we enforce

```
n[start - 1] == n[start + 1];
n[end +1] == n[end - 1 ];
```

for each field. Not that this is sufficient for the 3-site stencils that we have used to calculate gradient terms; however, as the size of the stencil increases so must the size of the ghost region. For instance, if a 5-site stencil was used, we would now require:

```
n[start - 2] == n[start + 2];
n[start - 1] == n[start + 1];

n[end + 2] == n[end - 2] ;
n[end + 1] == n[end - 1];
```

and so on.

As with the simulations of the microscopic XPFC equations, we also encountered one particular numerical difficulty in the amplitude simulation. The above method requires the use of constant values of the chemical potentials μ_{eq} and μ_a computed from the relevant phase diagram of the alloy system in its relevant thermodynamic variables. Past work done with this model [28] for the binary alloy case where $n = 0$ found no difficulty in stabilizing the solid-liquid interface with constant chemical potential values. However, upon inclusion of the accurate density $n_0(\vec{r})$ profile, we encountered similar difficulties in obtaining a stable interface as those we found for the binary XPFC model. In particular, we found that after some initial adjustment of the interface shape our system melted. Namely, the interface profile, while maintaining the same shape, began to translate laterally through the simulation box, continuing to do so until the system was entirely one phase. As this happened the far field values for all of the fields remained unchanged from their initial values.

We were able to track this issue down to a numerical artefact. For the initial profile, the driving forces (i.e. the right hand sides of Eq 3.53 and 3.54, and the variational derivatives of the amplitude equations) were nonzero around the interface, exhibiting both a positive and a negative spike around this region. As the system evolved and the interface shape cleaned up, these peaks reduced in size significantly and approached zero. However, these peaks do not all succeed in reaching zero, instead maintaining either a small dip or well that stops changing at some finite size. This feature was also observed in the simple binary alloy case; however, it was a small enough value that it did not effect the evolution of the system. In our case, however, this peak is sufficiently large that it evidently drives the system to minimize the energy in the only way that it can: by eliminating the interface. It is likely that this effect is the result of one of the many gradient terms in our expressions, either in concentration or one of the amplitudes. Moving to higher order numerical gradient approximations does not seem to show any improvement, however.

Decreasing both spacial and time steps dx and dt does reduce the size of this persistent peak somewhat, but at a dx of 0.1 and a dt of 0.001 the 'runaway interface' behaviour was still seen. It may be possible to eliminate this behaviour entirely by moving to even smaller dx and dt values; however at some point this becomes unreasonable for the purpose of efficient simulation.

We note that as long as some care is taken in obtaining measurements from the system, this effect is not important. As mentioned, for relatively early times the only changes occuring in the system profile are at the interface, which corrects its shape somewhat. This interface is stable for a brief period of time before it starts to move, and we emphasize

that the movement of the interface is *only* a translation; there is no shifting of the far field values of any of the fields. As such the calculated value of the grand potential rapidly converges after the interface has completed its adjustments and before the system has melted entirely (we note as well that the timescales for the system to completely melt are roughly an order of magnitude higher than those for the interface corrections to occur).

We thus take our systems to be converged when the total grand potential of the system has stopped changing up to 10^{-9}. Visual checks of the data confirm that this is sufficient for the interface shape to have made any changes, and that for longer timesteps no changes to this shape occur.

Chapter 4

Surface Energy Results for Single Component Materials

4.1 XPFC Phase Diagram

In this section we consider a two-dimensional pure material that can stabilize square or triangular crystal structures. To construct the phase diagram of the corresponding XPFC construction for this system, we need to obtain free energies for all the possible competing phases. We begin with the mode approximations for the densities of the solid phases. Following the form of Eq 2.12, we take a single-mode approximation for the triangular phase, and a two-mode approximation for the square phase. Simplifying we get the following approximations:

$$n_{sq}(x,y) = n_0 + 2A\left[\cos\left(\frac{2\pi}{a}x\right) + \cos\left(\frac{2\pi}{a}y\right)\right] + 2B\left[\cos\left(\frac{2\pi}{a}(x+y)\right) + \cos\left(\frac{2\pi}{a}(x-y)\right)\right] \tag{4.1}$$

$$n_{tri}(x,y) = n_0 + 2C\left[\cos\left(\frac{\sqrt{3}\pi}{a}y\right) + \cos\left(\frac{\pi}{2a}(3x+\sqrt{3}y)\right) + \cos\left(\frac{\pi}{2a}(3x-\sqrt{3}y)\right)\right] \tag{4.2}$$

where n_0 is the mean density in the solid and A, B, and C are mode amplitudes. As previously we set the lattice spacing $a = 1$.

We then substitute each of these mode approximations into the form of the free energy functional from Eq 2.21 and integrate over the respective crystal unit cells to obtain

square and triangular free energies. For the purposes of the phase diagram it is sufficient to take the sum of the correlation peaks rather than the envelope. The integral over the convolution term yields a Dirac delta function in k-space and as such simply returns a sum of terms in which each respective mode is multiplied by the correlation function evaluated at that mode.

We are left with equations for the free energy of the bulk square and triangle phases in terms of the average density and the mode amplitudes.

$$\begin{aligned} F_{sq} = 2(A^2+B^2)(1-n_0\eta+n_0^2\chi) + 3\chi^2(A^4+B^4) + 4A^2B(2n_0\chi-\eta+3B\chi) \\ +\frac{n_0^2}{2} - \eta\frac{n_0^3}{6} + \chi\frac{n_0^4}{12} - 2A^2\hat{C}_{k10}(k=k_{10}) - 2B^2\hat{C}_{k11}(k=k_{11}) \end{aligned} \tag{4.3}$$

$$\begin{aligned} F_{tri} = 3C^2(1-n_0\eta+n_0^2\chi) + 2C^3(2n_0\chi-\eta) + 15C^4\frac{\chi}{2} \\ +\frac{n_0^2}{2} - \eta\frac{n_0^3}{6} + \chi\frac{n_0^4}{12} - 3C^2\hat{C}_{k10}(k=k_{10}) \end{aligned} \tag{4.4}$$

These expressions are then minimized with respect to the amplitudes A, B, and C. For mathematical simplicity (only in calculating the phase diagram) we make the assumption that for the square, $B = fA$ and take the computed value of $f = 0.605$ from past XPFC studies [24]. We thus minimize to solve for one amplitude for each phase.

We can additionally construct a liquid phase free energy from either of these expressions by considering the case where all mode amplitudes are zero. The resulting free energy curves are plotted for a chosen temperature (Fig 4.1) and compared. A Maxwell equal area construction is then performed between each pair of curves to determine coexistence regions and thereby the liquidus and solidus lines. The resulting phase diagram is shown in Fig 4.2.

It should be noted that these calculated phase diagrams are necessarily approximate, and may not agree exactly with equilibrium results from the XPFC simulations; however, this method is sufficient to give a reliable starting point for initialization of the system (i.e. the boundary conditions of the fields in the Euler-Lagrange equations).

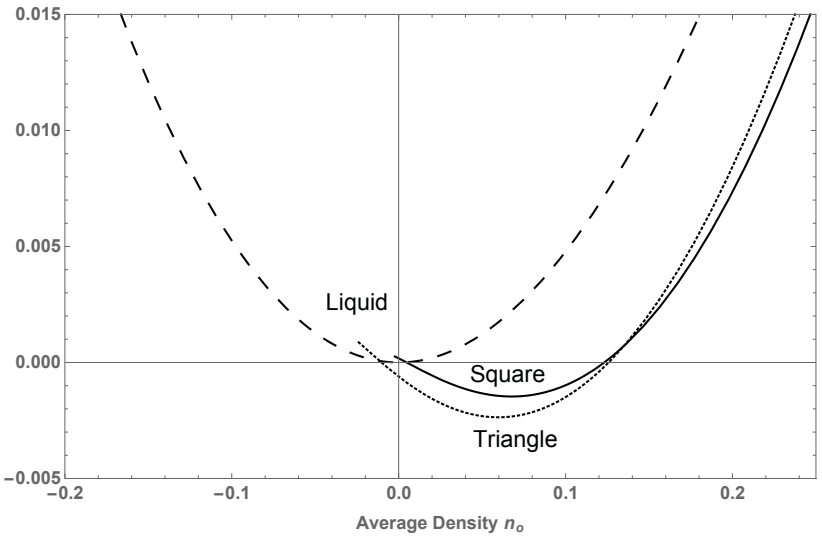

FIGURE 4.1: Calculated free energy curves for the square, triangle, and liquid phases of a single-component XPFC material, at a model temperature of $\sigma = 0.10$.

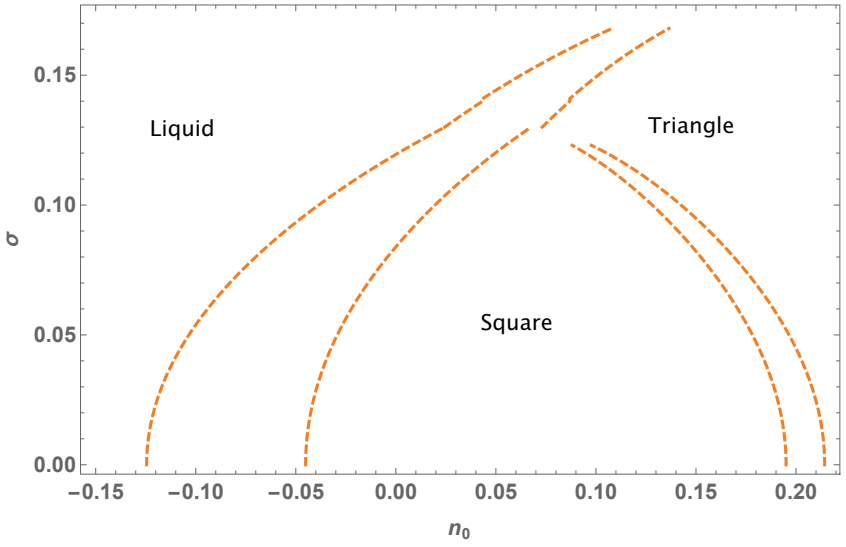

FIGURE 4.2: Phase diagram for a two-dimensional pure XPFC material capable of stabilizing both square and triangular crystal structures. Phase diagram is in terms of average density n_0 and model temperature σ. A peritectic temperature between square, triangle and liquid can be obtained with higher order density expansion around $n_0 = 0.075$[23].

4.2 Results of Surface Energy Calculations

For the pure material we performed trials for a variety of angles between 0 and $\frac{\pi}{2}$ (Fig 4.3), in which we solved Eq 3.11 and 3.12. We confirm that for each angle trial the average density n_0 is constant on the order of the change in γ, with fluctuations in density occuring only on order 10^{-6}. For each n_0 the chemical potential μ converges quickly to a single value (Fig 4.4) with fluctuations between trials of order 10^{-5}.

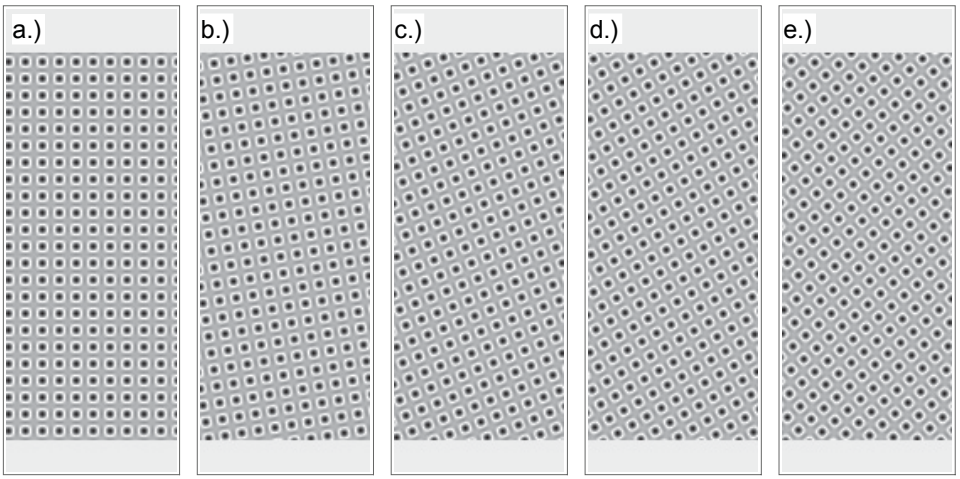

FIGURE 4.3: Density plots of the initialized solid strips embedded within liquid, at angles of a.) 0°, b.) 9°, c.) 21°, d.) 30°, and e.) 40°. The 2D simulation has been initialized with a sharp interface; however, this becomes more diffuse over the course of the simulation.

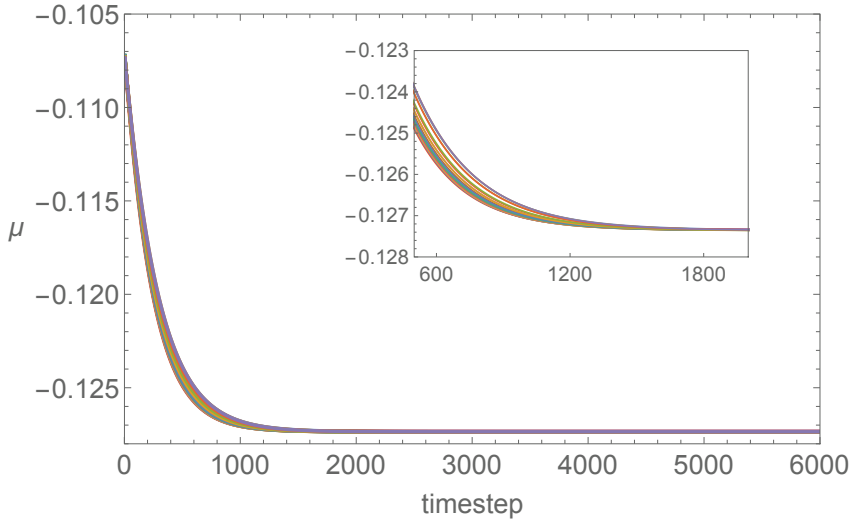

FIGURE 4.4: Convergence of chemical potential μ values with time step for all angles tested. Inset shows rapid convergence for early timescales.

We can predict the approximate form of the interfacial energy curve by making the assumption that the primary mechanism affecting the energy is the number of broken bonds per unit length of the solid-liquid interface. It is easy to picture that, for a square crystal, at 0 or $\frac{\pi}{2}$ there will be less broken bonds at the interface than at $\frac{\pi}{4}$; this idea is illustrated in Fig 4.5, as is the resulting approximate free energy curve.

We see no change in the interfacial energy data with average concentration, as is expected for a single-component material. We see a small change in anisotropy, on the order of 1%, with a temperature increase of 0.02 in terms of model parameters (Fig 4.6, left panel). The curves are fitted with the third order form of Eq 2.1. The data follows the form

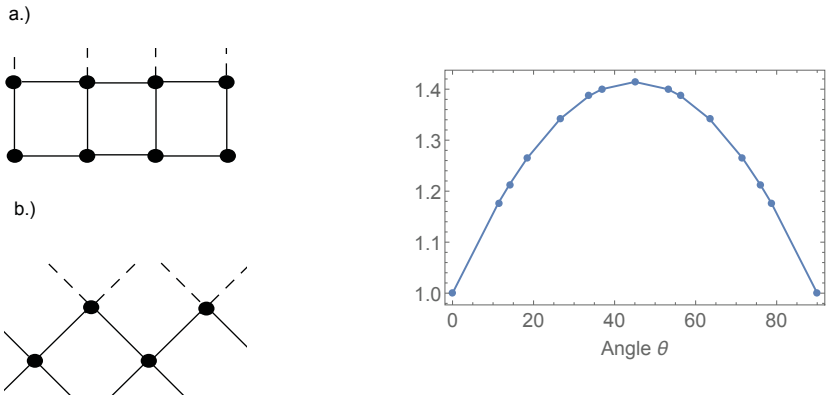

FIGURE 4.5: On the left we present representations of the solid-liquid interface for a crystal oriented at a.) 0° and b.) 45°. Dashed lines represent broken bonds. The right-hand plot illustrates the approximate shape of the free energy curve by plotting the number of broken bonds per unit length versus angle.

predicted from the broken bonds approximation. The isotropic fitting parameter γ_0 and the anisotropies ϵ_i are shown in Table 4.1.

σ	γ_o	ϵ_4	ϵ_8	ϵ_{12}
0.05	0.284454	-0.023609	-0.001932	-0.000282
0.07	0.253944	-0.025088	-0.001984	-0.000301

TABLE 4.1: Fitting parameters for pure material interfacial energy curves.

Finally, we take the second derivative of the interfacial energy fits to obtain stiffness $S(\theta) = \gamma + \gamma''$. As with $\gamma(\theta)$ itself we see only a small change with either temperature or average concentration. The resulting curve is also shown in Fig 4.6 (right panel).

Both surface energy and stiffness of a pure XPFC material follow the expected form. A maximum of interfacial energy corresponds to a minimal stiffness point in the interface. We note one interesting result however; our work here has been done with a single-component material that can stabilize both square and triangular crystals. When compared to past work[29] for a single-component material that stabilized only the triangle phase, we find that our curves for both $\gamma(\theta)$ and $S(\theta)$ are significantly broader in comparison. We attribute this, and the necessity of our use of a higher order fit, to the effect of the second crystal symmetry influencing the correlation function. The details of the curve fitting are discussed in further detail in Chapter 6, when we address alloys.

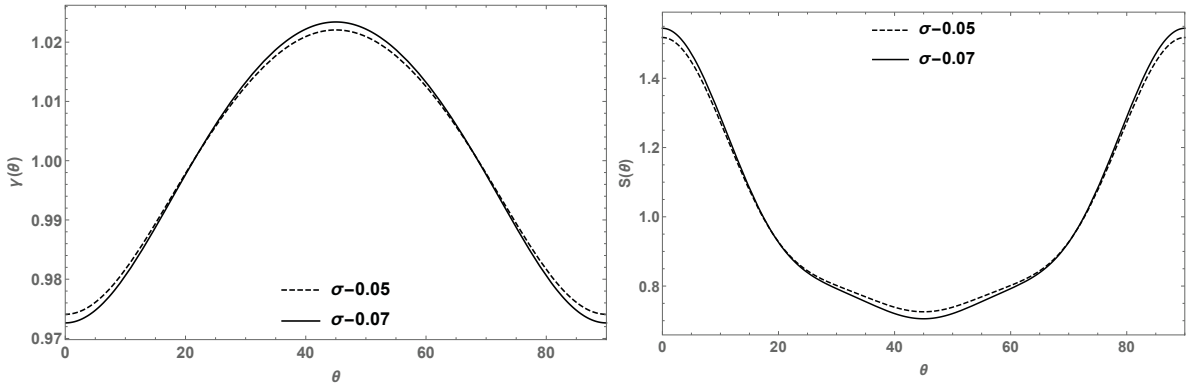

FIGURE 4.6: Normalized interfacial energy (left) and stiffness (right) plots for two temperatures; note that changes in these curves are minimal. Both $\gamma(\theta)$ and $S(\theta)$ follow the general trend of the expected behaviour for a pure material; however the curves are not as sharp as in the case where the single-component material can stabilize only a single crystal symmetry.

Chapter 5

Thermodynamics of an XPFC Binary Alloy in Concentration, Density, Pressure, and Temperature Space

5.1 Phase Diagram Construction

The binary alloy phase diagram follows the same basic high level prescription as a pure material, in terms of inserting the respective density mode approximations into the free energy functional and integrating over the unit cell to arrive at a mean field free energy density of solid phases. However when it comes to determining regions of coexistence, we now have an expression in terms of both average density n_0 and average concentration c_0 at a single temperature; we've effectively added another dimension to our phase diagram. Moreover, since density is a conjugate variable to pressure, control of the density axis implies control of pressure. To our knowledge there has been no previous PFC or related phase field study that examines the full c - n_0 - T space for metallic alloys.

The detailed construction of the full binary phase diagram is somewhat complex. Past work with alloys ([24],[28]) has typically been done around a density $n_0 = 0$ in the mode approximation inserted into the free energy. This leads to an effective two-dimensional phase diagram in temperature and concentration, shown in Fig 5.1.

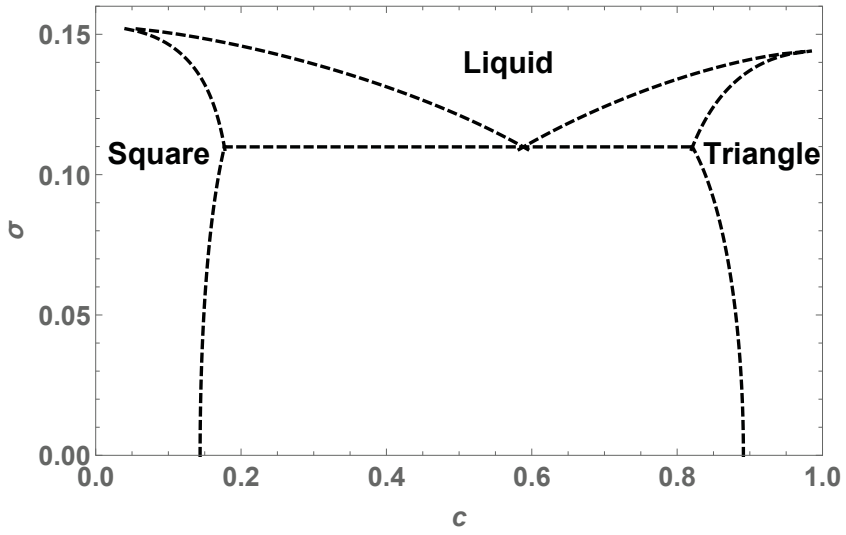

FIGURE 5.1: Simplified binary alloy phase diagram in concentration and temperature, calculated with the density field $n0$ set to zero. The concentration axis represents the fraction of species B present. The eutectic point occurs at a model temperature of $\sigma = 0.10$.

We aim in this thesis to construct a comprehensive phase diagram for a binary alloy by retaining both density and concentration as values that can be varied; this necessitates a 3-dimensional phase diagram construction. In addition we find that for a given constant temperature σ, a variety of sets of far-field values n_S, n_L, c_S, c_L can be found, each existing at a different pressure p. We are thus able to map out the phase diagram in pressure space as well.

Constructing a phase diagram in these variables will be necessary for setting the far-field values of the amplitude equations in concentration, density and order parameter amplitudes discussed above. To solve for the required far field (i.e equilibrium) values in both density and concentration, we require a set of 4 independent equations. We begin with the coarse grained expressions for the chemical potentials μ_{eq} and μ_A (Eq 3.31 and 3.33, respectively) presented in Chapter 3 and evaluated in each bulk phase:

$$\mu_{eq} = \frac{1}{n_S + 1}\frac{\partial F_S}{\partial c_S} = \frac{1}{n_L + 1}\frac{\partial F_L}{\partial c_L} \tag{5.1}$$

$$\mu_A = \frac{\partial F_S}{\partial n_S} - \frac{c_S}{n_S + 1}\frac{\partial F_S}{\partial c_S} = \frac{\partial F_L}{\partial n_L} - \frac{c_S}{n_L + 1}\frac{\partial F_L}{\partial c_L} \tag{5.2}$$

Where F_S and F_L are the coarse grained bulk free energies of the solid and liquid phases, respectively. Additionally, we write the equation for pressure (recalling that $p = -\Omega$ and

substitute the forms for μ_{eq} and μ_a above into Eq 3.64):

$$p = (n_S + 1)\frac{\partial F_S}{\partial n_S} - F_S = (n_L + 1)\frac{\partial F_L}{\partial n_L} - F_L \tag{5.3}$$

We then specify a temperature σ and pressure p, and using the expressions above solve the set of equilibrium equations [30]:

$$\mu_{eq}^L(\sigma, n_L, c_L) = \mu_{eq}^S(\sigma, n_S, c_S) \tag{5.4}$$
$$\mu_a^L(\sigma, n_L, c_L) = \mu_a^S(\sigma, n_S, c_S) \tag{5.5}$$
$$p^L(\sigma, n_L, c_L) = p \tag{5.6}$$
$$p^S(\sigma, n_S, c_S) = p \tag{5.7}$$

for n_S, n_L, c_S, c_L. In addition, the equilibrium chemical potentials and the solid amplitudes to be put into the simulation can be calculated from these far-field values. It is recalled that amplitudes are eliminated as previously by minimizing the respective free energies; note however that to obtain sufficiently accurate amplitude values for the simulation, all amplitudes must be solved for independently. The ratio approximation discussed in section 4.1 is insufficient for this method.

Note that not every combination of average values n_0, c_0 is possible at any given pressure. For a given choice of c_0 it is necessary to equate the respective lever rules in density and concentration to solve for n_0.

$$\frac{c_0 - c_L}{c_S - c_L} = \frac{n_0 - n_L}{n_S - n_L} \tag{5.8}$$

Alternately, if a particular c_0, n_0 combination is desired, one can choose not to specify pressure, and instead to solve

$$\mu_{eq}^L(\sigma, n_L, c_L) = \mu_{eq}^S(\sigma, n_S, c_S) \tag{5.9}$$
$$\mu_a^L(\sigma, n_L, c_L) = \mu_a^S(\sigma, n_S, c_S) \tag{5.10}$$
$$p^L(\sigma, n_L, c_L) = p^S(\sigma, n_S, c_S) \tag{5.11}$$
$$\frac{c_0 - c_L}{c_S - c_L} = \frac{n_0 - n_L}{n_S - n_L} \tag{5.12}$$

for given coexistence values and temperature. The latter value is not ideal for constructing a full phase diagram however, since there is no control over the pressure at which the resulting solution exists.

We present the phase diagram calculation for a square-triangle binary alloy with equal stiffness in both species, that is, $\alpha_{10}^A = \alpha_{10}^B = 1.5$. The stiffness for the second length scale of the square is chosen as $\alpha_{11}^A = \sqrt{2}\alpha_{10}^A$, in order to preserve elastic isotropy within the square phase. The simplified phase diagram for an analagous system constructed in 2 dimensions around $n_0 = 0$, is shown in Fig 5.1 for comparison.

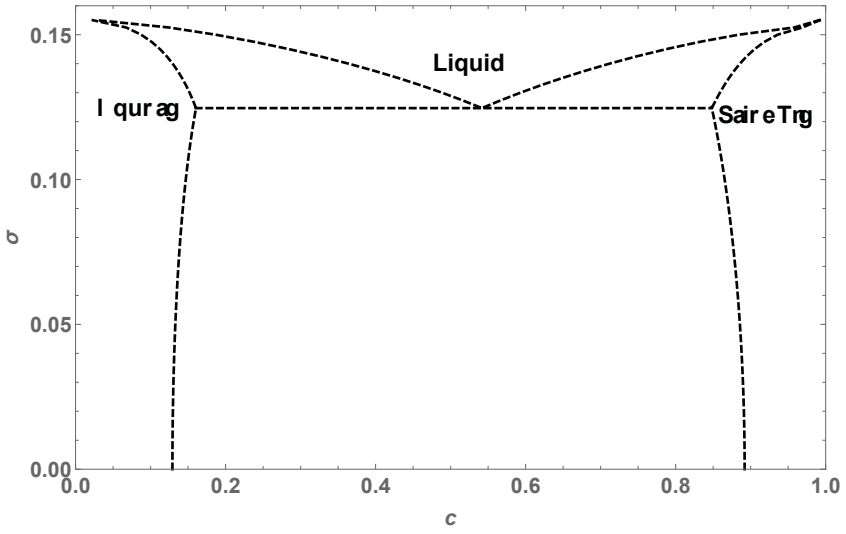

FIGURE 5.2: c - σ projection of a c-n_0-σ phase diagram for a binary alloy in the case of constant pressure. The same general shape as in the simplified $n_0 = 0$ case (Fig 5.1) is maintained. The phase diagram was constructed at a constant model pressure of $p = -0.07$. Note that at this pressure the eutectic temperature has risen to about $\sigma = 0.125$.

For the purposes of our numerical experiments, and indeed for most practical purposes, a constant-pressure phase diagram is preferred. We present by way of analogy, a 2D projection of the temperature-density-concentration phase diagram onto the temperature-concentration axes (Fig 5.2); here we can see that the general shape of the phase diagram closely mirrors the zero-density version, but with a small shift in the eutectic that was not adequately captured in the simplified $n_0 = 0$ approximation.

Fig 5.3 shows a three-dimensional phase diagram for a constant pressure of $p = -0.07$. The planar surfaces represent the solid-liquid coexistence regions for the square and triangle, respectively. The area above these curves corresponds to the liquid region of the phase diagram, and below to the solid region. The small n_0 and large n_0 edges of these planes are the respective solidus and liquidus lines, while points anywhere along the surface represent average values c_0, n_0, that can yield coexisting phases. The curve along which the two planes intersect represents the 2D analog of the eutectic point; a 'eutectic line'.

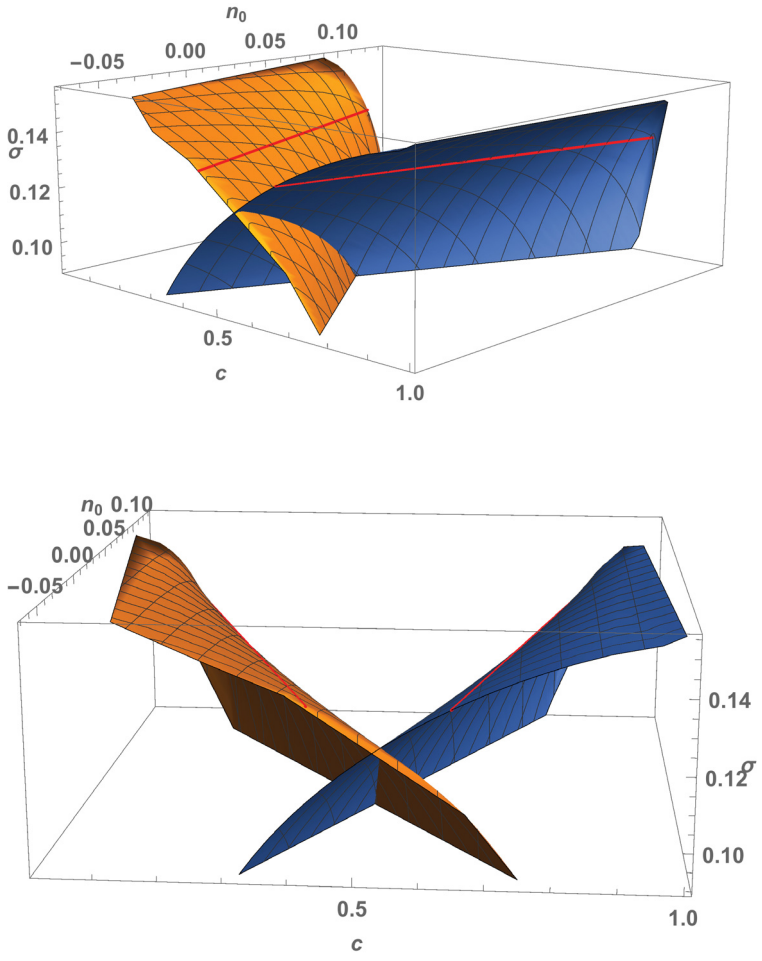

FIGURE 5.3: Solid-liquid coexistence regions of the 3D binary alloy phase diagram in temperature σ, concentration c_0, and density n_0, at a constant pressure $p = -0.07$. The orange represents the square-liquid coexistence plane, while the blue is the triangle-liquid. Red lines indicate coexistence tie lines.The intersecting eutectic line can be clearly seen; note that the eutectic temperature changes as one moves through density space.

5.1.1 Pressure Space Phase Diagram

We additionally present the behaviour of the phase diagram in pressure space. It is interesting to note that as we vary pressure for a constant temperature of $\sigma = 0.12$, the overall phase diagram maintains the same major features as the more typical constant pressure representation.

Fig 5.4 shows a pressure-concentration phase diagram of a binary alloy at constant temperature, projected from a concentration-density-pressure phase diagram. As model pressure becomes increasingly negative, the behaviour of the phase diagram mimics that

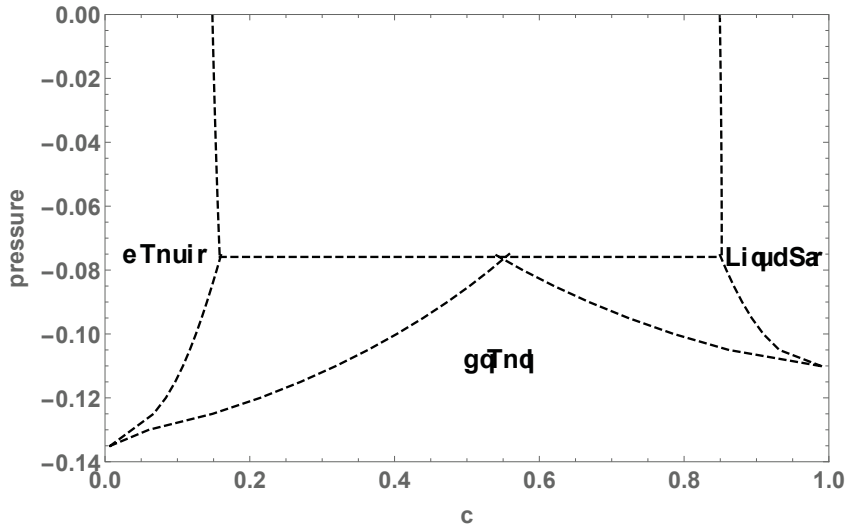

FIGURE 5.4: *c*-*p* phase diagram for a binary alloy projected from a three-dimensional *c*-*p*-n_0 phase diagram for the case of constant model temperature $\sigma = 0.12$. We see an inversion of the typical temperature-concentration phase diagram, with what may be termed a 'eutectic pressure' at $p = -0.75$.

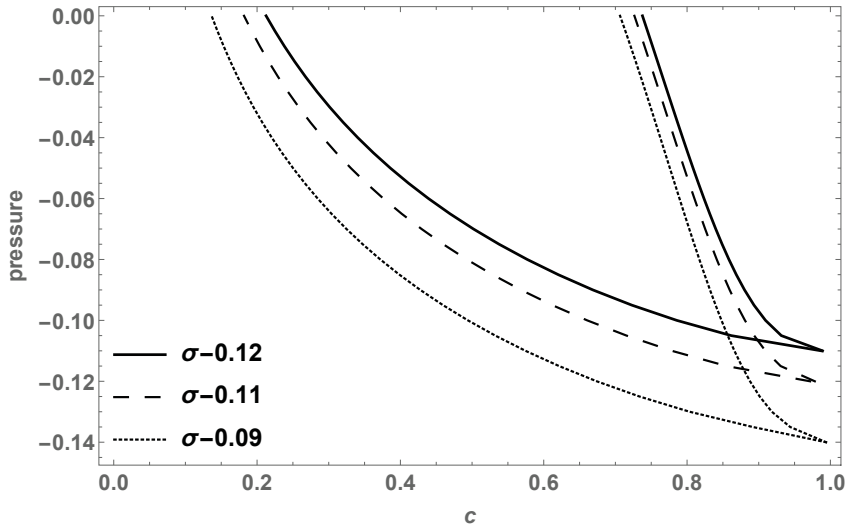

FIGURE 5.5: Pressure-concentration curves plotted for a variety of temperatures, for the triangle-liquid coexistence region of the phase diagram. This type of plot is more common when pressure is varied. Note that both the position and the width of the resulting coexistence region changes with temperature.

seen for constant pressure as temperature increases. Note in particular that the respective sizes of the square and triangle solid-liquid coexistence regions are comparable to those seen in the constant pressure case. We can also draw a parallel to the eutectic temperature and note the presence of a 'eutectic pressure' for the constant temperature case, located at roughly $p = -0.75$.

Rather than presenting a full 3D concentration-pressure-temperature phase diagram,

which can be awkward to visualize, in Fig 5.5 we present explicit pressure-concentration cuts of the triangle-liquid coexistence region, measured at a variety of temperatures. This clearly shows the manner in which both the shape and position of the major features of the liquidus and solidus lines vary with temperature.

The pressure dependence of the binary alloy phase diagram is clearly quite significant, and may strongly impact the potential of a simulation to stabilize certain structures and/or coexistence regions. Care must therefore be taken, especially if one desires to compare simulation results to experimental work, to ensure that trial profiles conform to a constant pressure. As we have demonstrated, when pressure is not specified in the construction of the phase diagram itself, a variety of different pressures may be inadvertently represented for each set of equilibrium solutions.

Chapter 6

Binary Alloy Surface Anisotropy

We investigate the impact of species concentration on the surface anisotropy of a binary alloy via a 1D amplitude expansion simulation, derived via coarse-graining of the binary XPFC model as presented in Section 3.3.

In order to investigate the effect of concentration c_0 on interfacial anisotropy, we alter the parameters of our generating XPFC model to emulate a phase diagram more in line with those of the aluminum-zinc alloys (see Fig 6.2) in which such concentration dependence has been observed experimentally [1]. Namely, we require a case where one component element has significantly higher stiffness than the other, resulting in a highly asymmetrical phase diagram. Using the standard procedure described in Chapter 5 for constructing alloy phase diagrams we obtain the phase diagram in Fig 6.1, which represents the alloy system we will be studying in the latter half of this chapter.

To begin with, however, we test our method for calculating interfacial energy on the more symmetrical phase diagram obtained in Chapter 5 to ensure that we can reproduce past results for a similar system.

6.1 Fitting Interfacial Energy curves

We digress briefly to discuss Eq 2.1 used to fit the interfacial energy data from our simulation of the symmetric binary alloy in Chapter 5. The first image in Fig 6.3 shows a sample of the raw data obtained from equilibrating the concentration, amplitude, and density profiles (hereafter just a *profile*) repeatedly for a range of interface orientations from $\theta = 0°$ to $\theta = 90°$. A clear sinusoidal form can already be observed.

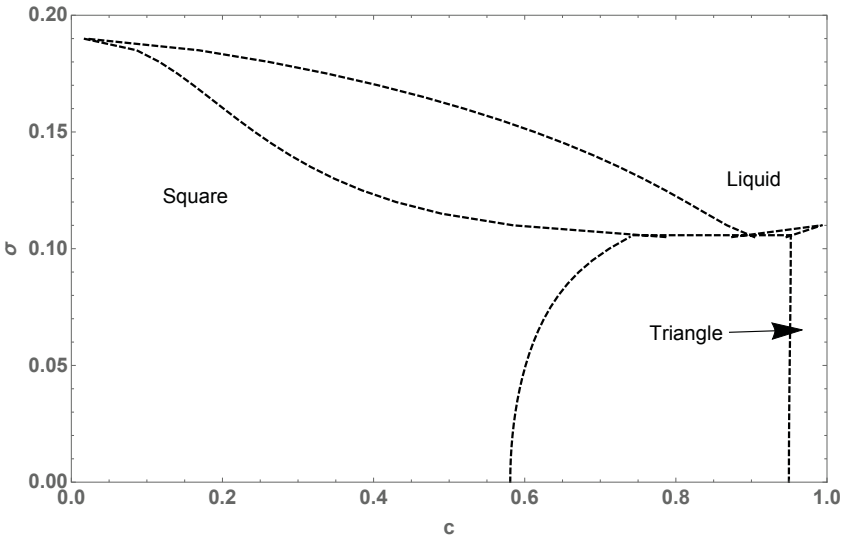

FIGURE 6.1: Solid-liquid coexistence region of the theoretical phase diagram obtained from the choice of parameters in Table 6.2, in which the left-side (square) species strongly dominates. This was constructed at a constant pressure of $p = -0.07$.

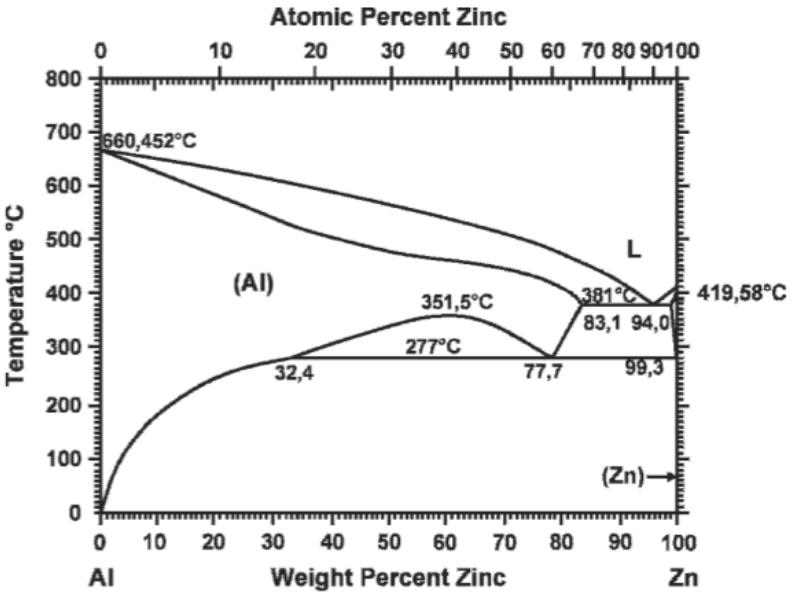

FIGURE 6.2: Aluminum Zinc phase diagram reproduced with permission from [1].

In fitting this curve, the expansion in Eq 2.1 can be taken to any desired order, where contributions from successive orders yield smaller and smaller corrections to the form. We aim to choose the smallest order expansion that can accurately capture the behaviour of the stiffness $S = \gamma + \gamma$". Past work with the same simulation method [28] has found a first order fit to be sufficient. However, we note that such trials were done for pure materials and alloys with symmetrical phase diagrams; that is, alloys where both species have the same preferred crystal structure (either both square or both triangle, for instance). In

either of these cases there is no competition from a different crystal structure and thus it is reasonable to expect that a simple first-order fit will be sufficient to capture the behaviour.

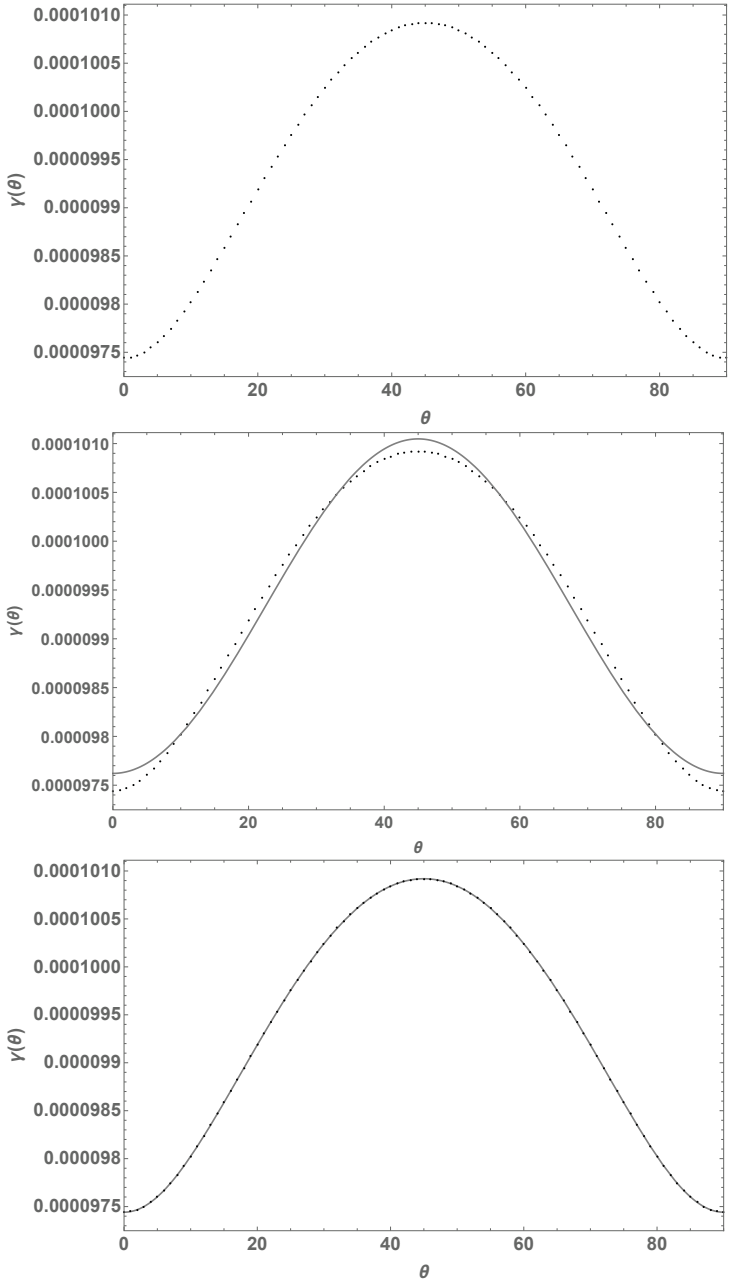

FIGURE 6.3: Top panel: simulation data for the interfacial energy $\gamma(\theta)$ at temperature $\sigma = 0.12$ and average concentration $c_0 = 0.2$ for the symmetric alloy in Fig 5.2 at a model pressure of $p = -0.07$. Middle panel: the notably poor first-order fit to the data; Bottom panel: the sixth-order fit to the data. A clear improvement in fit is visible.

In our case, however, the influence of the triangle species on the interfacial energy in the square phase is quite pronounced. Taking only the first order expansion results in an obviously poor fit to the data (middle image of Fig 6.3) and so we consider higher

order terms. Here we must be careful, as we obtain stiffness results by taking the second derivative of the fit to γ. As discussed previously, anisotropies in γ are exaggerated in S, and we must take care that artificial angular dependences introduced by an imperfect fit to the data in γ are not taken as significant results in stiffness. We find in particular that a second order fit introduces an artificial local maximum in stiffness at the location of the global minimum for higher order fits. We continue taking successively higher order fits until we are satisfied that no significant changes in the resulting stiffness curves are present (Fig 6.4). We thus present stiffness curves obtained by a sixth order fit to the interfacial energy data, that is:

$$\gamma = \gamma_o \left[1 + \epsilon_4 \cos 4\theta + \epsilon_8 \cos 8\theta + \epsilon_{12} \cos 12\theta + \epsilon_{16} \cos 16\theta + \epsilon_{20} \cos 20\theta + \epsilon_{24} \cos 24\theta\right] \tag{6.1}$$

Such a high order expression may not be reasonable or desirable for some applications of this data, however. We therefore note that several major features of the stiffness anisotropy curve are still obtained by the first order fit: that is, the same number of maxima and minima exist, at the same angles. Additionally, we note that moving from first to sixth order, the values of the lowest order fitting parameters γ and ϵ_4 only differ by 0.002% and 0.2% respectively, and that each successive fitting parameter ϵ_i is approximately an order of magnitude smaller than the one previous. As such for practical purposes (such as determining dendrite orientation), the first order fit contains the relevent data needed to extract important information about dendritic growth directions. By the same token, for regions where a double local minima may exist in the stiffness (as seen in Rappaz' results for a composition of 0.58)[1], the third-order fit should be sufficient in maintaining an accurate global minimum while also sustaining the presence of multiple local wells or peaks. These features are illustrated in Fig 6.4.

6.2 Species of Comparable Stiffness

Considering solid-liquid interfaces in the square-liquid coexistence region of the more symmetrical phase diagram, we begin by performing trials at a constant temperature σ and a variety of average concentration values c_0 within the solid-liquid coexistence region. Note that for this simulation, keeping the temperature constant amounts to staying on the same phase coexistence tie line, with the same far field values in concentration and density, and as such we do not expect to see any difference in the resulting interfacial energies. We can see from Fig 6.5 that this is the case, and the values of the various

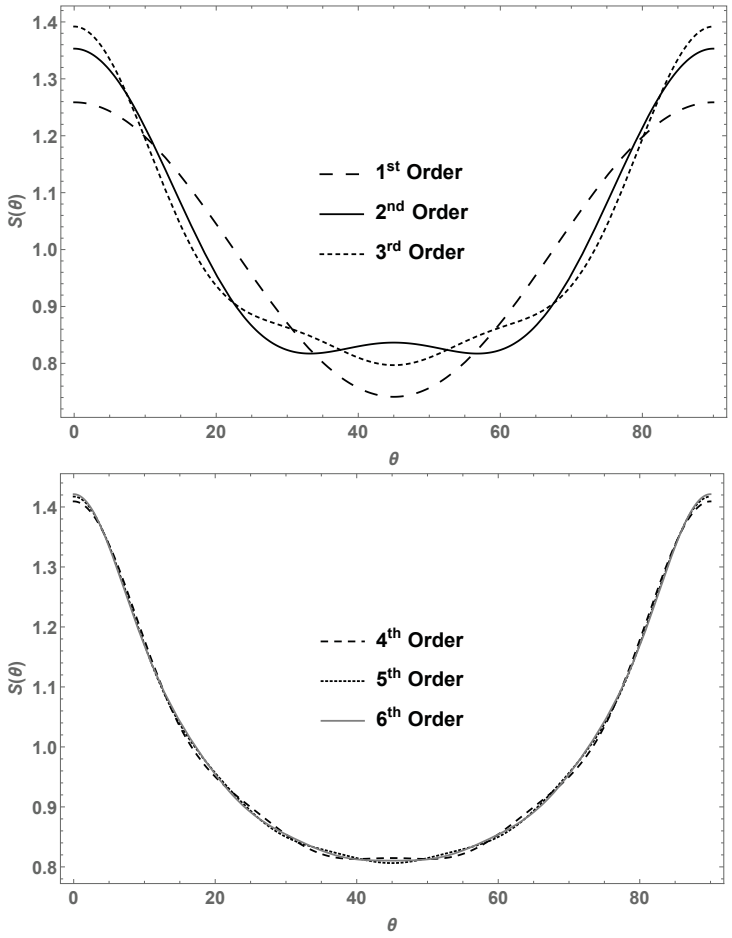

FIGURE 6.4: Stiffness curves $S(\theta)/\gamma_o$ resulting from first through sixth order fits. The second order fit in particular is misleading as it destroys the global minimum. Note that from fourth to sixth order there are minimal changes in the fit, and as well that for a stiffness with a single minimum the first order maintains the appropriate features, while for a stiffness with multiple minima, the third order fit is expected to be sufficient.

fitting parameters $\{\gamma, \epsilon_i\}$ for the curves corresponding to different c_0 remain unchanged. In all cases pressure remains fixed at $p = -0.07$.

σ	c_S	c_L	n_S	n_L
0.12	0.166754	0.582612	0.094614	-0.069095
0.13	0.151997	0.488390	0.092782	-0.069095
0.14	0.129449	0.364015	0.090405	-0.069095

TABLE 6.1: Far field values of density and concentration for a variety of temperatures, used to initialize simulation profiles in these fields. The subscripts S/L denote solid and liquid, respectively.

We next scan over a variety of temperatures; each temperature chosen gives a different set of far field values for phase concentration and density (shown in Table 6.1). The normalized interfacial energies and stiffnesses are presented in Fig 6.6. We see a clear change in the amplitudes of these curves with temperature. We additionally present plots

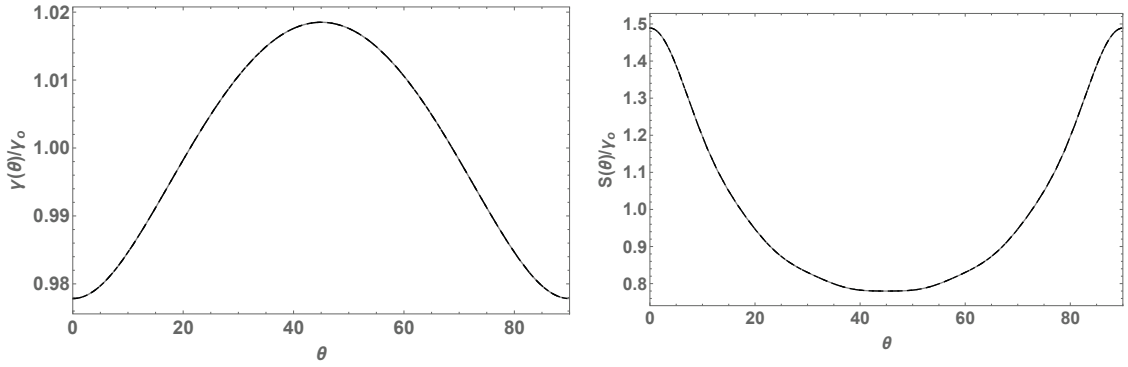

FIGURE 6.5: Interfacial energies γ and stiffnesses S overlaid for average concentrations of $c_0 = 0.2$, 0.3, and 0.4, at a constant temperature $\sigma = 0.13$. It is clear that there is no appreciable change in the behaviour of either of these quantities with average concentration when changing along a fixed-temperature tie line.

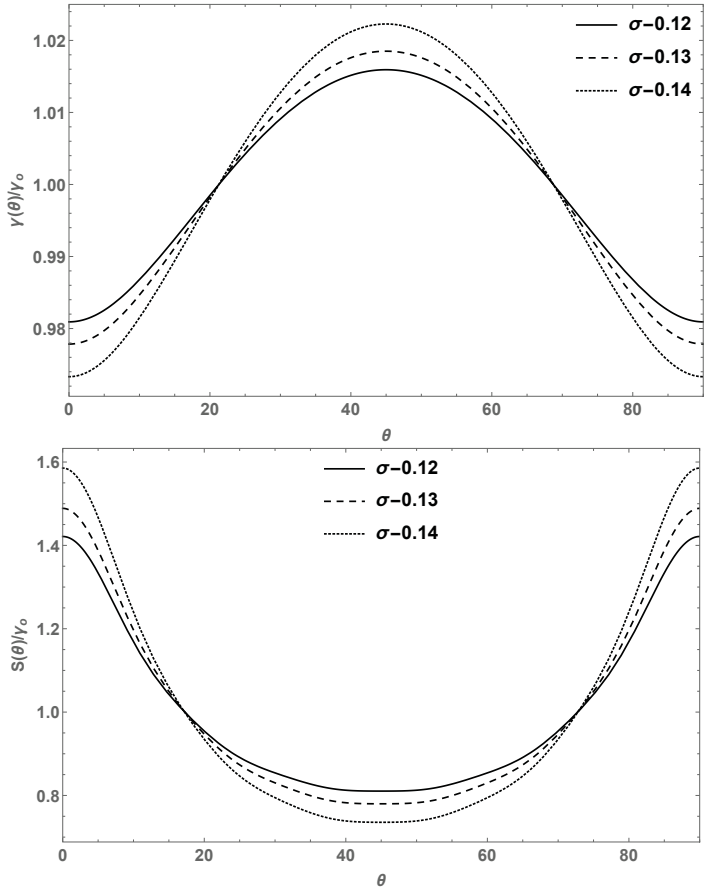

FIGURE 6.6: Interfacial energies γ and stiffnesses S normalized by the constant γ_o, shown for a constant average concentration $c_0 = 0.2$ and a variety of temperatures. The overall shape of the curves shown stays the same; however a change in the heights of the respective maxima and minima are clearly visible.

of the isotropic and anisotropic parameters in terms of temperature (Fig 6.7). We confirm that both γ and ϵ_4 decrease as temperature increases, as was observed in previous 1D amplitude simulations for an alloy system with $n_0 = 0$ [28]. Higher order anisotropy

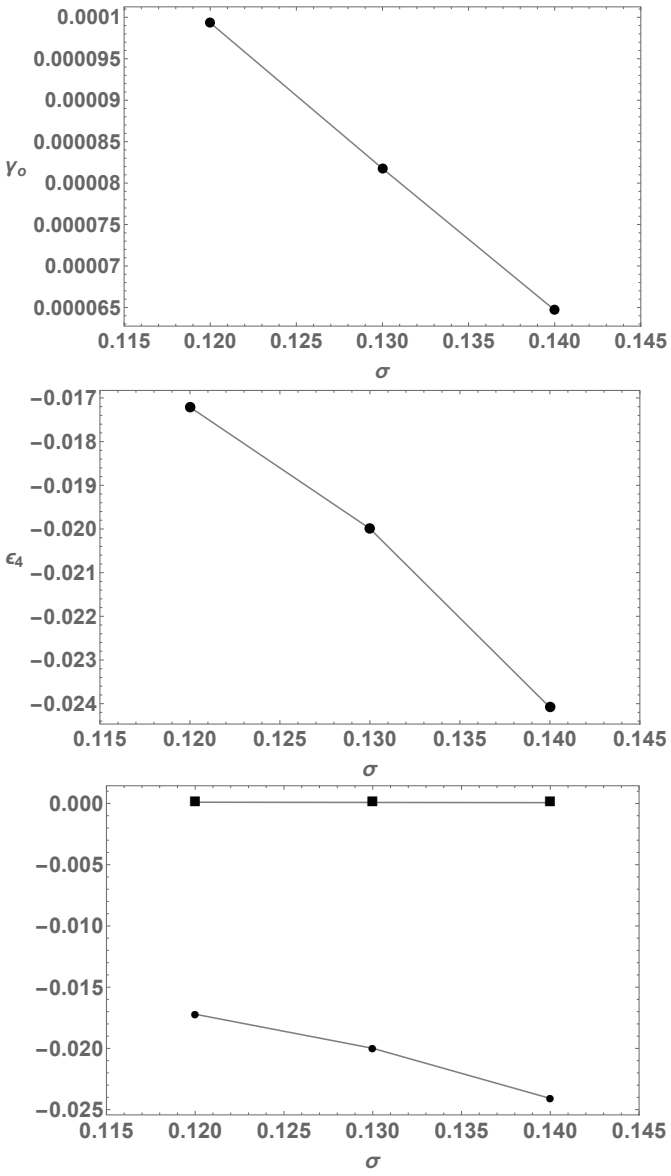

FIGURE 6.7: The behaviour of the isotropic fitting parameter γ_o (top) and the highest order anisotropic parameter ϵ_4 (middle) are shown. Both decrease with increasing temperature. Note from the bottom panel that the change in γ_o (square) values is not significant on the order of the ϵ_4 (circles).

parameters follow the same trend, albeit with shallower slopes. In addition note that the leading order anisotropy values ϵ_4 are several orders of magnitude larger than the γ_o.

6.3 Asymmetrical Alloy

We do not have sufficient degrees of freedom in our theoretical phase diagram construction to exactly recreate the aluminum-zinc phase diagram (Fig 6.2) used by Rappaz et

al. We satisfy ourselves with a phase diagram for which the solid-liquid coexistence region for species A extends significantly past a 50% concentration of species B. This is crucial since we measure the anisotropy by making use of the solid-liquid interface, and as such require an alloy system for which solid and liquid can coexist over a wide range of concentrations.

We primarily alter the phase diagram by changing the α_j values, which determine the widths of the Gaussian peaks in the correlation function, and thus control the relative stiffness of the component pure materials that comprise the alloy. In addition, we adopt the convention described in Greenwood et al [24], where the Debye Waller prefactor to the Gaussian is rewritten as

$$e^{-\frac{\sigma^2 \vec{k}_j^2}{2\rho_j \beta_j}} = e^{-\frac{\sigma^2}{\sigma_{Mj}^2}} \tag{6.2}$$

where σ_{Mj}^2 is an effective transition temperature that can be tuned to obtain desired behaviour. We can thus manipulate both peak heights and widths via the α_j and σ_{Mj} for each correlation peak. We however still choose the α for the square correlation function to satisfy the ratio for isotropic elasticity within the square crystal (Table 6.2).

We make an initial selection of parameters such that we can access both a wide range of concentrations overall, and several concentrations at any given temperature. In order to satisfy this range of coexistence requirements, we produce a somewhat eccentric phase diagram that is heavily dominated by the square phase. In particular the solid-solid region of the phase diagram (i.e. the region below the eutectic) is somewhat irregular. However, we consider the resulting calculated phase diagram adequate to illustrate both the capabilities of the model and the dependence of the interfacial anisotropy on the various model parameters. The resulting diagram also sufficiently mimics the one used in the main experimental study on this topic by Rappaz et al[1] in the solid-liquid coexistence region. The phase diagram obtained from these choices of parameters is shown in Fig 6.1.

$\vec{k}_j$	α_j	σ_{Mj}
$\vec{k}_{10}^A$	1	$\frac{\pi^2}{3}$
$\vec{k}_{11}^A$	$\sqrt{2}$	$\frac{2\pi^2}{3}$
$\vec{k}_{10}^B$	3.5	$\frac{8\pi^2}{9}$

TABLE 6.2: Choice of correlation function widths and heights (α and σ_M respectively) to create the square-biased binary alloy phase diagram in Fig 6.1.

As previously we consider a variety of concentrations at a constant temperature. Once again when confined to a single tie line we observe no change in the interfacial energy or

the resulting stiffness. We thus vary the temperature for a constant concentration and once again see different amplitudes for the interfacial energy and stiffness curves. We discuss our results further in the following section.

6.3.1 Following the solidus curve

We pause in our analysis to consider carefully what is being measured in the experimental results obtained from studies of Al Zn alloys[1][3]. These works were able to observe a concentration dependence in dendrite orientation and provided strong motivation for performing this study. These experimental works observed a change in stiffness anisotropy of Al Zn alloy with percentage zinc composition by measuring the dendrite orientation in the final solidified sample. Samples were solidified gradually via directional solidification, and results were presented both in terms of average composition and of nominal composition of the solid phase. We note that for a sufficiently steady cooling rate, this solid composition is ostensibly equivalent to the far field solid value from the last solid-liquid tie line encountered as the sample is cooled. Making an analogy between this experimental procedure and our method we can argue that each simulation temperature can be associated with a particular composition for the solid sample (Fig 6.8). We make the argument that the anisotropy changes that we have observed are the result of far-field composition changes rather than temperature, or at least, are a convolved representation of both effects. The possibility that this numerical method was in fact capturing two effects was actually suspected in past work [28]. With this in mind we additionally argue that the experimental results in question are more correctly presented in terms of solid composition (rather than average). We follow this line of reasoning in the further analysis of our results.[1]

To obtain surface energy curves we initialized simulation profiles with far-field values for concentration and density obtained from the calculated phase diagram Fig 6.8 (or Fig 6.1). All simulations and the calculation of the phase diagram itself were done at a constant pressure of $p = -0.07$. Starting amplitude profiles as well as the chemical potentials μ_{eq} and μ_A were calculated from these values. The simulation was considered to be equilibrated when the total grand potential Ω converged up to 10^{-9}.

[1]We also note, given that interfacial energy doesn't change while moving along a constant temperature tie line, that the results presented here will not change qualitatively even if the changes in anisotropy are connected instead to the liquidus line.

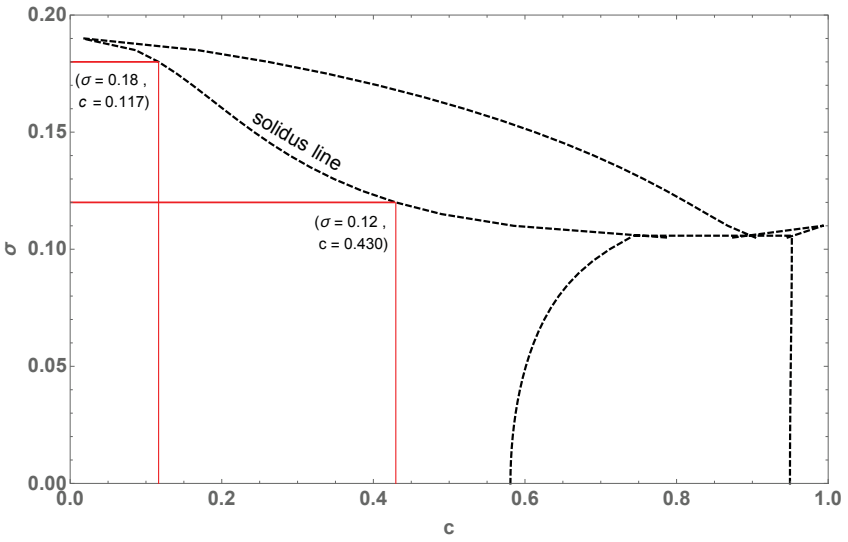

FIGURE 6.8: We illustrate the method by which a choice of temperature selects a particular associated concentration via its intersection with the solidus line of our calculated phase diagram (obtained with $p = -0.07$.)

Following this procedure and setup, we fitted the resulting surface energy to obtain interface stiffness as described in section 6.1. Figures 6.9 and 6.10 show the parameters γ_o and ϵ_4 resulting from these fits, in terms of both solidus concentration and temperature. We omit plots of the higher-order fitting parameters, but note that they follow the same general trend as ϵ_4, and report their values in Table 6.3.

σ	ϵ_8	ϵ_{12}	ϵ_{16}	ϵ_{20}	ϵ_{24}
0.12	-9.4×10^{-4}	-1.4×10^{-4}	-3.1×10^{-5}	-7.9×10^{-6}	-2.4×10^{-6}
0.13	-9.9×10^{-4}	-1.5×10^{-4}	-3.3×10^{-5}	-8.7×10^{-6}	-2.6×10^{-6}
0.14	-11.0×10^{-4}	-1.7×10^{-4}	-3.8×10^{-5}	-10.1×10^{-6}	-3.1×10^{-6}
0.15	-12.8×10^{-4}	-2.0×10^{-4}	-4.6×10^{-5}	-12.5×10^{-6}	-3.9×10^{-6}
0.16	-154×10^{-4}	-2.5×10^{-4}	-5.8×10^{-5}	-16.4×10^{-6}	-5.1×10^{-6}
0.17	-18.9×10^{-4}	-3.2×10^{-4}	-7.6×10^{-5}	-21.9×10^{-6}	-7.3×10^{-6}
0.18	-23.2×10^{-4}	-4.0×10^{-4}	-9.7×10^{-5}	-26.7×10^{-6}	-8.4×10^{-6}

TABLE 6.3: Higher order anisotropy parameters for interfacial energy curves, up to sixth order. Note the decrease in magnitude with increasing order.

We see that in terms of temperature the anisotropy ϵ_4 follows the same trend as is seen for the case of the equal stiffness species. The isotropic parameter γ_o, however, only shows this same behaviour for the high temperature/ low solidus concentration. Past $\sigma \approx 0.15$ ($c_S \approx 0.3$), we instead see the opposite behaviour, and γ_o decreases abruptly with decreasing temperature (and increasing concentration). We suggest as a possible explanation that we are observing two competing effects; for low c_S the previously reported constant-density temperature dependence [28] of the isotropy is seen. At sufficiently high c_S,

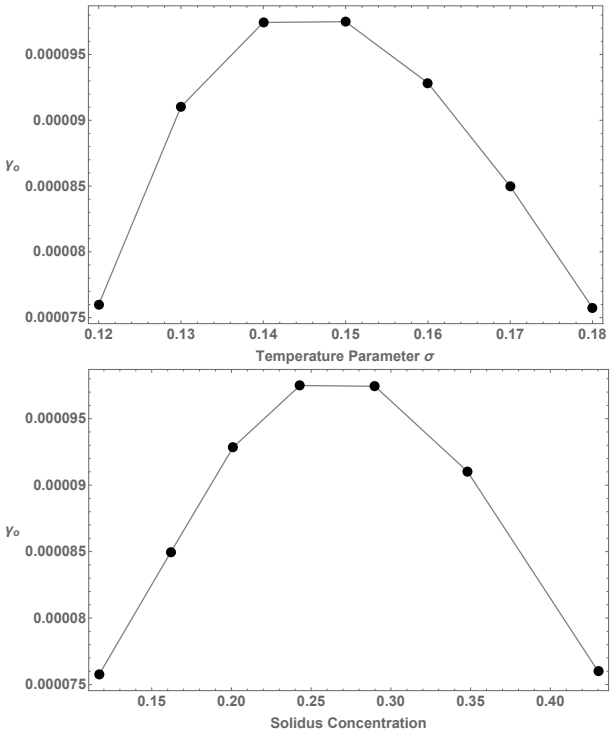

FIGURE 6.9: The isotropic fitting parameter γ_o, plotted in terms of both temperature and associated solidus concentration. For the higher temperature (low concentration) range the isotropy follows the behaviour seen in the comparable stiffness case (Fig 6.7); in the lower temperature (higher concentration) region its behaviour is inverted. However, the changes in this parameter are at least two orders of magnitude smaller than those observed in the anisotropy parameter and thus may not be significant.

however, this opposite behaviour may be due to the intrusion of the triangular species on the dominant square phase over this range of concentrations; namely, that the material wants to maintain an isotropic square structure but the intrusion of increasing amounts of the triangular species inhibits this. As such the preferred isotropic component is stronger the less the concentration of triangular species present; this corresponds to higher temperatures. In the equal stiffness case, the effect of increased triangle concentration is not as pronounced, and it is likely that the behaviour observed is solely due to temperature differences, possibly simply due to the inaccessability of higher concentrations. However in either case the change in γ_o is very small; on the scale of the anisotropy change, the isotropic component is effectively constant (Fig 6.11). Changes in γ_o are on the order of 10^{-5} and as such are not large enough to be considered statistically significant.

In terms of the anisotropic parameter ϵ_4, we note that in comparison to the 1% change in ϵ_4 seen in the pure material, we now observe a change an order of magnitude higher (10%) for the same difference in model temperature, or alternately for a difference in solidus concentration on the order of 0.01. In the scope of dendritic growth this is a very

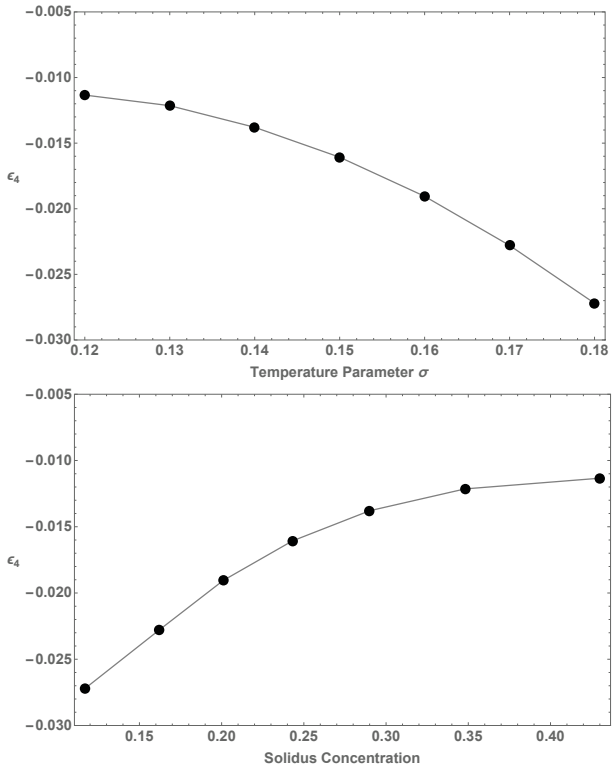

FIGURE 6.10: The first order anisotropic fitting parameter ϵ_4 plotted in terms of both temperature and associated solidus concentration. In both plots ϵ_4 appears to approach a plateau; it does so slightly more sharply in terms of concentration, as sufficiently high concentrations of the secondary species are reached. Higher values of concentration were not attainable within the square solid-liquid coexistence region of this XPFC alloy system.

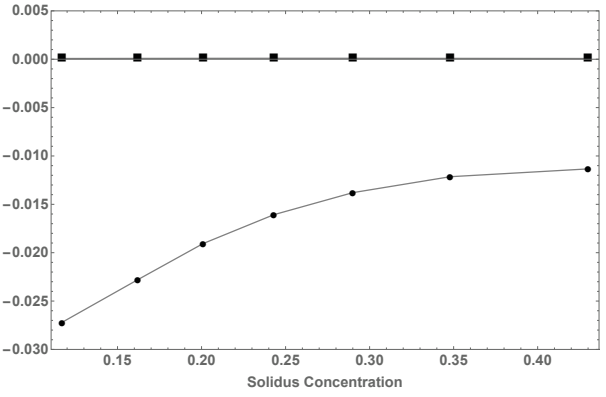

FIGURE 6.11: Isotropic γ (square) and anisotropic ϵ_4 (circle) fitting parameters plotted together in terms of solidus concentration; note that on the scale of ϵ_4 the values of the isotropic parameter are effectively constant.

significant predicted change. This agrees with the change in the dominant anisotropy parameter measured by Rappaz et al [1] over the same difference in solidus concentration, which is also on the order of 10%. We argue that this may be in part due to the influence of the solid concentration in the observed behaviour of the anisotropy, rather than the

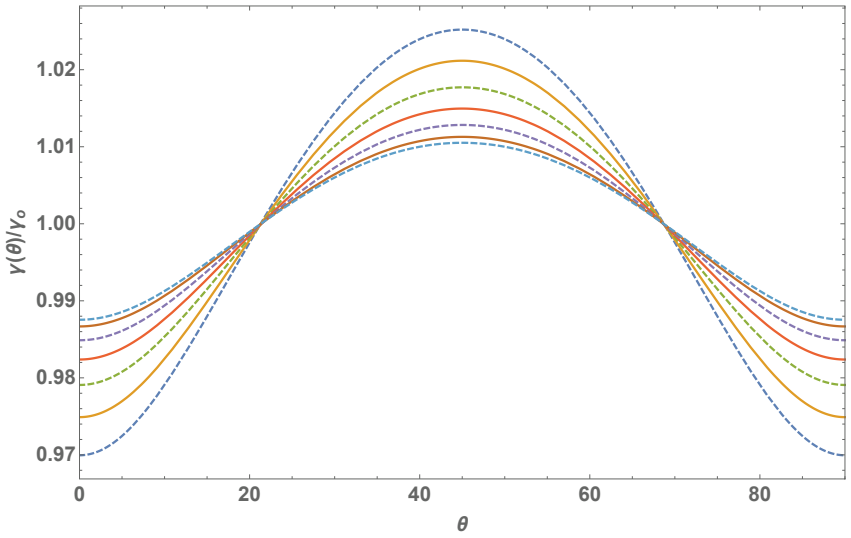

FIGURE 6.12: Normalized interfacial energies $\gamma(\theta)$ for the case of a large stiffness disparity between alloy species. The highest amplitude curves correspond to lowest solidus concentrations and vice versa. Concentrations shown are $0.117, 0.162, 0.201, 0.243, 0.290, 0.348, 0.430$. These curves were used to extract the data in Figures 6.9-6.10

presence of a temperature effect only; this is plausible in light of the observed plateau in the temperature versus concentration curve of the solidus line in Fig 6.1.

Figure 6.12 shows the interfacial energy curves used to extract the data in Figures 6.9 and 6.10. Figure 6.14 shows the corresponding normalized stiffness curves $\frac{S}{\gamma_o}$. We see a far more dramatic change than is observed for the equal stiffness case in Fig 6.6 or the pure material case in Chapter 4. In particular as a solidus composition of 0.5 is approached, the stiffness curve becomes notably more shallow and the global minimum at $\theta = 45°$ becomes far less well-defined; in fact we see a range from roughly 30° to 60° where the stiffness is almost flat, suggesting there is little preference for dendrite orientation within this range. These results in particular agree very well with the behaviour seen by Rappaz up to concentrations of 0.58 (Fig 6.13). We have not been able to observe the flip of the maxima to minima (and vice versa) that has been seen experimentally at higher concentrations of the second species; we attribute this to the fact that we have not been able to accurately reproduce the long, thin region of square liquid coexistence seen in the experimental Al-Zn phase diagram, and as such were not able to accurately model such high solidus concentrations with our simulation.

We surmise that the weakening stiffness curves that we observe with increased concentration are due to the presence of increasing amounts of species B, a soft material with

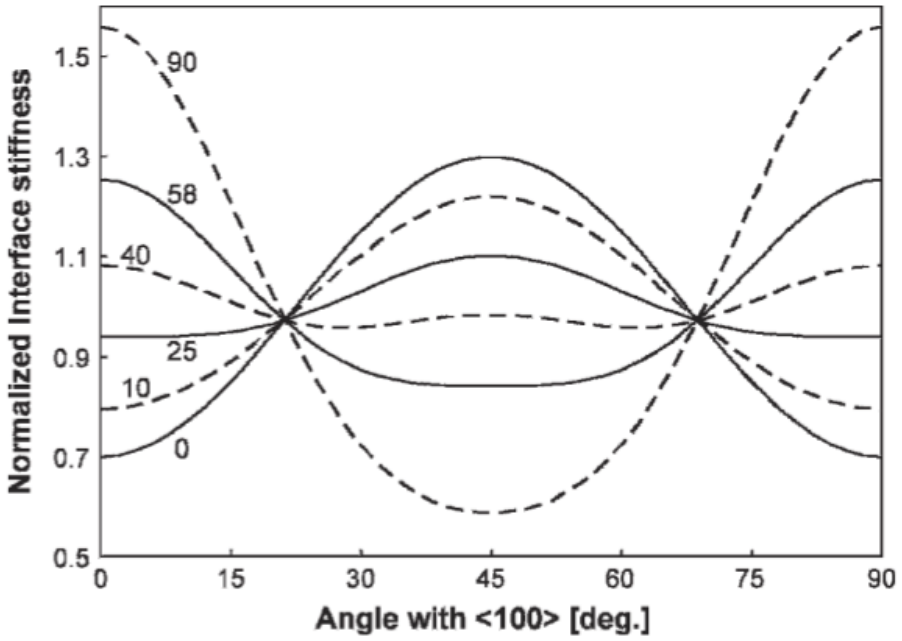

FIGURE 6.13: Angular variation of the normalized stiffness in the (001) plane for various zinc concentrations in Al-Zn, obtained via dendrite growth direction measured in experiments. Reprinted with permission from [1]

a preference for the triangle phase embedded in the square lattice structure. At low concentrations, where species A is still dominant, the crystal settles into a very stiff square lattice structure with little tolerance for misalignment. To illustrate this mechanism, we have engineered our system such that the square species is exceedingly stiff in comparison to the triangle species, and as such intermediate concentrations of the triangle phase are insufficient to produce stiffness minima reminiscent of a triangular crystal as has been seen in experimental work [1]; however, the influence of the increased amount of the second species is evident. Sufficient species B atoms present in the square species A lattice will, eventually, lead to the material overall becoming softer, as more and more of the lattice is made up of the low stiffness material. This is what is occuring in the flattened region of the $c_0 = 0.430$ curve in Fig 6.14. To our knowledge, this is the first fundamental theoretical study to examine the role of impurities on interfacial anisotropy, and to provide a mechanism to help explain the experimental results with regards to the role of impurities on dendritic anisotropy obtained by Rappaz et al [1].

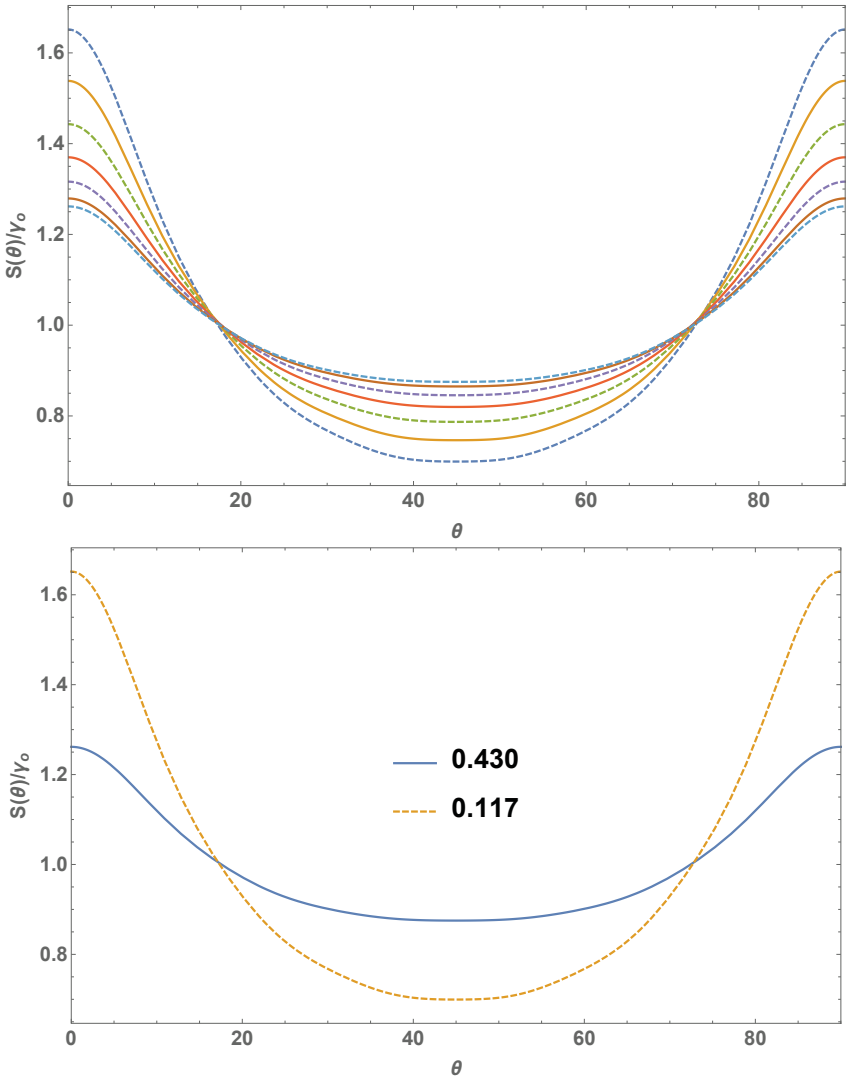

FIGURE 6.14: (Top) Normalized stiffness curves $S(\theta)/\gamma_o$ corresponding to the interfacial energy curves of Fig 6.12. The highest amplitude curves correspond to lowest solidus concentrations and vice versa. Concentrations shown are $0.117, 0.162, 0.201, 0.243, 0.290, 0.348, 0.430$. In the bottom figure the highest and lowest concentration curves obtained are presented to illustrate the extent to which the stiffness has changed.

Chapter 7

Conclusions

We have motivated this work in part due to experimental studies that have suggested a concentration dependence on interfacial anisotropy of certain metallic alloys. As this anisotropy determines dendrite growth directions, it is important to the microstructure of the material which in turn can determine the material properties. There is thus a great deal of practical import in determining the mechanism behind this relationship.

The work done by Rappaz et al[1] in particular measured the changing anisotropy via dendrite orientation in fully solidified samples. We have instead made use of an established microscopic theory for measuring the anisotropy inherent in an equilibrium solid-liquid interface, namely, a phase field crystal model coarse grained to obtain an equivalent amplitude-expansion phase field model. For the case of constant temperature, we did not see any change in interfacial anisotropy with average concentration. This was to be expected, as for each average concentration value at a given constant temperature we were still restricted to the same set of far field (i.e. bulk phase) values and thus there was no mechanism for changing the interfacial energy. We did however observe a fairly large change in the anisotropy of the interfacial energy (and interfacial stiffness) with temperature.

In attempting to understand these results we make an important distinction; namely, that in our studies of the solid-liquid coexistence region, the significant value is not the average concentration of the material, but rather, the far-field solid concentration. With this in mind we argue that the effect of varying temperature is actually (or at least, is primarily) to move the system to different values along the solidus line. The concentrations at which experimental results are reported for fully solidified samples should then most correctly be determined by the point at which the solidus line was

crossed as the sample was cooled. Note that one could follow the liquidus line as well and would obtain the same qualitative results as those we have reported, albeit tied to different concentrations.

Our simulation results help us to explain this behaviour observed in experiments (reported in Fig 6.13) by the increased percentage of secondary species atoms infiltrating the preferred lattice structure of the primary species. In the case where the two species prefer different lattice symmetries, and one of the species is sufficiently stiff in comparison to the other, softer material, we may not see a discontinuous transition from one preferred dendrite orientation to another. Rather, the stiffer material may hold on to its preferred structure while becoming increasingly 'mushy' in certain directions due to the increased presence of the softer material. Our simulation results suggest that this can lead to flattened regions of the stiffness curves that exhibit no strongly preferred direction for dendrite growth. Our results also showed that the role of concentration, modulated presumably by temperature, causes a much more significant change in interface anisotropy than does a change in temperature in a single component material. This is consistent with experiments that have observed significant anisotropy change in binary alloys.

We have simulated one dimensional interface cuts using a one dimensional binary alloy amplitude model, derived from the XPFC model, as a method of studying this phenomenon. We argue that observing anisotropy in terms of the equilibrium solid-liquid interface is not only sufficient, but is perhaps the more correct way of characterizing this concentration dependence, due to the model's connection to elemental interactions inherited from the liquid state correlation functions built into the XPFC model.

This behaviour is still not fully characterized nor understood, however, and two avenues of further study in particular are evident.

The first is in the construction of the phase diagram itself. We have stated that given the approximation used we were unable to exactly reproduce the shape of the Al Zn phase diagram for which the changing interfacial anisotropy has been observed experimentally. The creation of a more accurate analagous phase diagram, presumably via the inclusion of high order terms in the ideal and excess components of the free energy, would allow our simulation to access higher values of the solidus concentration. We expect that this would allow a numerical determination of the full variation of the stiffness anistropy from the preferred crystal stiffness form of the first species to that of the second.

The second is somewhat complex. We have been unable to completely separate the temperature and concentration dependence of the interfacial anisotropy, althought a comparison of our constant σ versus changing σ anisotropy results does strongly indicate that the role of concentration on interface anisotropy is modulated by temperature as a control. As part of this work we have obtained a greater understanding of the behaviour of the binary alloy phase diagram in all its relevant thermodynamic variables. As such we are forced to conclude that this convolved effect is a limitation of the accessible phase space.

The majority of past computational studies of binary alloys have made use of a simplified phase diagram [24][28] in which the density field is effectively set to zero. In this work we have demonstrated the method for calculating a full phase diagram in both density and concentration space, and in doing so have also been able to map out the variation of the equilibrium properties of binary alloys as a function of temperature, density, concentration and pressure variables.

In particular, in calculating the three-dimensional phase diagram we found that not every density and concentration combination is possible in a binary alloy; choosing n_0 and c_0 haphazardly may still give solutions, but at arbitrary points in pressure space. We are thus still restricted to a single coexistence tie line at a given temperature.

We expect that this may change upon moving to higher order alloys, i.e. the ternary. The addition of a second concentration field should create a phase space wherein multiple tie lines can be constructed for a particular temperature, and we can thus create a coexistence plane rather than just a coexistence line.

It should be relatively straightforward to obtain both a phase diagram and dynamics equations for a ternary alloy by following the same procedure outlined in this work, namely, beginning with a grand potential formulation of the form

$$\Omega[\rho_A, \rho_B] = F[\rho_A, \rho_B] - \mu_A \int \rho_A(\vec{r})d\vec{r} - \mu_B \int \rho_B(\vec{r})d\vec{r} - \mu_C \int \rho_C(\vec{r})d\vec{r} \tag{7.1}$$

Calculating the phase diagram would now require six values to be solved for (due to the addition of two far field values for the additional concentration field), and as such two additional equations would be necessary. The expression for the additional chemical potential μ_c should provide one of these; there may be a way to make use of the lever rule, for example, as a second.

The ability to access multiple far field concentrations at a single temperature may thus be the key to further elucidating the concentration dependence of surface anisotropy,

potentially freeing us from the indistinct combination of temperature and concentration effects.

Appendix A

Effective Correlation Function Terms used in the XPFC Binary Alloy

Beginning with correlation function terms in AA, AB, BA and BB as described in Section 2.2.3, we start with the form:

$$\delta\rho_A \int C^{AA}\delta\rho'_A + \delta\rho_B C^{BB}\delta\rho'_B + \delta\rho_A \int C^{AB}\delta\rho'_B + \delta\rho_B \int C^{BA}\delta\rho'_A \tag{A.1}$$

we consider each correlation term separately and perform the variable transforms in Eq 2.23.

Starting with the AA term:

$$\begin{aligned}
\delta\rho_A \int C^{AA}\delta\rho'_A &= (\rho_A - \rho_A^0)C^{AA}(\rho'_A - \rho'^0_A) \\
&= \rho_A C^{AA}\rho'_A - \rho_A^0 C^{AA}\rho'_A \\
&= (1-c)(n+1)\rho^0 C^{AA}(1-c)(n'+1)\rho^0 - (1-c^0)(n^0+1)\rho^0 C^{AA}(1-c)(n'+1)\rho^0 \\
&= n(1-c)^2 C_2^{AA} n' - n(1-c)C_2^{AA}c - (c-c^0)(1-c)C_2^{AA}n' + (c-c^0)C_2^{AA}c
\end{aligned} \tag{A.2}$$

where we have divided by ρ_0 to go from C^{AA} to C_2^{AA}. We can see that we have a term in n', a term in c, a term inc^0 and n', and a term in c^0 and c. These four categories will provide the grouping used to obtain expressions C^n_{eff}, C^c_{eff},$C^{c_0 n}_{eff}$, and $C^{c_0 c}_{eff}$.

For the BB term:

$$\begin{aligned}\delta\rho_B \int C^{BB}\delta\rho'_B &= (\rho_B - \rho_B^0)C^{BB}(\rho'_B - \rho'^0_B)\\ &= \rho_B C^{BB}\rho'_B - \rho_B^0 C^{BB}\rho'_B\\ &= c(n+1)\rho^0 C^{BB}c(n'+1)\rho^0 - c^0(n^0+1)\rho^0 C^{BB}c(n'+1)\rho^0\\ &= nc^2C^{BB}n' + ncC^{BB}c + (c-c^0)cC^{BB}n' + (c-c^0)C^{BB}c\end{aligned} \tag{A.3}$$

For the AB term:

$$\begin{aligned}\delta\rho_A \int C^{AB}\delta\rho'_B &= (\rho_A - \rho_A^0)C^{AB}(\rho'_B - \rho'^0_B)\\ &= \rho_A C^{AB}\rho'_B - \rho_A^0 C^{AB}\rho'_B\\ &= (1-c)(n+1)\rho^0 C^{AB}c(n'+1)\rho^0 - (1-c^0)(n^0+1)\rho^0 C^{AB}c(n'+1)\rho^0\\ &= nc(1-c)C^{AB}n' + n(1-c)C^{AB}c - (c-c^0)cC^{AB}n' - (c-c^0)C^{AB}c\end{aligned} \tag{A.4}$$

And finally, for the BA term:

$$\begin{aligned}\delta\rho_B \int C^{BA}\delta\rho'_A &= (\rho_B - \rho_B^0)C^{BA}(\rho'_A - \rho'^0_A)\\ &= \rho_B C^{BA}\rho'_A - \rho_B^0 C^{BA}\rho'_A\\ &= c(n+1)\rho^0 C^{BA}(1-c)(n'+1)\rho^0 - c^0(n^0+1)\rho^0 C^{BA}(1-c)(n'+1)\rho^0\\ &= nc(1-c)^2C^{BA}n' - ncC^{BA}c + (c-c^0)(1-c)C^{BA}n' - (c-c^0)C^{BA}c\end{aligned} \tag{A.5}$$

Grouping the terms as described above, we can then obtain:

$$
\begin{aligned}
C^{n}_{eff} &= c^2 C_2^{BB} + (1-c)^2 C_2^{AA} + c(1-c)(C_2^{BA} + C_2^{AB}) \\
C^{c}_{eff} &= c(C_2^{BB} - C_2^{BA}) - (1-c)(C_2^{AA} - C_2^{AB}) \\
C^{c_0 n}_{eff} &= c(C_2^{BB} - C_2^{AB}) - (1-c)(C_2^{AA} - C_2^{BA}) \\
C^{c_0 c}_{eff} &= C_2^{BB} + C_2^{AA} - (C_2^{BA} + C_2^{AB})
\end{aligned}
\tag{A.6}
$$

Appendix B

Amplitude Expansion of the XPFC Free Energy Functional

Beginning with the binary alloy free energy in Eq 2.31, we demonstrate in this section how to recover a PF type model expression. The key consideration here is the separation of timescales of the model. We consider the mode approximation of the density, which has the form

$$n = n_0(\vec{r}) + \sum_{\vec{G}} \eta_{\vec{G}} e^{i\vec{G}.\vec{r}} + c.c. \tag{B.1}$$

where $n_0(\vec{r})$ is the average density, and the $\eta_{\vec{G}}$ are the amplitudes of the oscillations in density. In addition for the alloy we have concentration field, $c(\vec{r})$. These amplitudes and the average fields in density and concentration are all slow-varying in terms of atomic timescales. The goal of the amplitude expansion procedure that follows is effectively to coarse-grain this model such that only these slow variables remain; that is, the oscillating exponential factors themselves will no longer remain. To lowest order this amounts to retaining the terms in which the oscillatory exponential factors go to zero.

Formally, this is done by making use of a volume-averaging function which is normalized such that

$$\int d\vec{r'} X_V(\vec{r} - \vec{r'}) = 1 \tag{B.2}$$

and which acts on a function $f(\vec{r})$ to be coarse-grained as

$$\langle f(\vec{r})\rangle_V \equiv \int d\vec{r'} f(\vec{r'}) X_V(\vec{r}-\vec{r'}) \tag{B.3}$$

The Fourier transform of this function can be written as

$$X_V(\vec{r}-\vec{r'}) = \int d\vec{k} \hat{X}_V(|\vec{k}|) e^{i\vec{k}\cdot(\vec{r}-\vec{r'})} \tag{B.4}$$

We present the formal derivation, using a generic mode approximation, below.

Consider first the ideal terms. We begin by substituting in the mode approximation. Using the n^2 term to demonstrate:

$$\begin{aligned}\int d\vec{r} n(\vec{r})^2 = &\int d\vec{r} \sum_{j,l} \eta_j(\vec{r})\eta_l(\vec{r}) e^{i(\vec{G}_j+\vec{G}_l)\cdot\vec{r})} \\ &+ \int d\vec{r} \sum_{j,l} \eta_j(\vec{r})\eta_l^\dagger(\vec{r}) e^{i(\vec{G}_j-\vec{G}_l)\cdot\vec{r})} \\ &+ \int d\vec{r} \sum_{j,l} \eta_j^\dagger(\vec{r})\eta_l(\vec{r}) e^{i(\vec{G}_l-\vec{G}_j)\cdot\vec{r})} \\ &+ \int d\vec{r} \sum_{j,l} \eta_j^\dagger(\vec{r})\eta_l^\dagger(\vec{r}) e^{-i(\vec{G}_j+\vec{G}_l)\cdot\vec{r})}\end{aligned} \tag{B.5}$$

We can make use of Eq. B.2 to multiply all terms by one.

$$\begin{aligned}&\sum_{j,l} \int d\vec{r} \int d\vec{r'} X_V(\vec{r}-\vec{r'})\eta_j(\vec{r})\eta_l(\vec{r}) e^{i(\vec{G}_j+\vec{G}_l)\cdot\vec{r})} \\ +&\sum_{j,l} \int d\vec{r} \int d\vec{r'} X_V(\vec{r}-\vec{r'})\eta_j(\vec{r})\eta_l^\dagger(\vec{r}) e^{i(\vec{G}_j-\vec{G}_l)\cdot\vec{r})} \\ +&\sum_{j,l} \int d\vec{r} \int d\vec{r'} X_V(\vec{r}-\vec{r'})\eta_j^\dagger(\vec{r})\eta_l(\vec{r}) e^{i(\vec{G}_l-\vec{G}_j)\cdot\vec{r})} \\ +&\sum_{j,l} \int d\vec{r} \int d\vec{r'} X_V(\vec{r}-\vec{r'})\eta_j^\dagger(\vec{r})\eta_l^\dagger(\vec{r}) e^{-i(\vec{G}_j+\vec{G}_l)\cdot\vec{r})}\end{aligned} \tag{B.6}$$

Taking, for example, the first term, the limiting procedure is applied by switching the order of integration:

$$\int d\vec{r'} \int d\vec{r} X_V(\vec{r} - \vec{r'}) \eta_j(\vec{r}) \eta_l(\vec{r}) e^{i(\vec{G}_j + \vec{G}_l)\cdot\vec{r}} \tag{B.7}$$

We now make use of the assumption that the amplitudes η_j are slow-varying compared to the volume-averaging scale to justify taking a Taylor expansion of the amplitudes around $\vec{r'} = \vec{r}$ (to second order). Inserting the expansion into Eq B.7 gives

$$\begin{aligned}
&\int d\vec{r'} \int d\vec{r} X_V \left(\eta_j(\vec{r}) + (\vec{r} - \vec{r'})_1 \partial_{\vec{r'_1}} \eta_j(\vec{r}) + \frac{1}{2} (\vec{r} - \vec{r'})_2 (\vec{r} - \vec{r'})_1 \partial_{\vec{r'_2}} \partial_{\vec{r'_1}} \eta_j(\vec{r}) \right) \\
&\left(\eta_l(\vec{r}) + (\vec{r} - \vec{r'})_1 \partial_{\vec{r'_1}} \eta_l(\vec{r}) + \frac{1}{2} (\vec{r} - \vec{r'})_2 (\vec{r} - \vec{r'})_1 \partial_{\vec{r'_2}} \partial_{\vec{r'_1}} \eta_l(\vec{r}) \right) e^{i(\vec{G}_j + \vec{G}_l)\cdot\vec{r}}
\end{aligned} \tag{B.8}$$

Expanding out this expression and pulling the $\vec{r'}$ terms out of the $\vec{r}$ integral, we get integrals in $\vec{r}$ of the from zeroth to fourth order with the forms:

$$\int d\vec{r} X_V e^{i(\vec{G}_j + \vec{G}_l)\cdot\vec{r}} \tag{B.9}$$

$$\int d\vec{r} X_V (\vec{r} - \vec{r'})_1 e^{i(\vec{G}_j + \vec{G}_l)\cdot\vec{r}} \tag{B.10}$$

$$\int d\vec{r} X_V (\vec{r} - \vec{r'})_2 (\vec{r} - \vec{r'})_1 e^{i(\vec{G}_j + \vec{G}_l)\cdot\vec{r}} \tag{B.11}$$

$$\int d\vec{r} X_V (\vec{r} - \vec{r'})_2 (\vec{r} - \vec{r'})_1 (\vec{r} - \vec{r'})_1 e^{i(\vec{G}_j + \vec{G}_l)\cdot\vec{r}} \tag{B.12}$$

$$\int d\vec{r} X_V (\vec{r} - \vec{r'})_2 (\vec{r} - \vec{r'})_1 (\vec{r} - \vec{r'})_2 (\vec{r} - \vec{r'})_1 e^{i(\vec{G}_j + \vec{G}_l)\cdot\vec{r}} \tag{B.13}$$

Eq. B.9 can be simplified by substituting in the Fourier transform of the volume averaging function as follows.

$$\begin{aligned}
\int d\vec{r} X_V e^{i(\vec{G}_j + \vec{G}_l)\cdot\vec{r}} &= \int d\vec{r} \int d\vec{k} \hat{X}_V(|\vec{k}|) e^{i\vec{k}\cdot(\vec{r} - \vec{r'})} e^{i(\vec{G}_j + \vec{G}_l)\cdot\vec{r}} \\
&= \int d\vec{k} \hat{X}_V(|\vec{k}|) e^{-i\vec{k}\cdot\vec{r'}} \delta(\vec{k} + \vec{G}_j + \vec{G}_l) \\
&= \hat{X}_V(|\vec{G}_j + \vec{G}_l|) e^{i(\vec{G}_j + \vec{G}_l)\cdot\vec{r'}}
\end{aligned} \tag{B.14}$$

For the remaining expressions, we also perform repeated partial integrations to get rid of the $(\vec{r}-\vec{r'})$ terms.

$$\begin{aligned}\int d\vec{r} X_V(\vec{r}-\vec{r'})_1 e^{i(\vec{G}_j+\vec{G}_l)\cdot\vec{r}} &= \int d\vec{r}\int d\vec{k}\hat{X}_V(|\vec{k}|)e^{i\vec{k}\cdot(\vec{r}-\vec{r'})}(\vec{r}-\vec{r'})_1 e^{i(\vec{G}_j+\vec{G}_l)\cdot\vec{r}} \\ &= \int d\vec{r}\int d\vec{k}\hat{X}_V(|\vec{k}|)\left(-i\partial_{\vec{k}_1}e^{i\vec{k}\cdot(\vec{r}-\vec{r'})}\right)e^{i(\vec{G}_j+\vec{G}_l)\cdot\vec{r}} \\ &= i\left(\partial_{\vec{k}_1}\hat{X}_V(|\vec{G}_l+\vec{G}_j|)\right)e^{i(\vec{G}_l+\vec{G}_j)\cdot\vec{r'}} \end{aligned} \tag{B.15}$$

$$\begin{aligned}\int d\vec{r} X_V(\vec{r}-\vec{r'})_2(\vec{r}-\vec{r'})_1 e^{i(\vec{G}_j+\vec{G}_l)\cdot\vec{r}} &= \int d\vec{r}\int d\vec{k}\hat{X}_V(|\vec{k}|)\left(i^2\partial_{\vec{k}_2}\partial_{\vec{k}_1}e^{i\vec{k}\cdot(\vec{r}-\vec{r'})}\right)e^{i(\vec{G}_j+\vec{G}_l)\cdot\vec{r}} \\ &= -i^2\left(\partial_{\vec{k}_1}\partial\vec{k}_2\hat{X}_V(|\vec{G}_l+\vec{G}_j|)\right)e^{i(\vec{G}_l+\vec{G}_j)\cdot\vec{r'}} \end{aligned} \tag{B.16}$$

$$\begin{aligned}&\int d\vec{r} X_V(\vec{r}-\vec{r'})(\vec{r}-\vec{r'})_2(\vec{r}-\vec{r'})_1(\vec{r}-\vec{r'})_1 e^{i(\vec{G}_j+\vec{G}_l)\cdot\vec{r}} \\ &= \int d\vec{r}\int d\vec{k}\hat{X}_V(|\vec{k}|)\left(-i^3\partial_{\vec{k}_3}\partial_{\vec{k}_2}\partial\vec{k}_1 e^{i\vec{k}\cdot(\vec{r}-\vec{r'})}\right)e^{i(\vec{G}_l+\vec{G}_j)\cdot\vec{r'}} \\ &= i^3\left(\partial_{\vec{k}_1}\partial_{\vec{k}_2}\partial_{\vec{k}_3}\hat{X}_V(|\vec{G}_l+\vec{G}_j|)\right)e^{i(\vec{G}_l+\vec{G}_j)\cdot\vec{r'}} \end{aligned} \tag{B.17}$$

$$\begin{aligned}&\int d\vec{r} X_V(\vec{r}-\vec{r'})(\vec{r}-\vec{r'})_2(\vec{r}-\vec{r'})_1(\vec{r}-\vec{r'})_2(\vec{r}-\vec{r'})_1 e^{i(\vec{G}_j+\vec{G}_l)\cdot\vec{r}} \\ &= \int d\vec{r}\int d\vec{k}\hat{X}_V(|\vec{k}|)\left(i^4\partial_{\vec{k}_1}\partial_{\vec{k}_2}\partial_{\vec{k}_3}\partial_{\vec{k}_4}e^{i\vec{k}\cdot(\vec{r}-\vec{r'})}\right)e^{i(\vec{G}_l+\vec{G}_j)\cdot\vec{r}} \\ &= -i^4\left(\partial_{\vec{k}_1}\partial_{\vec{k}_2}\partial_{\vec{k}_3}\partial_{\vec{k}_4}\hat{X}_V(|\vec{G}_l+\vec{G}_j|)\right)e^{i(\vec{G}_l+\vec{G}_j)\cdot\vec{r'}} \end{aligned} \tag{B.18}$$

Inserting each of these expressions back into the integral over $\vec{r'}$, we can now apply the volume averaging function to the exponential terms of the form $e^{i(\vec{G}_l+\vec{G}_j)\cdot\vec{r'}}$. These terms represent oscillatory functions on the scale of the lattice spacing a of the crystal structure, while the limiting factor of the averaging function restricts us to length scales significantly greater than a. Thus any surviving exponential terms will go to zero.

The only terms that will survive are those at resonance, that is, with $e^{i(\pm\vec{G}_l \pm \vec{G}_j)\cdot\vec{r}'}$ such that $(\pm\vec{G}_l \pm \vec{G}_j)$ equals zero. With only two $\vec{G}$ vectors this amounts to the case $(\vec{G}_l - \vec{G}_j)$ where $j = l$. Thus for the n^2 term we are left with

$$\sum_j \left[\int d\vec{r} \int d\vec{r'} X_V(\vec{r} - \vec{r'}) \eta_j(\vec{r}) \eta_j^\dagger(\vec{r}) + \int d\vec{r} \int d\vec{r'} X_V(\vec{r} - \vec{r'}) \eta_j^\dagger(\vec{r}) \eta_j(\vec{r}) \right] \tag{B.19}$$

where we make use of Eq B.2 to write the final contribution to the coarse-grained expression from the n^2 term:

$$2 \sum_j \int d\vec{r} |\eta_j(\vec{r})|^2 \tag{B.20}$$

The same procedure is applied to the n^3 and n^4 terms. We can take a shortcut by simply determining which combinations of vectors $\vec{G}_j$ will give resonance for each order, and retaining the corresponding combinations of amplitudes.

For the square-triangle binary alloy with mode approximation

$$n(\vec{r}) = n_0 + \sum_j^2 A_j e^{i\vec{k}_j \cdot \vec{r}} + \sum_l^2 B_l e^{i\vec{q}_l \cdot \vec{r}} + \sum_m^3 C_m e^{i\vec{Q}_m \cdot \vec{r}} + c.c. \tag{B.21}$$

where the A_j correspond to the $(1,0)$ square vectors, the B_l to the $(1,1)$ square vectors, and the C_m to the $(1,0)$ triangle vectors, the surviving 3 and 4 vector combinations are:

$$\begin{aligned} \vec{Q}_1 + \vec{Q}_2 + \vec{Q}_3 \text{ (and c.c.)} \\ \vec{q}_1 - \vec{k}_1 - \vec{k}_2 \text{ (and c.c.)} \\ \vec{q}_2 - \vec{k}_1 + \vec{k}_2 \text{ (and c.c.)} \\ -\vec{k}_1 - \vec{k}_1 + \vec{q}_1 - \vec{q}_2 \text{ (and c.c.)} \\ -\vec{k}_2 - \vec{k}_2 + \vec{q}_1 + \vec{q}_2 \text{ (and c.c.)} \end{aligned} \tag{B.22}$$

and so the final coarse-grained expression resulting from the ideal terms is

$$
\begin{aligned}
F_{id(cg)} = &\int d\vec{r}\left(1-\eta n_0+\chi n_0^2\right)\left(A_1^2+A_2^2+B_1^2+B_2^2+C_1^2+C_2^2+C_3^2\right)\\
&+\frac{1}{2}n_0^2-\frac{\eta}{6}n_0^3+\frac{\chi}{12}n_0^4+\omega(n_0+1)\Delta F_{mix}(c)\\
&+\left(4\chi n_0-2\eta\right)\left(A_1A_2B_1+A_1A_2B_2+C_1C_2C_3\right)\\
&+\frac{\chi}{2}\left(A_1^4+A_2^4+B_1^4+B_2^4+C_1^4+C_2^4+C_3^4\right)\\
&+2\chi A_1^2\left(B_1B_2+C_2C_3\right)+2\chi A_1^2\left(A_2^2+B_1^2+B_2^2+C_1^2+C_2^2+C_3^2\right)\\
&+2\chi A_1^2B_1B_2+2\chi A_2^2\left(B_1^2+B_2^2+C_1^2+C_2^2+C_3^2\right)\\
&+2\chi B_1^2\left(B_2^2+C_1^2+C_2^2+C_3^2\right)+2\chi B_2^2\left(C_1^2+C_2^2+C_3^2\right)\\
&+2\chi C_1^2\left(C_2^2+C_3^2\right)+2\chi C_2^2C_3^2+4\chi B_1B_2BC_2C_3
\end{aligned}
\tag{B.23}
$$

We now proceed with the coarse graining of the excess term of Eq 2.31. There is no coarse graining required for the purely concentration term $\alpha|\nabla c|^2$ and so we are only concerned with the correlation function term. For now we write the interpolated correlation function as $X_1(c)C_2^{AA}+X_2(c)C_2^(BB)=C_2^{eff}(|\vec{r}-\vec{r'}|)$. Note that

$$
C_2^{eff}(|\vec{r}-\vec{r'}|)=\int d\vec{k}\hat{C}_2(|\vec{k}|)e^{i\vec{k}\cdot(\vec{r}-\vec{r'})}
\tag{B.24}
$$

Substituting the Fourier transform into the excess term we get

$$
-\int\frac{1}{2}d\vec{r}n(\vec{r})\int d\vec{r'}\int d\vec{k}\hat{C}_2(|\vec{k}|)e^{i\vec{k}\cdot(\vec{r}-\vec{r'})}n(\vec{r'})
\tag{B.25}
$$

As previously, we substitute in the full mode expansion (Eq B.21) for $n(\vec{r'})$ into Eq B.25 and Taylor expand the amplitudes around $\vec{r}=\vec{r'}$. For clarity we neglect to put in the mode expansion for the leading $n(\vec{r})$ for the time being.

$$
\begin{aligned}
&-\frac{1}{2}\int d\vec{r}n(\vec{r})\int d\vec{r'}\int d\vec{k}\hat{C}_2(|\vec{k}|)\sum_j\{\eta_j(\vec{r})+(\vec{r'}-\vec{r})_1\partial_{\vec{r}_1}\eta_j(\vec{r})\\
&+\frac{1}{2}(\vec{r'}-\vec{r})_2(\vec{r'}-\vec{r})_1\partial_{\vec{r}_2}\partial_{\vec{r}_1}\eta_j(\vec{r})\}e^{i\vec{G}_j\cdot\vec{r}}e^{i\vec{k}\cdot(\vec{r}-\vec{r'})}\\
&-\frac{1}{2}\int d\vec{r}n(\vec{r})\int d\vec{r'}\int d\vec{k}\hat{C}_2\sum_j\{\eta_j^\dagger(\vec{r})+(\vec{r'}-\vec{r})_1\partial_{\vec{r}_1}\eta_j^\dagger(\vec{r})\\
&+\frac{1}{2}(\vec{r'}-\vec{r})_2(\vec{r'}-\vec{r})_1\partial_{\vec{r}_2}\partial_{\vec{r}_1}\eta_j^\dagger(\vec{r})\}e^{-i\vec{G}_j\cdot\vec{r}}e^{i\vec{k}\cdot(\vec{r}-\vec{r'})}
\end{aligned}
\tag{B.26}
$$

We can now insert the volume averaging function Eq B.2 as before; we obtain zeroth, first and second order integrals of the forms in Eq B.9 - B.11. As previously for the first and second order forms, we perform partial integration (repeated as necessary) to eliminate the $(\vec{r} - \vec{r'})$ terms. After evaluating the integrals we get the following forms.

For zeroth order:

$$-\frac{1}{2}\int d\vec{r} n(\vec{r}) \sum_j \hat{C}_2(|\vec{G}_j|)\eta_j(\vec{r})e^{i\vec{G}_j\cdot\vec{r}} \tag{B.27}$$

For first order:

$$-\frac{1}{2}\int d\vec{r} n(\vec{r}) \sum_j (-i)\partial_{\vec{k}_1}\hat{C}_2(|\vec{G}_j|)\partial_{\vec{r}_1}\eta_j(\vec{r})e^{i\vec{G}_j\cdot\vec{r}} \tag{B.28}$$

And for second order:

$$-\frac{1}{2}\int d\vec{r} n(\vec{r}) \sum_j \frac{i^2}{2}\partial_{\vec{k}_2}\partial_{\vec{k}_1}\hat{C}_2(|\vec{G}_j|)\partial_{\vec{r}_2}\partial_{\vec{r}_1}\eta_j(\vec{r})e^{i\vec{G}_j\cdot\vec{r}} \tag{B.29}$$

Now we can insert the mode expansion for the $n(\vec{r})$ term. Rather than explicitly writing out all possible combinations, we simply recall the resonance condition described previously. The highest order terms in amplitude that we acquire are only second order, and so we just have to be concerned with the case where $j = l$. The surviving terms are then

$$\begin{aligned}\sum_j \int d\vec{r}\hat{C}_2(|\vec{G}_j|)\eta_j\eta_j^\dagger - i\partial_{\vec{k}_1}\hat{C}_2(|\vec{G}_j|)\eta_j\partial_{\vec{r}_1}\eta_j^\dagger + \frac{i^2}{2}\partial_{\vec{k}_2}\partial_{\vec{k}_1}\hat{C}_2(|\vec{G}_j|)\eta_j\partial_{\vec{r}_2}\partial_{\vec{r}_1}\eta_j^\dagger \\ + \quad \hat{C}_2(|\vec{G}_j|)\eta_j^\dagger\eta_j - i\partial_{\vec{k}_1}\hat{C}_2(|\vec{G}_j|)\eta_j^\dagger\partial_{\vec{r}_1}\eta_j + \frac{i^2}{2}\partial_{\vec{k}_2}\partial_{\vec{k}_1}\hat{C}_2(|\vec{G}_j|)\eta_j^\dagger\partial_{\vec{r}_2}\partial_{\vec{r}_1}\eta_j\end{aligned} \tag{B.30}$$

Recall that the XPFC model constructs the terms of the correlation functions as Gaussians around the reciprocal space lattice vectors; as such the first derivative of $\hat{C}_2(|\vec{G}_j|)$ must be zero. We are left with

$$\sum_j \int d\vec{r}\hat{C}_2(|\vec{G}_j|)\eta_j\eta_j^\dagger + \frac{i^2}{2}\partial_{\vec{k}_2}\partial_{\vec{k}_1}\hat{C}_2(|\vec{G}_j|)\eta_j\partial_{\vec{r}_2}\partial_{\vec{r}_1}\eta_j^\dagger$$
$$+ \quad \hat{C}_2(|\vec{G}_j|)\eta_j^\dagger\eta_j + \frac{i^2}{2}\partial_{\vec{k}_2}\partial_{\vec{k}_1}\hat{C}_2(|\vec{G}_j|)\eta_j^\dagger\partial_{\vec{r}_2}\partial_{\vec{r}_1}\eta_j \tag{B.31}$$

We can also eliminate the terms of the form $\eta_j\partial_{\vec{r}_2}\partial_{\vec{r}_1}\eta_j^\dagger$ by integrating by parts to obtain:

$$\begin{aligned}
&\int d\vec{r}\left(\eta_j\partial_{\vec{r}_2}\partial_{\vec{r}_1}\eta_j^\dagger + \eta_j^\dagger\partial_{\vec{r}_2}\partial_{\vec{r}_1}\eta_j\right) \\
&= 2\int d\vec{r}\left(\partial_{\vec{r}}\eta_j^\dagger\partial_{\vec{r}}\eta_j\right) \\
&= 2\int d\vec{r}|\nabla\eta_j|^2
\end{aligned} \tag{B.32}$$

We now calculate the second derivative of the effective correlation function $\hat{C}_2^{eff}$:

$$\begin{aligned}
\partial_{\vec{k}_1}\partial_{\vec{k}_2}\hat{C}_2^{eff} &= \partial_{\vec{k}_1}\partial_{\vec{k}_2}\left(X_1(c)\hat{C}_2^{AA} + X_2(c)\hat{C}_2^{BB}\right) \\
&= \partial_{\vec{k}_1}\left(X_1(c)\hat{C'}_2^{AA} + X_2(c)\hat{C'}_2^{BB}\right)\frac{\vec{k}}{|\vec{k}|} \\
&= \left(X_1(c)\hat{C''}_2^{AA} + X_2(c)\hat{C''}_2^{BB}\right)\frac{\vec{k}^2}{|\vec{k}|^2}
\end{aligned} \tag{B.33}$$

where the derivatives are evaluated at $\vec{k} = \vec{G}_j$.

The final expression is now

$$\begin{aligned}
F_{ex(cg)} = \sum_j \int d\vec{r}(-1)|\eta_j|^2 &\left(X_1(c)\hat{C}_2^{AA}(|\vec{G}_j|) + X_2(c)\hat{C}_2^{BB}(|\vec{G}_j|)\right) \\
&-\frac{1}{|\vec{G}_j|^2}\left(X_1(c)\hat{C''}_2^{AA}(|\vec{G}_j|) + X_2(c)\hat{C''}_2^{BB}(|\vec{G}_j|)\right)|\left(i\vec{G}_j\cdot\nabla\right)\eta_j|^2
\end{aligned} \tag{B.34}$$

Thus our total coarse grained, amplitude model expression, obtained via a binary alloy XPFC model, is:

$$
\begin{aligned}
F_{cg} = \int d\vec{r} \big(1 - \eta n_0 + \chi n_0^2\big) \left(A_1^2 + A_2^2 + B_1^2 + B_2^2 + C_1^2 + C_2^2 + C_3^2\right) \\
+\frac{1}{2} n_0^2 - \frac{\eta}{6} n_0^3 + \frac{\chi}{12} n_0^4 + \omega(n_0+1)\Delta F_{mix}(c) + \alpha|\nabla c|^2 \\
+ (4\chi n_0 - 2\eta)\left(A_1 A_2 B_1 + A_1 A_2 B_2 + C_1 C_2 C_3\right) \\
+\frac{\chi}{2}\left(A_1^4 + A_2^4 + B_1^4 + B_2^4 + C_1^4 + C_2^4 + C_3^4\right) \\
+2\chi A_1^2\left(B_1 B_2 + C_2 C_3\right) + 2\chi A_1^2\left(A_2^2 + B_1^2 + B_2^2 + C_1^2 + C_2^2 + C_3^2\right) \\
+2\chi A_1^2 B_1 B_2 + 2\chi A_2^2\left(B_1^2 + B_2^2 + C_1^2 + C_2^2 + C_3^2\right) \\
+2\chi B_1^2\left(B_2^2 + C_1^2 + C_2^2 + C_3^2\right) + 2\chi B_2^2\left(C_1^2 + C_2^2 + C_3^2\right) \\
+2\chi C_1^2\left(C_2^2 + C_3^2\right) + 2\chi C_2^2 C_3^2 + 4\chi B_1 B_2 B C_2 C_3 \\
-2(A_1^2 + A_2^2)\left(X_1(c)\hat{C}_2^{AA}(|\vec{k}_{10}^A|) + X_2(c)\hat{C}_2^{BB}(|\vec{k}_{10}^A|)\right) \\
-2(B_1^2 + B_2^2)\left(X_1(c)\hat{C}_2^{AA}(|\vec{k}_{11}^A|) + X_2(c)\hat{C}_2^{BB}(|\vec{k}_{11}^A|)\right) \\
-2(C_1^2 + C_2^2 + C_3^2)\left(X_1(c)\hat{C}_2^{AA}(|\vec{k}_{10}^B|) + X_2(c)\hat{C}_2^{BB}(|\vec{k}_{10}^B|)\right) \\
-\frac{1}{|\vec{k}_{10}^A|^2}\left(X_1(c)\hat{C''}_2^{AA}(|\vec{k}_{10}^A|) + X_2(c)\hat{C''}_2^{BB}(|\vec{k}_{10}^A|)\right)\left[\left|\left(i\vec{k}_{10}^A\cdot\nabla\right)A_1\right|^2 + \left|\left(i\vec{k}_{10}^A\cdot\nabla\right)A_2\right|^2\right] \\
-\frac{1}{|\vec{k}_{11}^A|^2}\left(X_1(c)\hat{C''}_2^{AA}(|\vec{k}_{11}^A|) + X_2(c)\hat{C''}_2^{BB}(|\vec{k}_{11}^A|)\right)\left[\left|\left(i\vec{k}_{11}^A\cdot\nabla\right)B_1\right|^2 + \left|\left(i\vec{k}_{11}^A\cdot\nabla\right)B_2\right|^2\right] \\
-\frac{1}{|\vec{k}_{10}^B|^2}\left(X_1(c)\hat{C''}_2^{AA}(|\vec{k}_{10}^B|) + X_2(c)\hat{C''}_2^{BB}(|\vec{k}_{10}^B|)\right) \\
\left[\left|\left(i\vec{k}_{10}^B\cdot\nabla\right)C_1\right|^2 + \left|\left(i\vec{k}_{10}^B\cdot\nabla\right)C_2\right|^2 + \left|\left(i\vec{k}_{10}^B\cdot\nabla\right)C_3\right|^2\right]
\end{aligned}
\tag{B.35}
$$

Bibliography

[1] F. Gonzales and M. Rappaz. Dendrite growth directions in aluminum-zinc alloys. *Metallurgical and Materials Transactions A*, 37(9):2797–2806, 2006.

[2] W. D. Callister Jr. *Materials science and engineering: an introduction*. Wiley, 2010.

[3] T. Haxhimali, A. Karma, F. Gonzales, and M. Rappaz. Orientation selection in dendritic evolution. *Nature Materials*, 5:660–664, 2006.

[4] J. Friedli, J.L. Fife, P. Di Napoli, and M. Rappaz. Dendritic growth morphologies in al-zn alloys—part i: X-ray tomographic microscopy. *Metallurgical and Materials Transactions A*, 44(12):5522–5531, 2013.

[5] S. Henry, T. Minghetti, and M. Rappaz. Dendrite growth morphologies in aluminium alloys. *Acta Materialia*, 46(18):6431–6443, 1998.

[6] A. Karma and W. J. Rappel. Phase-field method for computationally efficient modeling of solidification with arbitrary interface kinetics. *Physical Review E*, 53(4): R3017–R3020, 1996.

[7] N. Provatas, N. Goldenfeld, and J. Dantzig. Efficient computation of dendritic microstructures using adaptive mesh refinement. *Physical Review Letters*, 80(15):3308–3311, 1998.

[8] M. Greenwood, M. Haataja, and N. Provatas. Crossover scaling of wavelength selection in directional solidification of binary alloys. *Physical Review Letters*, 93:246101, 2004.

[9] M. Amoorezaei, S. Gurevich, and N. Provatas. Spacing characterization in al-cu alloys directionally solidified under transient growth conditions. *Acta Materialia*, 58 (18):6115–6124, 2010.

[10] V. Fallah, A. Korinek, N. Ofori-Opoku, N. Provatas, and S. Esmaeili. Atomistic investigation of clustering phenomenon in the al-cu system: three-dimensional phase-field crystal simulation and hrtem/hrstem characterization. *Acta Materialia*, 61(17): 6372–6386, 2013.

[11] L. Granasy, T. Pusztai, and J. A. Warren. Modeling polycrystalline solidification using phase field theory. *Journal of Physics: Condensed Matter*, 16:R1205–R1235, 2004.

[12] H. Emmerich, H. Lowen, R. Wittkowski, G. Gruhn, T.and Toth, G. Tegze, and L. Granasy. Phase-field-crystal models for condensed matter dynamics on atomic length and diffusive time scales: an overview. *Advances in Physics*, 61(6):665–743, 2012.

[13] N. Provatas, M. Greenwood, B. Athreya, N. Goldenfeld, and J. Dantzig. Multi-scale modeling of solidification: phase field methods to adaptive mesh refinement. *International Journal of Modern Physics B*, 19(31):4525–4566, 2005.

[14] N. Provatas and K. Elder. *Phase-field methods in material science and engineering*. Wiley, 2010.

[15] A. Semoroz, Y. Durandet, and M. Rappaz. Ebsd characterization of dendrite growth directions, texture and mmisorientations in hot-dipped al-zn-si coatings. *Acta Materialia*, 49(3):529–541, 2001.

[16] J.J. Hoyt, M. Asta, and A. Karma. Method for computing the anisotropy of the solid-liquid interfacial free energy. *Physical Review Letters*, 86(24):5530–5533, 2001.

[17] K.R. Elder and M. Grant. Modeling elastic and plastic deformations in non equilibrium processing using phase field crystals. *Physical Review E*, 70:051605, 2004.

[18] K.R. Elder, N. Provatas, J. Berry, P. Stefanovic, and M. Grant. Phase-field crystal modeling and classical density functional theory of freezing. *Physical Review B*, 75: 064107, 2007.

[19] M. Greenwood, J. Rottler, and N. Provatas. Phase-field-crystal methodology for modeling of structural transformations. *Physical Review E*, 83:031601, 2011.

[20] K.R. Elder, M. Katakowski, M. Haataja, and M. Grant. Modeling elasticity in crystal growth. *Physical Review Letters*, 88(24):245701, 2002.

[21] T.V. Ramakrishnan and M. Yussouff. First-principles order-parameter theory of freezing. *Physical Review B*, 19(5):2775–2794, 1979.

[22] K. R. Elder, Z.-F. Huang, and N. Provatas. Amplitude expansion of the binary phase-field-crystal model. *Physical Review E*, 81(1):011602, 2010.

[23] M. Greenwood, N. Provatas, and J. Rottler. Free energy functionals for efficient phase field crystal modeling of structural phase transformations. *Physical Review Letters*, 105:045702, 2010.

[24] M. Greenwood, N. Ofori-Opoku, J. Rottler, and N. Provatas. Modeling structural transformations in binary alloys with phase field crystals. *Physical Review B*, 84: 064104, 2011.

[25] J. W. Cahn and J. E. Hilliard. Free energy of a nonuniform system: I. interfacial free energy. *Journal of Chemical Physics*, 28(2):258–267, 1958.

[26] J. Mellenthin, A. Karma, and M. Plapp. Phase-field crystal study of grain-boundary pre melting. *Physical Review B*, 78:184110, 2008.

[27] V. Kalikmanov. *Statistical physics of fluids: basic concepts and applications*. Springer Berlin, 2001.

[28] N. Provatas and S. Majaniemi. Phase-field-crystal calculation of crystal-melt surface tension in binary alloys. *Physical Review E*, 82:041601, 2010.

[29] N. Provatas and S. Majaniemi. Deriving surface-energy anisotropy for phenomenological phase-field models of solidification. *Physical Review E*, 79:011607, 2009.

[30] L. D. Landau and E. M. Lifshitz. *Statistical Physics*. ButterWorth-Heinemann, 1980.